Probing Impulsive Strain and Lattice Dynamics by Time-Resolved Ultrafast X-ray Diffraction

A Thesis

Presented in

Partial Fulfillment for the

Requirements for the Degree of

MASTER OF SCIENCE

June, 2010

by

G. Jackson Williams

PHYSICS DEPARTMENT

College of Liberal Arts and Sciences

DePaul University

Chicago, Illinois

© G. Jackson Williams 2010

All Rights Reserved

To My Family and Friends

ACKNOWLEDGEMENTS

Having just completed the final additions to this thesis, I would like to thank everyone who made this possible. Without their support, both mentally and physically, I would not have made it this far.

I would like to thank my family for their unending support of my goals and hobbies. You have given me the inspiration to reach for what I did not think was possible and cheered me on no matter what I wanted to do. The greatest gift is your genuine curiosity and interest in what I do. Thank you also for the hamburger money you give me when I come home to visit. Claire and Bailey, thank you for the wisecracks about my experiments and not allowing me to take myself too seriously. Denise, thank you for making sure I got enough to eat and putting up with my tardiness. You have supplied me with the support I needed to be successful through these last two years. It is hard to tell all of you how much I love you and to thank you enough for what you have given me.

To my advisor, Eric C. Landahl, for all the guidance and mentoring. It has been a pleasure to work for you. Thank you for being a great role model, teaching me how to think like an experimentalist, and sending me down my current path. It was a great learning experience to help you build your lab up from nothing. Thank you also for teaching me about x-rays and lasers, easily the two coolest fields in all of physics. Most importantly I would like to thank you for your lab space. It was a personal refuge for doing homework, avoiding distractions, and fiddling around with ultrafast lasers. To Sarah and her caring, generous family, thank you for the Wisconsin vacation and the first aid when I cut my foot open.

I need to thank Dohn Arms and Don Walko of Sector 7 at the APS for treating me so well and not just like any other user. You have treated me like a colleague from the beginning and helped me at every turn. Thank you also for the discussions of x-ray diffraction and diffraction simulations, without you I would have never understood dynamical diffraction or how to code Wie.

To my advisor at St. Olaf College, Jason J. Engbrecht, without your help I would have never had the ambition to become an experimental scientist. Thank you for pushing me when you did and giving me the chance to work for you. It has changed

the course of my life for the best.

I would also like to thank my thesis committee members, Eric Dufresne and Gabriela Gonzalez-Aviles, for reading all of this and being such a pleasure to work with.

As well, I would like to thank Nate, Adam, Erik and Tyler for their friendship and advice over the last 6 years. I am sure I have left some people out to whom I owe my appreciation, but I will need to do that in person.

TABLE OF CONTENTS

LIST OF FIGURES vii

LIST OF TABLES x

CHAPTER

I. Introduction 1

1.1 Ultrafast Dynamics 2
1.2 Thesis Motivation 4

II. Dynamics of Strain in Semiconductor Crystals 6

2.1 Semiconductors Under Ultrafast Laser Excitation 6
2.2 Strain in Semiconductors 10

III. X-ray Diffraction in Ideal Crystals 19

3.1 X-ray Diffraction 20
3.2 The Structure Factor 23
3.3 Kinematic Diffraction 31
3.4 Dynamical Diffraction 34
3.5 Numerical Modeling 37
3.6 Comparison with $\chi_{0,H}$ 41

IV. Experimental Setup 45

4.1 X-ray source 45
4.2 Beamline layout 49
4.3 Pump-Probe X-ray Experiments 51
4.4 Detectors 52
4.4.1 Counting Mode 53
4.4.2 Proportional Mode 56
4.5 Data Acquisition / Ztec Oscilloscope 56

4.6 Laser System 59

V. Time-Resolved X-ray Diffraction 61

5.1 Time Resolved X-ray Rocking Curves 61
5.2 InSb Results 65
5.3 GaAs Results 71
5.4 Comparison with Models 75

VI. Conclusions and Outlook 81

APPENDICES 83

A. Physical Properties of GaAs and InSb 84

B. Ztec Oscilloscope Boot Protocol 85

C. Matlab Code 87

C.1 Strained Crystal Dynamical Diffraction Routines 87
C.1.1 Main Routine for Dynamical Diffraction 87
C.1.2 Structure Factor 88
C.1.3 Calculating the Debye-Waller Coefficient 91
C.1.4 Determining $\psi_{0,H}$ 92
C.1.5 Takagi-Taupin Rocking Curves 92
C.1.6 Thomsen Strain Model for GaAs 95
C.1.7 Thomsen Strain Model for InSb 96
C.1.8 Asymmetric Thermoelastic Model for InSb 97
C.2 Data Reduction and Analysis 98
C.2.1 Main Routine for GaAs Data Extraction 98
C.2.2 Extract Centroid Shifts for Each Fluence for GaAs . 100
C.2.3 Main Routine for InSb Data Extraction 101
C.2.4 Extract Centroid Shifts for Each Fluence for InSb . 103
C.2.5 Deadtime Correction Subroutine 104
C.3 Dispersion Correction Terms $\Delta f'$ and $\Delta f''$ 105
C.3.1 Indium 105
C.3.2 Antimony 112
C.3.3 Gallium 119
C.3.4 Arsenide 125

BIBLIOGRAPHY 132

LIST OF FIGURES

Figure

1.1 Typical Pump-Probe Experimental Setup 3

1.2 Example Rocking Curve 4

1.3 Example Data of Bragg Peak Shifts 5

2.1 Carrier Generation Processes 7

2.2 Carrier Thermalization Processes 8

2.3 Schematic of Auger Recombination 9

2.4 Thomsen Strain Model 11

2.5 Strain Profile with Diffusion and Auger Recombination 13

2.6 Temperature Profile with Diffusion and Auger Recombination . . . 14

2.7 Electron Density Profile with Diffusion and Auger Recombination . 15

2.8 Traveling Strain Wave 17

2.9 Schematic of Ultrafast Excitation in Semiconductors 18

3.1 Three Dimensional Representation of the Unit Cell 20

3.2 Geometric Representation of Diffraction 21

3.3 Vector Representation of the Bragg Law 22

3.4 Geometric Atomic Form Factor 26

3.5 Dispersion Corrections $\Delta f'$ and $\Delta f''$ 28

3.6 Model of a Zinc-Blende Unit Cell 29

3.7 Dynamical Diffraction Schematic 35

3.8 Darwin Calculation for Reflection Intensity 36

3.9 Cartoon of Wave Representation in Dynamical Diffraction 37

3.10 Asymmetric Bragg Reflection Geometry 39

3.11 Schematic of Wie Algorithm 40

3.12 Bragg Diffraction Peak with Unstrained and Strained Crystal Lattice 42

3.13 Comparison between Wie ($\psi_{0,H}$) and $\chi_{0,H}$ for InSb 43

3.14 Comparison between Wie ($\psi_{0,H}$) and $\chi_{0,H}$ for GaAs 44

4.1 APS Experiment Floor 46

4.2 Undulator Insertion Device 47

4.3 Beamline Layout 49

4.4 Example of a Top Up Occurrence 50

4.5 Experimental Layout 51

4.6 Deadtime Correction for Counting Detector 54

4.7 Counting Statistics for Deadtime Corrections 55

4.8 X-ray Bunch Train From Proportional Mode APD 57

4.9 Timing Diagram for Typical Time Resolved Experiment 58

5.1 Schematic of Rocking Curve Response to Lattice Distortion 63

5.2 Gaussian Fits to Rocking Curves 65

5.3 InSb Rocking Curves at 400 ps After Excitation 67

5.4 Time-Resolved Centroid Shift for InSb at Various Fluences 68

5.5 Time-Resolved Changes in FWHM for InSb at Various Fluences . . 69

5.6 Peak and Thermal Strain in InSb 70

5.7 Rocking Curve of GaAs at Initial Time Points 71

5.8 Time Resolved Centroid Shift for GaAs at Various Fluences 72

5.9 Time Resolved Changes in FWHM for GaAs at Various Fluences . . 73

5.10 Peak and Thermal Strain in GaAs 74

5.11 Centroid Shifts for InSb with Thomsen Model 76

5.12 InSb plotted with Thomsen Model 77

5.13 Time Resolved Centroid Shift with Nonlinear Strain 78

5.14 Centroid Shifts for GaAs with Nonlinear Strain 80

LIST OF TABLES

Table

3.1 Cromer-Mann Atomic Scattering Factors 27

3.2 Dispersion Corrections 27

3.3 Fractional lattice coordinates for GaAs in a zinc blende structure . . 29

3.4 Structure Factors for InSb and GaAs 30

3.5 Average Atomic Displacements 31

3.6 Parameters for Wie Method of Dynamical Diffraction 38

A.1 Properties of GaAs and InSb at 300 K 84

CHAPTER I

Introduction

The interest in semiconductor dynamics is driven by the rise of solid state technology in consumer products and the pursuit of a fundamental understanding of physical properties. High purity, perfect crystal semiconductors are readily available and used in applications in the telecommunication, computer, and laser industries. With femtosecond laser pulses, extremely fast dynamics can be probed, helping to understand the fundamental interaction between light and matter on the time scale of a few oscillations of an electromagnetic field. Optical reflectivity and transmission of perturbed systems were the first experiments to indirectly measure the crystal lattice response to ultrafast excitation. X-ray diffraction, however, is able to directly assess the atomic positions inside the lattice. Synchrotron radiation, producing high brilliance x-ray pulses, together with time resolved experimental methods allows for picosecond resolution of transient dynamics in semiconductors.

Measuring acoustic phonons and strain in bulk materials has been an ongoing area of interest in the time-resolved research community. Although there are several proposals to explain the dynamics observed in crystals none describe nonlinear dependencies on deposited energy in crystals far below the damage threshold. This thesis presents time-resolved studies of strain and acoustic impulses in bulk semicon-

ductors and provides an explanation for observed ultrafast dynamics. This work is based on pump-probe experiments of indium antimonide (InSb) and gallium arsenide (GaAs). X-ray diffraction simulations of strained crystals have been developed to provide direct analysis of the data.

The remainder of this chapter serves to introduce the subject of ultrafast semiconductor science. Chapter II reviews relevant theories of ultrafast dynamics and strain in semiconductors. Chapter III introduces the theory of x-ray diffraction in perfect crystals. It continues to explain calculations for simulations of x-ray diffraction in strained crystals developed for these experiments. The experimental setup is discussed in Chapter IV. In Chapter V, results of the optical pump, x-ray probe experiment are presented for InSb and GaAs. Finally, Chapter VI concludes the study and proposes new opportunities for development of this research.

1.1 Ultrafast Dynamics

Semiconductor crystals absorb photons of energies $h\nu$, greater than the band gap E_g. In direct gap semiconductors, this process promotes valence band electrons to the conduction band without a change in momentum. At high incident radiation densities, the electron-hole pairs create an electrostatic potential large enough to alter the periodic structure of the crystal. This deformation potential deflects atomic planes, straining the crystal. Photo-induced strain occurs only within the penetration depth of the light, typically 100 – 1000 nm. The perturbed atomic planes recoil as they return to equilibrium positions, launching a coherent acoustic impulse.

The first proposed model to describe crystalline strain was a thermoelastic traveling wave model where all incident radiation energy is deposited into the lattice as heat. The resulting transient strain wave propagates at the speed of sound in the

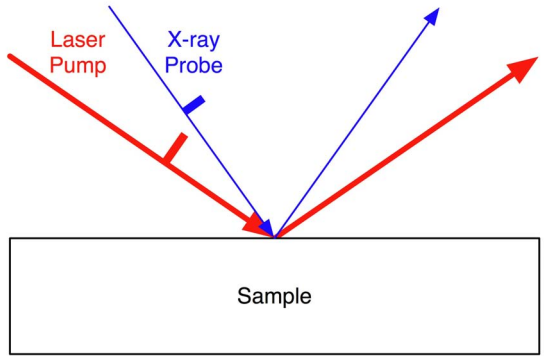

Figure 1.1: Typical setup for a time resolved pump probe experiment. The x-ray pulse probes the crystalline lattice at a time after a laser pulse perturbs the system.

material into the crystal depth, while a permanent exponential strain profile remains at the surface. A constant strain is a good first approximation since thermal diffusion is extremely slow compared to electron diffusion (six orders of magnitude slower) or other transient processes in photo-excited semiconductors. In this model, the strain response is linear with the amount of absorbed energy.

Many previous experiments have analyzed acoustic impulses and strained semiconductors data with this model [1–5]. There exists omissions from this model, including contributions from electrons and nonlinear responses to absorbed laser fluence. Other experiments have accounted for the electrons by including electron-hole plasma diffusion and Auger recombination for germanium [6]. Free carrier absorption for GaAs has also been proposed, but has not provided satisfactory supporting evidence to this phenomenon [7]. The experiments presented in this thesis investigates strain in InSb and GaAs and presents a strain model to describe the nonlinear fluence dependence in GaAs.

To measure transient strain, time-resolved Bragg x-ray diffraction is employed. This technique has been established as a powerful tool to view transient structural

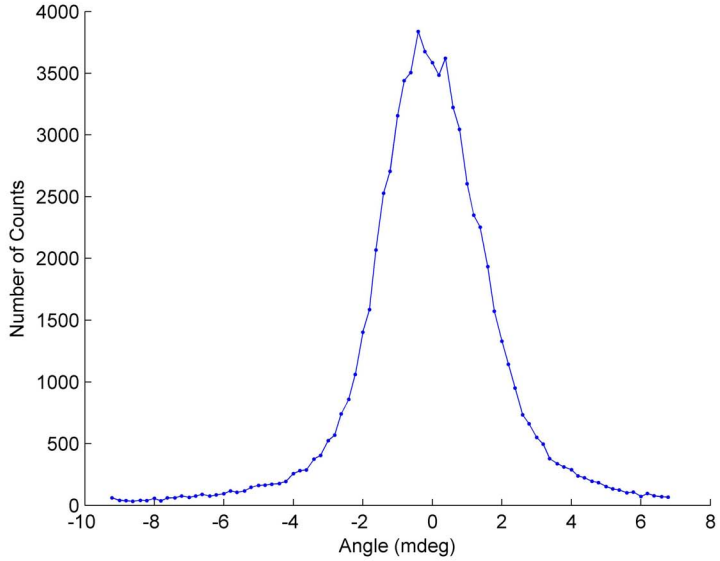

Figure 1.2: Example of Bragg diffraction peak for InSb.

dynamics in crystalline solids [8]. Using a pump-probe experimental setup (Figure 1.1), wafer samples of polished semiconductors are illuminated by femtosecond pulses of amplified laser light, deforming the crystal lattice. At a variable delay, the x-ray probe diffracts from the perturbed structure, resolving transient dynamics in the material. The delay is systematically lengthened from time-zero, T_0, or the time when x-ray and laser pulse arrive concurrently. As the crystalline lattice is distorted, the distance between atomic planes changes and the satisfactory angle for Bragg diffraction shifts. Bragg peaks (see Figure 1.2) are recorded at each time point and the center is extracted. An example of the time-resolved data for the centroid Bragg peak shift is shown in Figure 1.3.

1.2 Thesis Motivation

The dynamics of photo-excited semiconductor systems have been the focus of many experimental pursuits [1, 4, 9]. However, a detailed understanding of the lattice

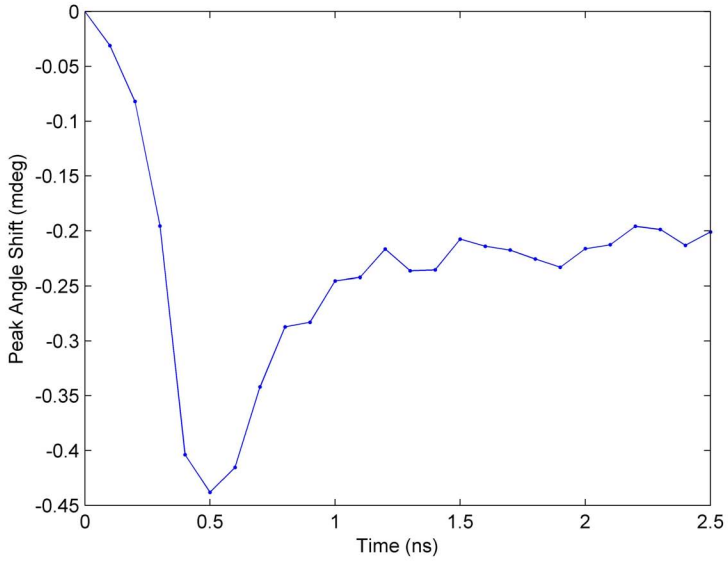

Figure 1.3: Example of Bragg diffraction peak-shift data for InSb at low fluences.

dynamics and thermalization are still illusive. These studies have used a computer model to predict the outcome of x-ray diffraction that did not include the detail necessary to investigate intensity-dependent dynamics in lattice structure across different systems. The available programs had not been adequately benchmarked, were not flexible in the selection of materials or x-ray energies, and were not scaleable to the study of increasingly complicated models of real semiconductor behavior.

Furthermore, there exists unanswered questions on the linear and nonlinear effects of InSb and GaAs. The fluence dependence of these materials are in stark contrast with each other and offer insights to carrier generation and thermalization as well as structural dynamics. This thesis demonstrates the correct method of constructing strain profiles for the purpose of analyzing time-resolved diffraction experiments.

CHAPTER II

Dynamics of Strain in Semiconductor Crystals

Strain in semiconductors generally results from lattice mismatch in atomic planes. The lattice mismatch may be constant in time, such as a crystal epitaxially grown on a substrate, or can be transient such as an acoustic phonon. This discussion will focus on transient strain in crystals where strain is produced from rapid heating, acoustic impulses, and interactions between free carriers and the lattice. The following reviews the physics of semiconductors and crystal strain imposed upon ultrafast laser excitation.

2.1 Semiconductors Under Ultrafast Laser Excitation

When light is incident on opaque material, several processes and interactions occur on various time scales from femtoseconds (10^{-15} s) to nanoseconds (10^{-9} s) which eventually transfers energy from absorbed photons to thermal vibrations in the lattice [10]. It is important to note that the subsequent processes are not sequential, but rather happens across overlapping intervals. The first energy transition is carrier generation. Photons of energy exceeding the band gap are absorbed to create a single electron-hole pair. The excess photon energy moves immediately into the lattice

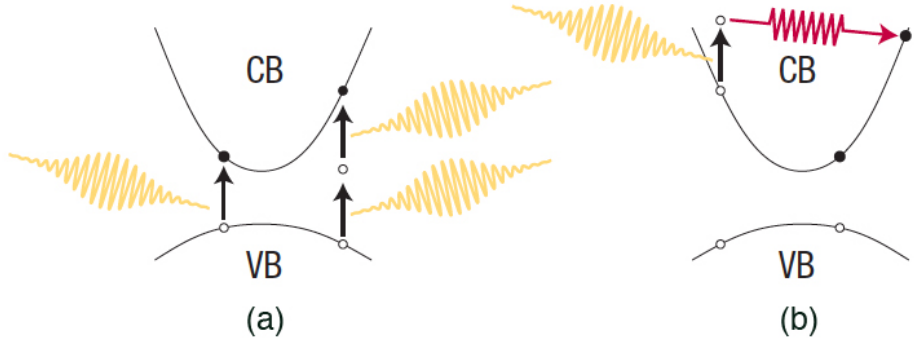

Figure 2.1: Carriers are generated through single or two photon absorption (a). Photons can also be captured through free carrier absorption (b). Figure adapted from [10].

as thermal vibrations. Two photon absorption, a nearly instantaneous process, will occur at high field intensities but since this process is intensity dependent and these experiments do not have the necessary photon densities, it does not play a role in dynamics discussed here. As well, an electron in the conduction band can absorb a second photon, called free carrier absorption (FCA). FCA does not increase the carrier density but creates highly energetic carriers within the lattice, potentially liberating additional electrons at a later time through impact ionization. Carrier generation occurs on a time scale of up to a few femtoseconds. A cartoon of these processes is given in Figure 2.1

The crystal enters the thermalization regime after the ultrashort pulse has exited the crystal and deposited energy into the electrons. Thermalization occurs primarily through carrier-carrier and carrier-phonon scattering, depositing energy into the lattice on the time scale of a few hundred femtoseconds to tens of picoseconds. Carrier-carrier scattering is an electrostatic collision that does not change the total energy of the carriers. It may take hundreds of femtoseconds for carriers to equilibrate through

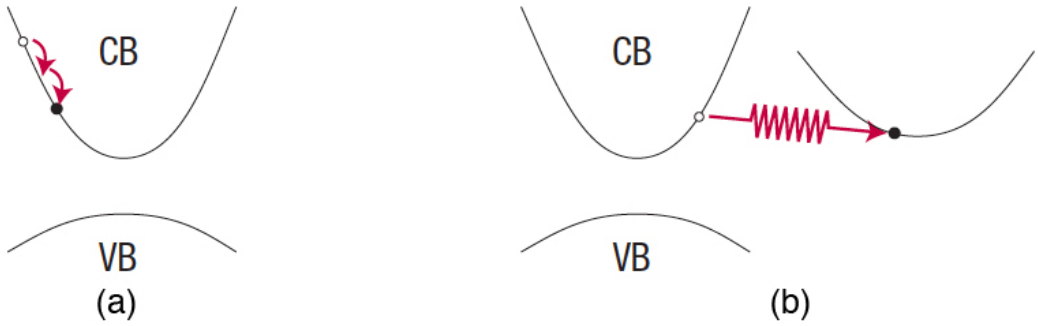

Figure 2.2: Carriers thermalize through carrier-carrier scattering (a) or carrier-phonon scattering (b) where carriers emit a phonon as heat into the lattice. Figure adapted from [10].

carrier-carrier scattering. Carrier-phonon scattering is an inelastic process in which electrons absorb (or emit) phonons, gaining (or losing) energy and momentum to the lattice. Figure 2.2 gives a schematic of the thermalization processes. Each of these process do not change the carrier density, but decreases the total carrier energy through the emission of phonons. All carriers generally reach thermal equilibrium after a few picoseconds. Throughout carrier generation and thermalization, electrons are diffusing into the crystal depth. Initially, electrons are deposited throughout the penetration depth of the laser (~ 100 nm – 1μm). Immediately, these carriers begin to propagate at supersonic speeds, dependent on the diffusion constant in the material.

At longer time regimes, picoseconds to nanoseconds, the lattice carriers are removed through recombination. Carrier removal takes place through radiative or non-radiative recombination. In radiative recombination, electrons transition from the conduction band to valence band and release energy as a photon. Since energy is radiated away from the crystal, the lattice remains unaffected. Non-radiative recombination transfers energy to the lattice and is dominated by Auger recombination.

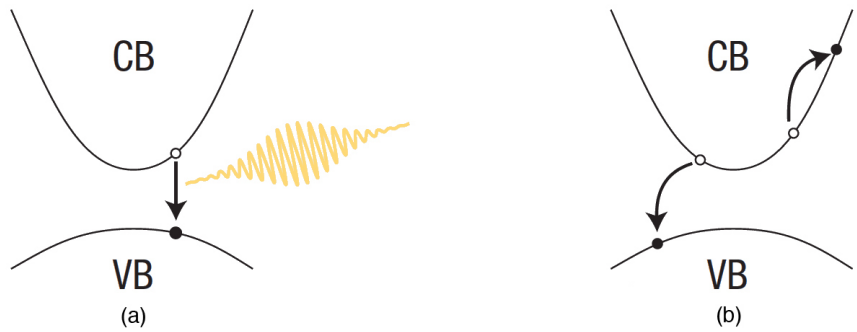

Figure 2.3: Radiative recombination (a) releases a photon where in Auger recombination (b), an electron and hole recombine, donating the excess energy to a third carrier. Figure adapted from [10].

Other non-radiative processes like recombination-generation centers and defect-and-surface recombination rely on dopants or impurities to facilitate the transition of energy into the lattice. The samples used in this study are of extremely high purity and other non-radiative recombination processes do not play a major roll in carrier removal. Auger recombination goes as the cube of the carrier density, n,

$$\frac{\partial n}{\partial t} = -An^3 \tag{2.1}$$

where A is the Auger coefficient. This contribution quickly overpowers other recombination contributions due to the cubic dependency. The Auger process occurs when an electron and hole collide and recombine, giving the excess energy to third carrier (see Figure 2.3). This three-particle process is responsible for the cubic density dependence. The higher energy electrons thermalize through carrier-carrier and carrier-phonon scattering, giving energy to the lattice as heat. After all carriers have recombined, the lattice is hot and identical to that of a crystal heated in by conventional means where the lattice vibrations are indistinguishable between the two

cases.

In an opaque semiconductor heated without the use of ultrafast pulses, melting would occur if the root mean square of the atomic displacement (vibrational amplitude), $\langle u^2 \rangle^{1/2}$, exceeds the Lindemann criterion, or 10% of RMS displacement. When femtosecond pulses are used, the lattice disorder is initially due completely to the non-thermal electronic excitation component. At large pulse energy densities ablation can occur where free electron absorption dominates early dynamics and drives lattice vibrations into a non-thermal melting regime where material is ejected from the surface.

2.2 Strain in Semiconductors

The specific dynamics of the lattice through excitation, thermalization, and carrier removal is of importance to many in the scientific community and the semiconductor industry (e.g. optical communication, photovoltaics, solid state lasers). When carriers are produced, the lattice can[1] respond to the deformation potential by expanding. The coupling between carriers and lattice creates a highly perturbed system within the penetration depth while leaving the bulk unaffected. After the pump pulse leaves, the deformation propagates as an acoustic pulse throughout the crystal. This stress pulse, or coherent longitudinal acoustic phonon, moves through the lattice at the speed of sound. An analytic model to this strain was proposed by Thomsen *et al.* to describe an exponential strain profile matching the penetration depth profile [11]. This model assumes only thermal contributions with strain dependent on the depth, z, such that the strain tensor, $[\boldsymbol{\eta}]$, has a single nonzero component η_{33}. The solution

[1]Deformation potentials can be positive or negative, corresponding to a expansion or contraction of the lattice. In this discussion, all materials happen to have positive deformation potentials.

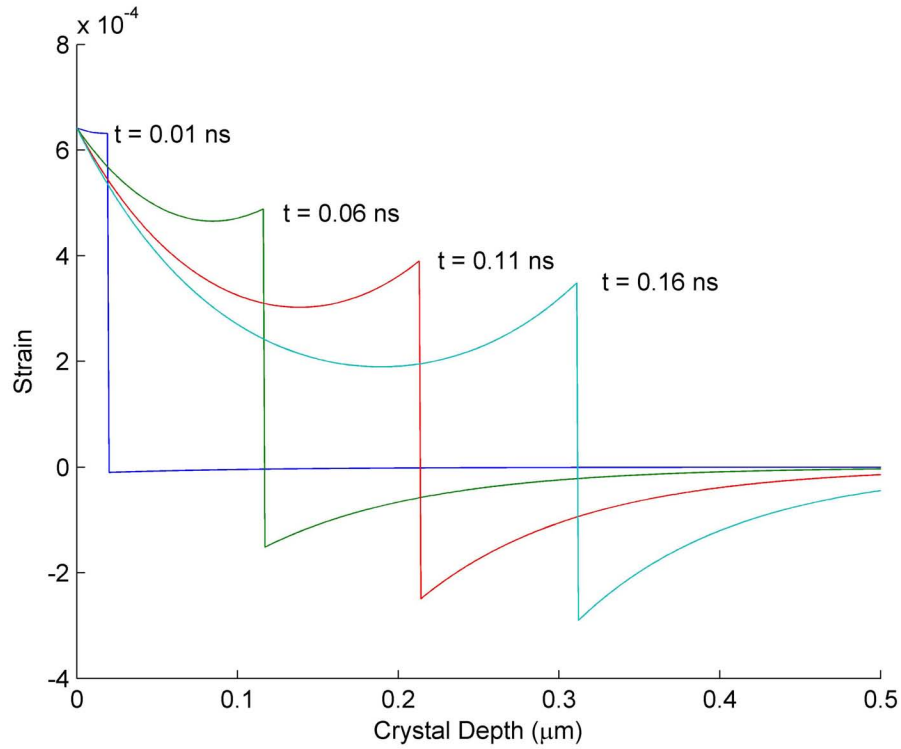

Figure 2.4: Thomsen strain model at several time points. Calculated using Equation 2.2 for InSb.

to the wave equation with the initial condition of zero strain everywhere at $t = 0$ is

$$\eta(z,t) = (1-R)\frac{Q\beta}{A\zeta C}\frac{1+\nu}{1-\nu}\left[e^{-z/\zeta}(1-\tfrac{1}{2}e^{-vt/\zeta}) - \tfrac{1}{2}e^{-|z-vt|/\zeta}\,\mathrm{sgn}(z-vt)\right] \qquad (2.2)$$

where R is the reflectivity, Q is the energy incident on the surface of the crystal , β is the linear expansion coefficient, A is the illuminated spot size, ζ is the absorption length, C is the specific heat per unit volume, and ν is Poisson's ratio. The longitudinal speed of sound, v, in the material is given by

$$v^2 = 3\frac{1-v}{1+v}\frac{B}{\rho}$$

where B is the bulk modulus and ρ is the density. A list of these parameters are given in Appendix A for InSb and GaAs.

The thermoelastic Thomsen model is mathematically sound and accurately represents an undamped wave in a homogeneous medium. Since the initial condition is zero strain everywhere, the propagating strain pulse is bipolar and has equal contributions of negative and positive amplitudes. The Thomsen strain is a product of thermal expansion alone where the temperature rise in the crystal $\Delta T(z)$, is a function of only the energy deposited per unit volume within the crystal,

$$\Delta T(z) = (1 - R)\frac{Q}{A\zeta C}e^{-z/\zeta}.$$

That is, all of the energy in the laser pulse is converted directly into heat. This is an approximation as previous experiments have shown that the electron-phonon coupling time is $\sim$ 10 ps in many semiconductors [1,12,13]. The finite generation time smooths out the discontinuity in the Thomsen wave model. As well, strain generation in the Thomsen model is not physical. For ultrafast pulses, energy is deposited into the lattice within $\sim$ 50 fs. In Figure 2.4, it can be seen that the strain takes an extremely long amount of time to strain the penetration depth of the laser.

A plasma driven strain model, proposed by DeCamp *et al.* (a version of the this strain model is shown in Figure 2.5), accounts for the coupling between the photo-excited plasma and lattice [6]. The temperature profile (Figure 2.6) is dependent on the contributions from Auger recombination and temperature diffusion,

$$\frac{\partial T}{\partial t} = D_t\frac{\partial^2 T}{\partial z^2} + An^3\frac{E_g}{C} \tag{2.3}$$

where D_t is the thermal diffusion coefficient and E_g is the electronic band gap. The

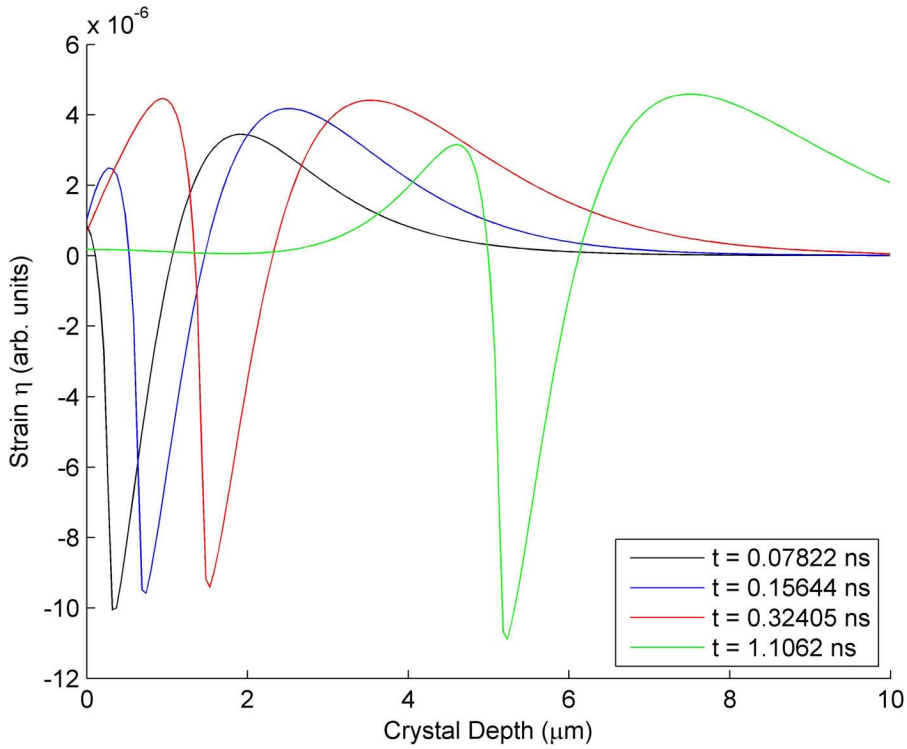

Figure 2.5: Strain profile for the case including diffusion and recombination at several time points. Calculated from Equation 2.5 for GaAs at a fluence of 0.25 mJ/cm^2 and laser wavelength at 800 nm.

number density of carriers is reduced by Auger recombination and diffusion moves electrons into the lattice. The diffusion length L_{diff}, is proportional to the diffusion constant and a function of time where

$$L_{\text{diff}} \sim 2\sqrt{D_{t,e}\, t}$$

and

$$\frac{\partial n}{\partial t} = D_e \frac{\partial^2 n}{\partial z^2} - An^3. \tag{2.4}$$

The electron diffusion (Figure 2.7) is often supersonic, creating stress deep in the

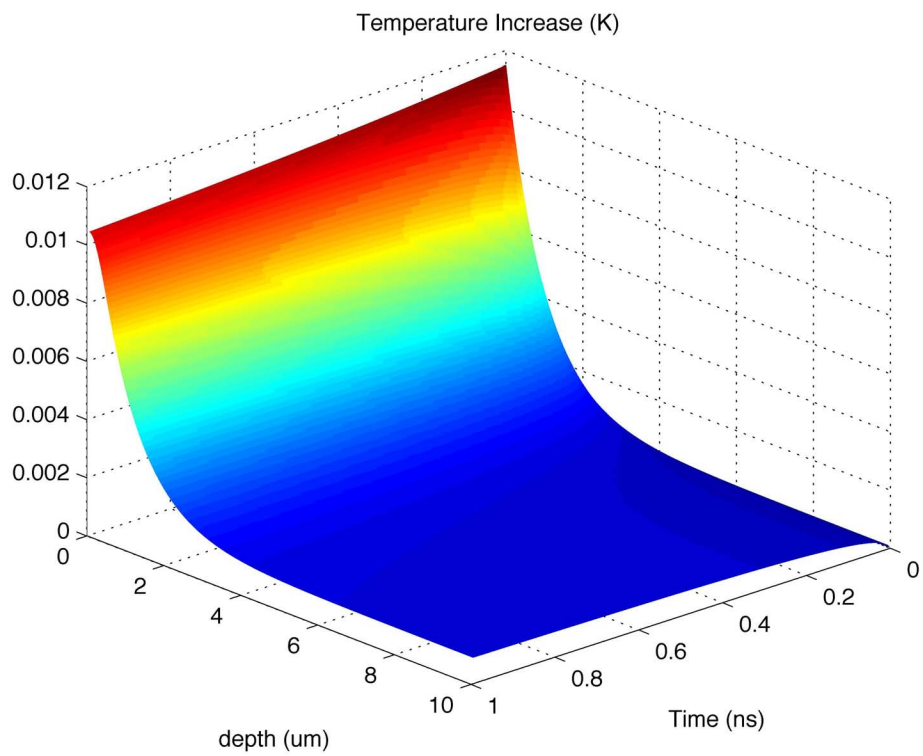

Figure 2.6: Temperature profile for GaAs, at a fluence of 0.25 mJ/cm^2, including contributions from Auger recombination and thermal diffusion. The crystal remains hot at the surface due to slow thermal diffusion and additional heat supplied by the Auger effect.

crystal before the acoustic pulse arrives which spatially broadens the acoustic pulse by a factor of up to five [14]. The strain profile now contains temperature and plasma density dependences:

$$\eta(z,t) = \alpha_t T(z,t) + \alpha_e n(z,t) \tag{2.5}$$

where α_t is the thermal expansion coefficient and α_e is the electronic coupling coefficient, also referred to as the deformation potential [6]. A list of values for these parameters is presented in Appendix A for InSb and GaAs. The strain, η, drives a displacement in the lattice (strain wave) along a direction normal to the surface,

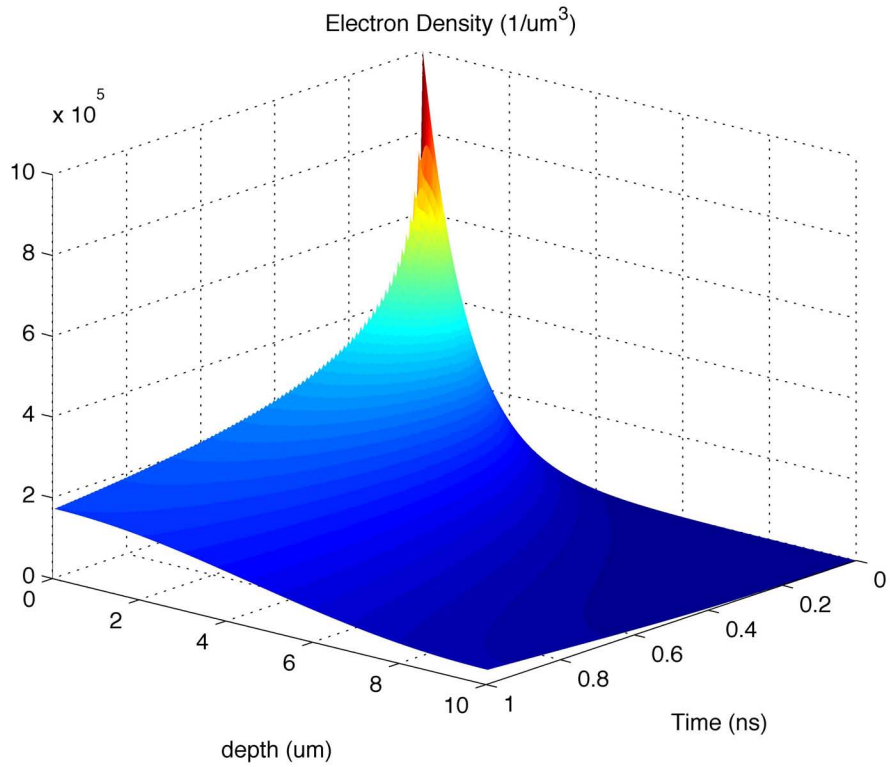

Figure 2.7: Electron density for GaAs, at a fluence of 0.25 mJ/cm^2, including contributions from Auger recombination and electron diffusion. Electron diffusion quickly reduces the carrier density at the surface, moving deep into the crystal at early times.

governed by the wave equation,

$$\frac{\partial^2 u}{\partial t^2} = v^2 \frac{\partial^2 u}{\partial z^2} \tag{2.6}$$

where

$$\eta = \frac{\partial u}{\partial z} \tag{2.7}$$

and u is the atomic displacement from equilibrium. Due to the contributions from the electronic component, the shape and speed of the impulsive wave differs signif-

icantly from the Thomsen model. The traveling wave in space and time, solved by Equation 2.6 is shown in Figure 2.8.

It is interesting to note that the temperature profile is heavily dependent on the Auger recombination and band gap. For every absorbed photon, the excess energy over the band gap ($h\nu - E_g$) is transferred to kinetic energy of the electron. After which, the temperature diffuses into the bulk and continues to rise for several nanoseconds from the large contribution of Auger heat. The temperature profile (Equation 2.3) in space and time is shown in Figure 2.6.

The carrier density, on the other hand, is an ever-decreasing monotonic process. Assuming an instantaneous generation, carriers diffuse into the crystal and are recombined with holes, quickly eliminating excess charge. The carrier profile (Equation 2.4) is shown in Figure 2.7. The strain profile is simply the sum of the thermal and electron density profiles, scaled by the respective coupling coefficients.

Decamp *et al.* found that in order to explain the dynamics observed in germanium, diffusion and Auger recombination must be present in the strain model. Previous x-ray diffraction experiments had analyzed data using the Thomsen model with only slight modifications to approximate non-thermal terms [1, 4, 6, 12]. To correctly analyze semiconductor dynamics, the differential relations (Equation 2.3, 2.4 and 2.6) must be solved numerically.

Summarizing the progression of dynamics and strain in photo-excited semiconductors: photons are first absorbed by electrons in the material. A portion of the photon energy, equal to the band gap, goes directly into promoting electrons to the conduction band. Excess energy, $h\nu - E_g$, is transferred to the lattice as heat. As carriers cool, they recombine, further heating the lattice. The total strain in the crystal is a scaled sum of the electron deformation and thermal distortion of the lattice,

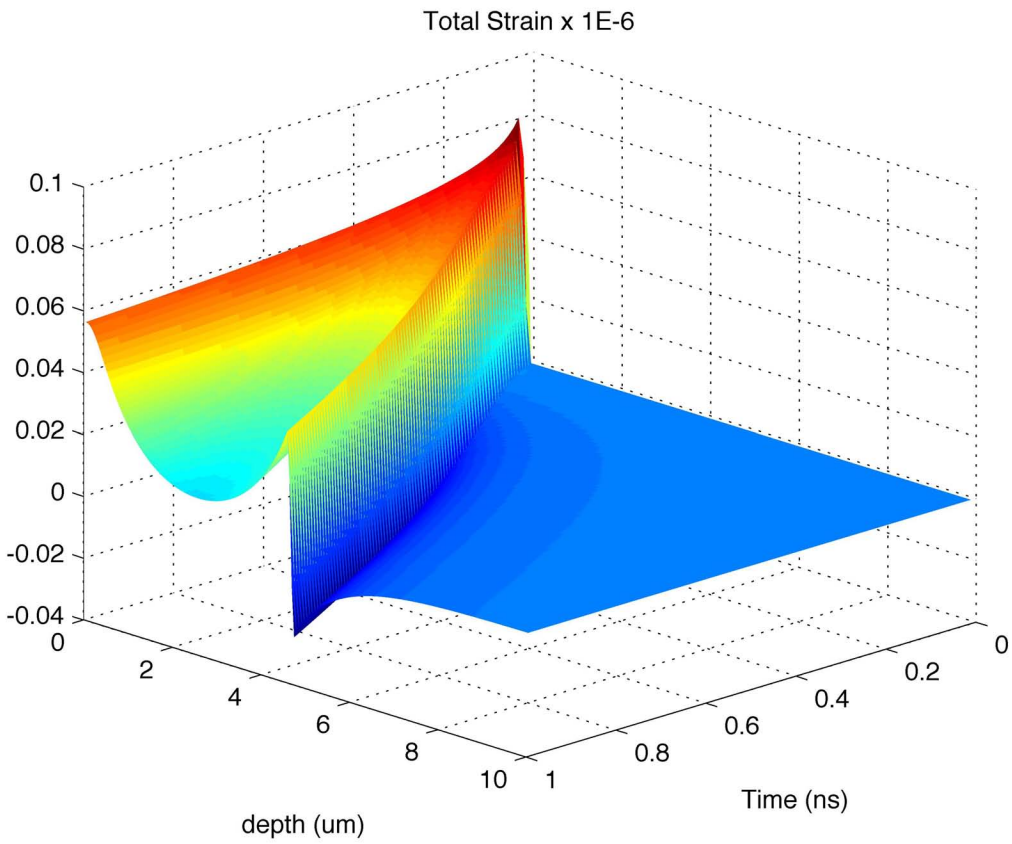

Figure 2.8: The absorption of energy at the surface of the crystal launches an acoustic bipolar impulse through the depth of the material. The Auger recombination and electron diffusion drive the wave, decreasing the deformation potential. This serves to balance the symmetry of the traveling wave. At 1 ns, the wave looks very similar to the Thomsen model since a large number of the electrons have been recombined. The thermal diffusion can be seen at the surface layer with an long-lived exponential decay.

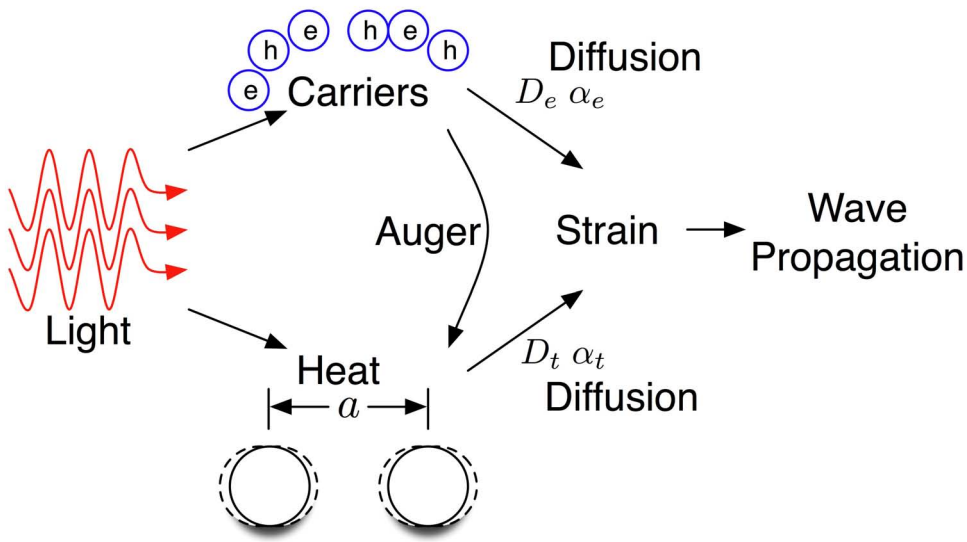

Figure 2.9: The evolution of ultrafast excitation involves several processes: carrier production, recombination, and thermal vibrations. These deform the lattice structure, producing strain which then propagates into the crystal.

where carriers and temperature continuously diffuse into the bulk material. These processes are illustrated schematically in Figure 2.9.

CHAPTER III

X-ray Diffraction in Ideal Crystals

In 1895 Wilhelm Rontgen demonstrated that x-rays had properties unlike visible light after producing the first x-ray radiograph showing the hand of his wife. In the years prior to this discovery the group theory of crystals had been published and, in 1912, M. von Laue proposed using crystals as a natural diffraction grating. He showed experimentally that crystals generated an interference pattern analogous to a periodic three-dimensional diffraction grating. In 1914, he received the Nobel Prize in Physics for his work in crystals. Immediately following, the father and son team of W.H. Bragg and W.L. Bragg proposed a different geometry with superior experimental techniques to probe the structure of crystals, work that won them the Nobel Prize in 1915. These inaugural experiments laid the foundation for the study of structure at atomic length scales.

This chapter will explore the theory of x-ray diffraction. The discussion is limited to perfect crystals, giving an overview of diffraction by x-rays in the Bragg geometry. A more thorough discussion of space groups, imperfect crystals, and other geometries is presented in Warren and Zachariasen [15, 16].

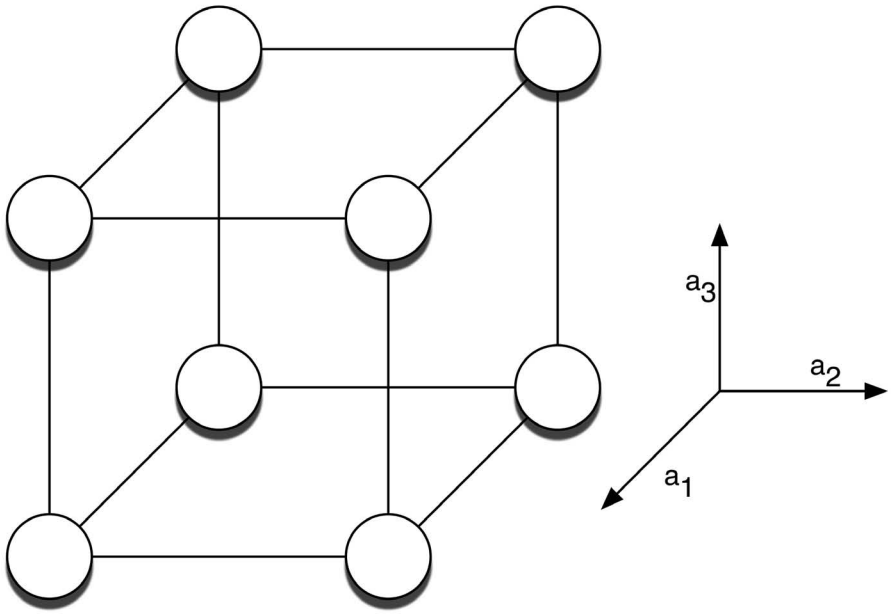

Figure 3.1: Three Dimensional representation of the unit cell defined by the crystal axis $\mathbf{a}_1\mathbf{a}_2\mathbf{a}_3$.

3.1 X-ray Diffraction

Diffraction is the process by which light produces an interference pattern after passing though a narrow aperture or sharp edge. As Laue showed, the periodic structure of crystals produces interference patterns similar to that of a grating. The basis for the first order solution to crystalline diffraction is based on Laue's assumption of the diffraction grating model. This method is commonly referred to as the wave kinematical diffraction theory. The diffraction grating condition requires the product of the distance between slits and the change in wave vector, $\Delta\mathbf{k}$, between the diffracted and incident beam, $\mathbf{k}_H$ and $\mathbf{k}_0$) respectively, be of integer value. The wave vectors are of equal magnitude $|\mathbf{k}_H| = |\mathbf{k}_0|$ and are defined along the unit vector of the incident and diffracted directions, $\mathbf{u}_{0,H}$ where $\mathbf{k}_{0,H} \equiv \frac{1}{\lambda}\mathbf{u}_{0,H}$ and λ is the wavelength of the

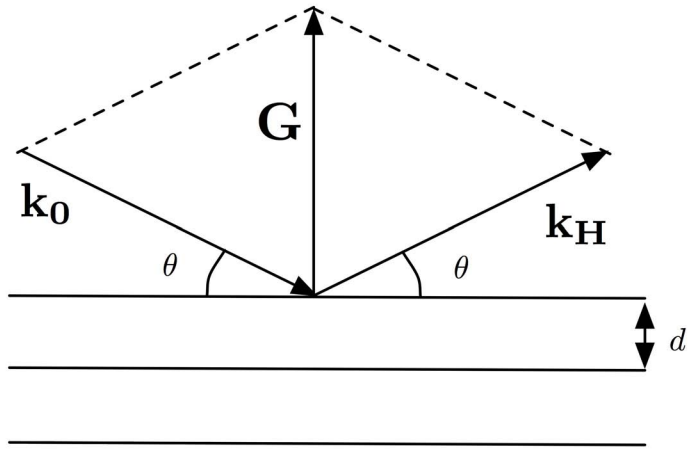

Figure 3.2: Relations involved in the vector representation of diffraction.

incident beam. The diffraction condition is

$$\mathbf{a}_i \cdot (\mathbf{k}_{H_i} - \mathbf{k}_0) = H_i \tag{3.1}$$

where H_i is an integer, $\mathbf{a}_i$ is the unit cell axis vector describing the periodicity of the crystal and measuring the separation of neighboring equivalent points. Each of these terms are indexed over three spatial coordinates where $i = 1, 2, 3$. It is then possible to describe any vector in the lattice by

$$\mathbf{r}_i = x_i\mathbf{a}_i + y_i\mathbf{a}_i + z_i\mathbf{a}_i. \tag{3.2}$$

where $0 \leq x_i, y_i, z_i \leq 1$. In three-space Equation 3.1 is known as the Laue vector equations and express the conditions to produce diffraction maxima.

It is convenient to express the unit cell geometry in reciprocal space. Defining the unit reciprocal lattice vector, $\mathbf{G}$, (see Figure 3.2) corresponding to an allowed reflection,

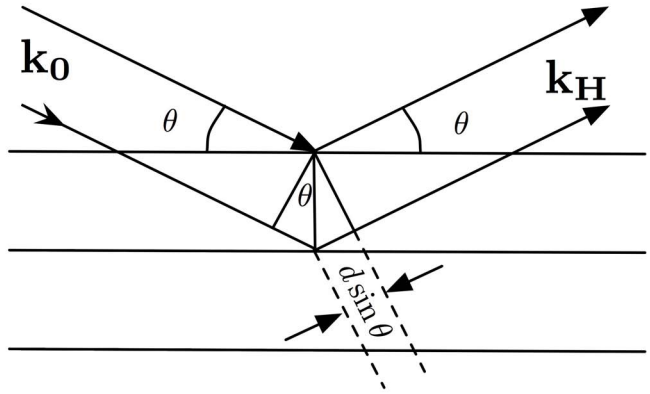

Figure 3.3: Vector representation of the Bragg Law.

$$\mathbf{G} = H_1\mathbf{b}_1 + H_2\mathbf{b}_2 + H_3\mathbf{b}_3 \tag{3.3}$$

with $\mathbf{b}_i$ being the reciprocal vector set of $\mathbf{a}_i$:

$$\mathbf{b}_1 = \frac{\mathbf{a}_2 \times \mathbf{a}_3}{\mathbf{a}_1 \cdot \mathbf{a}_2 \times \mathbf{a}_3} \tag{3.4}$$

$$\mathbf{b}_2 = \frac{\mathbf{a}_3 \times \mathbf{a}_1}{\mathbf{a}_1 \cdot \mathbf{a}_2 \times \mathbf{a}_3} \tag{3.5}$$

$$\mathbf{b}_3 = \frac{\mathbf{a}_1 \times \mathbf{a}_2}{\mathbf{a}_1 \cdot \mathbf{a}_2 \times \mathbf{a}_3} \tag{3.6}$$

where $\mathbf{a}, \mathbf{b}$ have the property $\mathbf{b}_i \cdot \mathbf{a}_j = \delta_i j$. By construction, the reciprocal lattice vector $\mathbf{G}$ is the difference in wave vectors of the incident and diffracted waves. This difference is also called the scattering vector, $\Delta\mathbf{k}$, where $\mathbf{G} = \mathbf{k}_H - \mathbf{k}_0 = \Delta\mathbf{k}$. If the scattering vector deviates from the Laue conditions, the diffraction pattern does not produce constructive interference. That is, if the coefficients of the Laue condition, H_i, of the reciprocal lattice vector are not integers, there is no diffraction maxima. The set H_i is also known as the Miller indices hkl. The integers hkl define $\mathbf{G}$ to a

reciprocal lattice plane such that the distance normal between two planes is parallel to the vector set $\mathbf{a}_i$ by construction. The distance d of the interplanar spacing is given by $d = \hat{\mathbf{n}} \cdot \mathbf{a}_i / H_i = 1/|\mathbf{G}|$, where $\hat{\mathbf{n}} = \mathbf{G}/|\mathbf{G}|$. The Laue equations can then be written as

$$\mathbf{a}_1 \cdot \mathbf{G} = h, \qquad \mathbf{a}_2 \cdot \mathbf{G} = k, \qquad \mathbf{a}_3 \cdot \mathbf{G} = l. \tag{3.7}$$

From simple geometry (Figure 3.3), the path difference between the incident and diffracted wave vectors is $2\sin(\theta)/\lambda$. Combining this with the definition of the scattering vector $\Delta\mathbf{k} = \mathbf{G} = 1/d$, the Bragg law is derived:

$$|\mathbf{k}_H - \mathbf{k}_0| = |\mathbf{G}| \Rightarrow 2\sin(\theta_B)/\lambda = \frac{1}{d} \tag{3.8}$$

where the subscript B denotes a Bragg reflection.

3.2 The Structure Factor

When a plane wave is incident on a group of electrons, classical and quantum scattering theory allows for two scattering phenomena: inelastic and elastic scattering. Compton scattering is an inelastic process wherein some energy is imparted on an electron and diffracted radiation is Compton shifted to a longer wavelength. The inelastic scattering is incoherent in nature and represents the sum of intensities of scattering from individual atoms comprising the lattice. Since this scattering is both incoherent and independent of short and long-range order, it does not provide insight to diffraction at the Bragg peak and therefore to this discussion. The coherent, elastically scattered radiation, however, gives rise to interference and Bragg diffraction.

To calculate the unmodified scattering from the crystal, the charge density, ρ, in a volume dV must be assessed where the integral over the entire volume evaluates to a single electron, $\int \rho dV = 1$. The scattering amplitude from an electron is the volume integral of the charge density and the phase difference between the radiation scattered by the jth electron and the electron at the origin ($\mathbf{G} \cdot \mathbf{r}_j$),

$$f_0 = \int \rho e^{2\pi i \mathbf{G} \cdot \mathbf{r}_j} dV. \tag{3.9}$$

This phase term must be included because x-ray wavelengths are comparable to the distance between electrons. For any atom, the scattering power f_0 is a function of the radial dependence of the electrons, so that at small values of $\sin\theta/\lambda$, f_0 approaches Z, the number of electrons in the atom. The electron distribution can be calculated using the Hartree-Fock method [17].

The atomic scattering power, f_0, correctly describes the scattering amplitude from a free electron (a Thomson scattering event). If the case of a scattering event from a group of bound electrons — such as in a crystal — is considered, the scattering amplitude from a unit cell must be evaluated. The scattering power of the unit cell, F_0, replaces f_0 where the electron distribution function of the crystal lattice, Ω, replaces ρ, where

$$F_0 = \int \Omega e^{2\pi i \mathbf{G} \cdot \mathbf{r}_j}. \tag{3.10}$$

The function Ω can be found by superimposing the contributions from all electron

distributions throughout the crystal lattice,

$$\Omega(\mathbf{r}) = \sum_k \rho_k(\mathbf{r} - \mathbf{r}_k) \tag{3.11}$$

where $\mathbf{r}_k$ is the direction from the origin to the kth atom. It should be noted that ρ_k is not the same electron distribution of Equation 3.9 where ρ was the distribution from an atom in free space. In this case, the atoms are bound together (binding energy is non-zero) and this assumption is no longer valid. Furthermore, Equation 3.9 uses a classical view of the electron cloud. To fully account for all quantum effects, this picture must be replaced with a continuous band of virtual classical oscillators. The result of this correctly accounts for the cases with non-negligible anomalous dispersion, for which the index of refraction decreases with increasing frequency of the incident light. It is therefore necessary to label the scattering amplitudes f_0 and F_0 for which anomalous dispersion is not taken into account and where the subscripts are dropped for the cases when the dispersion corrections are included. It should be noted that it is common to see the scattering power of the unit cell referred to as the *structure factor* in many references. A more detailed theory of dispersion corrections is given in Zachariasen and Cromer [16, 17].

Quantitatively, the geometric part of the form factor, f_0, is calculated using the theoretical work of D. T. Cromer and J. B. Mann, to produce a set of nine coefficients (the Cromer-Mann coefficients) in a parameterization for neutral atoms given by

$$f_0 = \sum_{i=1}^{4} a_i \, e^{-b_i (\sin\theta_B/\lambda)^2} + c \tag{3.12}$$

which is valid for values of $0 \leq (\sin\theta_B)/\lambda \leq 2.0$ Å^{-1} and shown in Figure 3.4 [17]. The coefficients are listed in Table 3.1 for arsenide, gallium, indium, and antimony.

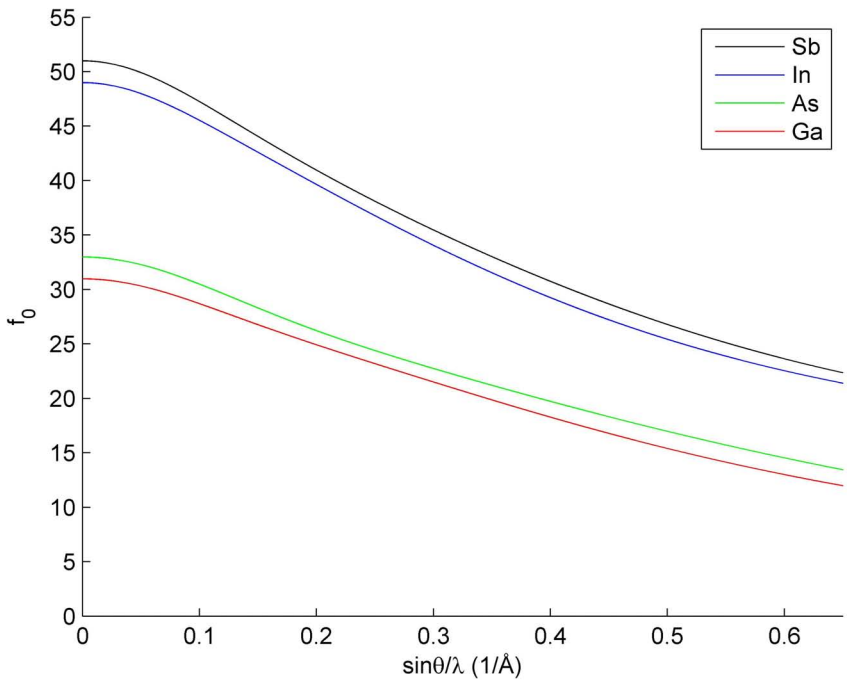

Figure 3.4: Non-Dispersive part of the atomic scattering factor for antimony, indium, arsenic, and gallium. Calculated using Cromer-Mann coefficients and Equation 3.12 [17].

The dispersion corrections, $\Delta f'$ and $\Delta f''$, are small and are expressed by

$$f = f_0 + \Delta f' + i\Delta f'' \tag{3.13}$$

where the imaginary part $\Delta f''$ represents a phase shift in the scattered radiation. This term will be important when analyzing the Bragg peak shapes. Since these corrections are a result of dispersion theory, they are dependent only on the frequency of the incident radiation and are independent of radial distribution or geometry of the given crystal.

The most drastic effects of anomalous dispersion manifest near or at an absorption edge, where the experimental uncertainty of these values are up to 15 - 20% very

Element	a_1	a_2	a_3	a_4	b_1	b_2	b_3	b_4	c
As	16.672	6.070	3.431	4.278	2.635	0.265	12.948	47.797	2.531
Ga	15.235	6.701	4.359	2.962	3.067	0.241	10.781	61.414	1.719
In	19.162	18.560	4.295	2.040	0.548	6.378	25.850	92.803	4.939
Sb	19.642	19.045	5.037	2.683	5.303	0.461	27.907	75.283	4.591

Table 3.1: Cromer-Mann coefficients for the geometric component of the atomic scattering form factor [17, 18].

near strong edges compared to $\leq 1\%$ uncertainty away from the absorption edges. Appropriate care must be taken around these absorption edges due to the discontinuities and singularities in the data (Figure 3.5). The dispersion corrections used to find the intensities of reflections are found experimentally and have been synthesized by Henke *et al.* [19]. In recent years, a database of these terms, collectively known as the *atomic form factors*, was created by the National Institute of Standards and Measures (NIST) [18]. By interpolating between data points, $\Delta f'$ and $\Delta f''$ can be estimated for any x-ray energy. The dispersion correction terms for arsenide, gallium, indium, and antimony are given in Table 3.2.

Correction	8 keV	9 keV	10 keV	11 keV	12 keV	13 keV
$\Delta f'_{As}$	-0.9136	-1.1922	-1.56186	-2.22129	-3.81902	-1.39895
$\Delta f''_{As}$	1.0169	0.82289	0.68078	0.57293	3.77479	3.21842
$\Delta f'_{Ga}$	-1.2629	-1.7348	-2.91219	-1.9114	-0.91121	-0.49946
$\Delta f''_{Ga}$	0.7857	0.63486	0.52471	3.45019	2.95286	2.61959
$\Delta f'_{In}$	0.1054	0.12455	0.07209	-0.01454	-0.11575	-0.22375
$\Delta f''_{In}$	5.0981	4.1778	3.49162	2.96388	2.54878	2.21616
$\Delta f'_{Sb}$	-0.0312	0.08996	0.09868	0.04877	-0.02907	-0.11992
$\Delta f''_{Sb}$	5.9588	4.8901	4.09321	3.47929	2.99569	2.60756

Table 3.2: Dispersion correction terms at several energies [18].

Recalling Equation 3.10 and accounting for the dispersion corrections, the struc-

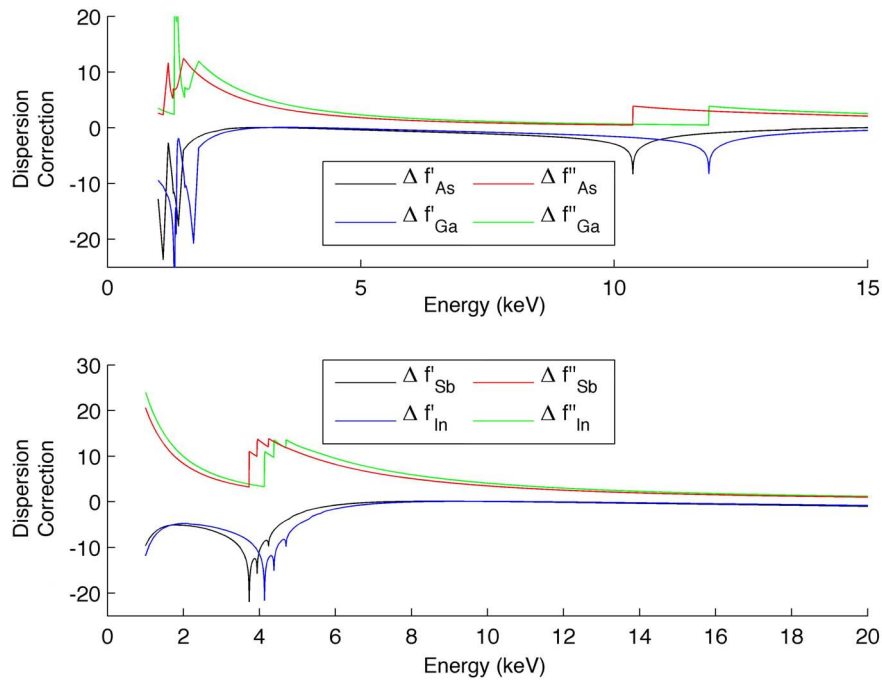

Figure 3.5: Dispersion Corrections $\Delta f'$ and $\Delta f''$ for antimony, indium, arsenic, and gallium. Data from NIST Atomic Form Factor database [18].

ture factor becomes the sum over the atoms in the unit cell,

$$F = \sum_k (f_k + \Delta f'_k + i\Delta f''_k) e^{2\pi i \mathbf{G}\cdot\mathbf{r}} \tag{3.14}$$

where F is now complex and can be written $F = F' + iF''$. The phase factor can be expanded into the unit cell and reciprocal lattice vectors, $\mathbf{a}_i$ and $\mathbf{b}_i$ respectively, where $\mathbf{G}\cdot\mathbf{r} = (h\mathbf{b}_1 + k\mathbf{b}_2 + l\mathbf{b}_3)\cdot(x_k\mathbf{a}_1 + y_k\mathbf{a}_2 + z_k\mathbf{a}_3)$ so that

$$F_{hkl} = \sum_k f_k e^{2\pi i (h\mathbf{b}_1 + k\mathbf{b}_2 + l\mathbf{b}_3)\cdot(x_k\mathbf{a}_1 + y_k\mathbf{a}_2 + z_k\mathbf{a}_3)} = \sum_k f_k e^{2\pi i (hx_k + ky_k + z_k)} \tag{3.15}$$

where x_k, y_k, z_k are the fractional coordinates defined by the Bravais lattice.

For the case of a simple cubic, the lattice basis has a single atom per unit cell

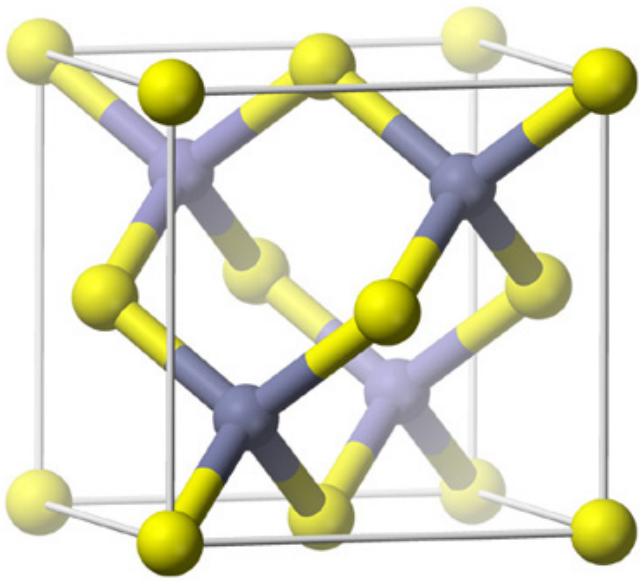

Figure 3.6: Model of the zinc blende unit cell. The diamond formation is that of the zinc blende where all atoms are identical [20].

located at the origin, or a fractional coordinates of (0,0,0). Plugging this into Equation 3.15, $F_{hkl} = f$. For a body-centered cubic (BCC) of a single element, the lattice contains two atoms with fractional coordinates (0,0,0) and $\left(\frac{1}{2}, \frac{1}{2}, \frac{1}{2}\right)$ giving $F_{hkl} = f[1 + e^{2\pi i(h+k+l)}]$. The zinc blende structure, shown in Figure 3.6, is the Bravais lattice of GaAs and InSb and contains eight atoms per unit cell. For GaAs, the unit cell contains 4 gallium atoms and 4 arsenic atoms with fractional coordinates shown in Table 3.3.

Ga	0	0	0	As	$\frac{1}{4}$	$\frac{1}{4}$	$\frac{1}{4}$
	$\frac{1}{2}$	$\frac{1}{2}$	0		$\frac{3}{4}$	$\frac{3}{4}$	$\frac{1}{4}$
	$\frac{1}{2}$	0	$\frac{1}{2}$		$\frac{3}{4}$	$\frac{1}{4}$	$\frac{3}{4}$
	0	$\frac{1}{2}$	$\frac{1}{2}$		$\frac{1}{4}$	$\frac{3}{4}$	$\frac{3}{4}$

Table 3.3: Fractional lattice coordinates for GaAs in a zinc blende structure

The choice of atomic origin is arbitrary so that f_{Ga} and f_{As} are interchangeable.

Plugging these coordinates in for x_k, y_k, z_k in Equation 3.15, the structure factor becomes

$$F_{hkl} = f_{Ga}[e^{2\pi i(0)} + e^{\pi i(h+k)} + e^{\pi i(h+l)} + e^{\pi i(k+l)}]$$
$$+ f_{As}[e^{\frac{1}{2}\pi i(h+k+l)} + e^{\frac{1}{2}\pi i(3h+3k+l)} + e^{\frac{1}{2}\pi i(3h+k+3l)} + e^{\frac{1}{2}\pi i(h+3k+3l)}].$$

F_{hkl} vanishes for terms where h, k, l are of differing parities. For those reflections $[(100), (210), (312), \text{etc...}]$ the scattering power is zero and the reflections are forbidden. The allowed reflections of the zinc-blende or diamond lattice has values of h, k, l which are all even or all odd $[(111), (200), (220), \text{etc...}]$. The structure factor of allowed reflections reduces to

$$F_{hkl} = 4\left[f_{Ga} + f_{As}\, e^{\frac{1}{2}\pi i(h+k+l)}\right]. \tag{3.16}$$

The diffracted scattering power, F_H is compared to the incident power, F_0 to find the relative refracted intensity where in the Miller formulation, $F_0 = F_{000}$, and is the structure factor for the incident wave.

Energy (keV)	F_{000}(InSb)	F_{400}(InSb)	F_{000}(GaAs)	F_{400}(GaAs)
8	400.27 - 44.23i	260.35 - 41.92i	247.13 - 7.21i	149.14 - 6.96i
9	400.83 - 36.27i	260.88 - 34.38i	244.12 - 5.83i	146.25 - 5.63i
10	400.66 - 30.34i	260.72 - 28.75i	237.94 - 4.82i	140.28 - 4.65i
11	400.11 - 25.77i	260.20 - 24.43i	239.30 - 16.09i	141.58 - 15.50i
12	399.40 - 22.18i	259.52 - 21.02i	236.91 - 26.91i	139.25 - 25.98i
13	398.60 - 19.30i	258.77 - 18.29i	248.24 - 23.35i	150.20 - 22.54i

Table 3.4: Structure factors for the (400) reflection at various energies for InSb and GaAs.

The effect of thermal vibrations in this discussion has so far been omitted. If, as a result of thermal vibrations, the lattice experiences large deviations from equilibrium

positions, atoms spend more time in the higher intensity wave field of the x-rays, leading to higher absorption. To account for this additional attenuation, the atomic scattering factor f_k is replaced by $f_k e^{-M_k}$ where M_k is the Debye-Waller factor for the kth atom. This is calculated from the average atomic displacement from equilibrium position, $\langle u_k^2 \rangle$, by

$$M_k = 8\pi^2 \langle u_k^2 \rangle \left(\frac{\sin^2 \theta}{\lambda} \right)^2 . \tag{3.17}$$

The Debye-Waller factor reduces the magnitude of structure factor, attenuating the diffracted intensity, as well as reduces the width of the diffraction peak. A summary of the atomic displacements is given in Table 3.5 which shows the temperature dependence. The effect of the Debye-Waller factor is more easily seen at high temperatures and high reflection angles.

Material	Element	100 K	200 K	400 K	600 K	800 K
InSb	In	0.006102	0.011711	0.023163	0.034671	0.046194
	Sb	0.005274	0.010085	0.019926	0.029821	0.039728
GaAs	Ga	0.003397	0.006038	0.011658	0.017368	0.023101
	As	0.002949	0.005201	0.010014	0.014909	0.019827

Table 3.5: Average atomic displacements for InSb and GaAs at various temperatures. Values shown in Å^2. Table adapted from [21].

3.3 Kinematic Diffraction

In the above sections, the scattering amplitude from a single atom and a unit cell was derived. The results from a unit cell must be extrapolated to estimate the diffracted intensity of a small crystal. To find the scattering amplitude for the entire crystal, a first order approximation might simply be to superimpose the contributions

of each unit cell across the entire crystal, with proper handling of the phase differences. The location of any unit cell from the origin can be found by the unit vector $\mathbf{A}_L = L_1\mathbf{a}_1 + L_1\mathbf{a}_2 + L_1\mathbf{a}_3$ where L_i is the lattice parameters for the associated directions $\hat{\mathbf{a}}_i$. The total scattering amplitude from a single unit cell located at $\mathbf{A}_L$ is $Fe^{2\pi i\mathbf{G}\cdot\mathbf{A}_L}$, where the phase difference is with respect to the unit cell at the origin. The total diffracted amplitude across all unit cells becomes

$$E_H = E_0\, F \sum_L e^{2\pi i\mathbf{G}\cdot\mathbf{A}_L} \tag{3.18}$$

and $E_{0,H}$ is the incident and diffracted electric field amplitude. Expanding the summation, assuming $N_1N_2N_3 = N$ is the total number of unit cells

$$\sum_L e^{2\pi i\mathbf{G}\cdot\mathbf{A}_L} = \sum_0^{N_1-1} e^{2\pi iL_1\mathbf{G}\cdot\mathbf{a}_1} \sum_0^{N_2-1} e^{2\pi iL_2\mathbf{G}\cdot\mathbf{a}_2} \sum_0^{N_3-1} e^{2\pi iL_3\mathbf{G}\cdot\mathbf{a}_3} \tag{3.19}$$

which can be reduced to the form

$$\frac{E_H}{E_0} = F \prod_{\mathbf{i}} \frac{e^{2\pi iN_i\mathbf{G}\cdot\mathbf{a}_i} - 1}{e^{2\pi i\mathbf{G}\cdot\mathbf{a}_i} - 1}. \tag{3.20}$$

Finally the fractional reflected intensity, I_H/I_0, is found by multiplying the ratio of the amplitudes with its complex conjugate to give

$$\frac{I_H}{I_0} = |F|^2 \prod_{\mathbf{i}} \frac{\sin^2(\pi N_i\mathbf{G}\cdot\mathbf{a}_i) - 1}{\sin^2(\pi\mathbf{G}\cdot\mathbf{a}_i) - 1}. \tag{3.21}$$

When the Laue condition (Equation 3.7) is satisfied, the scattering intensity reduces to

$$I_H = I_0 |F|^2 N^2 \tag{3.22}$$

This approach to solving for the scattering intensity has several assumptions that allow it to be an excellent first order approximation to perfect crystal reflections and serves as a good estimate for small, mosaic, or highly imperfect crystals. That is to say, this method is only acceptable for crystals comprised of a small number of unit cells, crystals that maintain short range order but not long range, or crystals with defects.

The obvious omission to this derivation is absorption. Two types of absorption occur in the crystal. In the first type, incident photons suffer true absorption through the photoelectric effect where electrons absorb energy and are promoted to a different band or ejected from the atom. Quantitatively, normal absorption is described through

$$\mu_n = \left(\frac{e^2}{mc^2}\right)\left(\frac{\lambda}{2\pi\epsilon_0 V}\right) F'' \tag{3.23}$$

where, again, F'' is the imaginary part of the structure factor in Equation 3.14, e and m are the charge and mass of an electron, c is the speed of light, ϵ_0 is the permittivity of free space, and V is the unit cell volume. Absorption along any other direction has a smaller coefficient since the absorption only depends on the depth from the surface where in a direction θ from the normal, $\mu_\theta = \mu_n \cos(\theta)$. The quantity μ is the fractional intensity decrease in the intensity per unit length where this absorption

obeys the Beer-Lambert Law,

$$I(z) = I_0 e^{-\mu z} \tag{3.24}$$

for any depth z. The theory presented above can be easily corrected for normal absorption by including $e^{-\mu z}$ to Equation 3.21.

In the second type of absorption, the incident beam interacts with the diffracted beam in a process known as extinction. This interference only occurs when the Laue condition is satisfied. Extinction can not be easily accounted for in the kinematical diffraction theory of Equation 3.21 and a new theory is necessary to accurately describe this physical process. This new theory is required to include the mutual dependencies of the incident and diffracted beams by creating a coupled system. This is done by modeling the interaction as coupled coherent oscillators and for this reason, is known as the dynamical theory of x-ray diffraction.

3.4 Dynamical Diffraction

The theory of kinematic diffraction makes an assumption that each unit cell of the crystal is independent of each other. To correct for this inaccuracy, the theory of dynamical diffraction was developed first by C. G. Darwin in 1914, and in a different formulation by P. P. Ewald in 1916. The theory has been updated and improved by many others, yet the greatest contribution was by M. Von Laue in which Maxwell's equations for a periodic complex dielectric constant were solved. In the Laue description, the wave field inside the crystal is considered as a single entity where the incident and diffracted beams coherently interact and energy is exchanged between the two (see Figure 3.7). It should be said that all three formulations are correct,

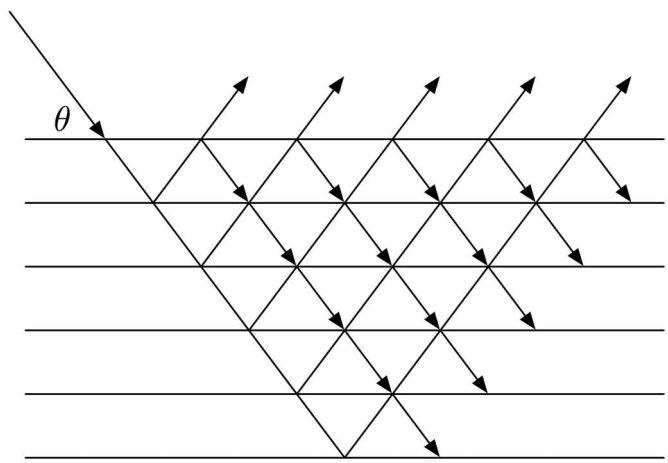

Figure 3.7: Dynamical diffraction illustration where incident and diffracted beams create a coupled system.

however the effects of absorption are implicitly included in Ewald and Laue. The discussion presented here only reviews the Bragg case of dynamical diffraction. A study of the Laue diffraction case[1] is given in Batterman and Cole [22].

According to the Darwin case — that is, no absorption ($Im(F_{hkl}) = F''_{hkl} = 0$) — the peak has a region of total reflection where $|I_H/I_0| = 1$ (blue curve in Figure 3.8). In 1930, J. A. Prins adapted this work to naturally include absorption through the structure factor. The complex structure factor works to reduce the reflection intensity across the region of total reflection, yet more importantly, includes the asymmetry of the reflection (red curve in Figure 3.8). In general, the attenuation due to extinction (negative interference) is many times greater than that produced by true absorption. To physically explain extinction, the most intuitive approach is the wave field treatment. At the surface, the wave nodes are located at the atomic plane, at the low-angle side of the reflection. As the incident angle increases, the nodes move linearly with angle until the atoms rest on the antinodal plane at the high-angle side

[1]Laue diffraction uses a different geometry than Bragg diffraction and uses non-monochromatic x-rays to gain information on atomic structure.

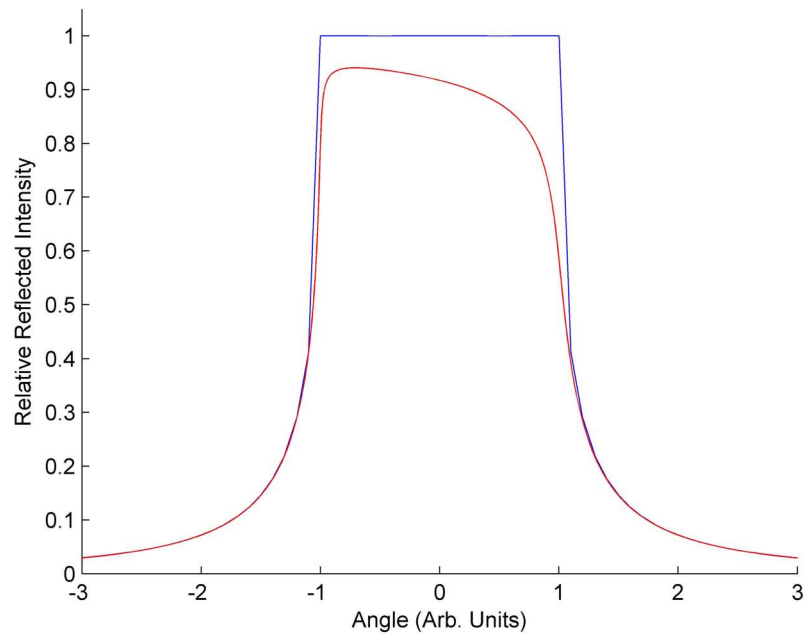

Figure 3.8: Darwin (blue) and Dawrin-Prins (red) rocking curves.

of the reflection range. As the atoms move into the higher amplitude wave field, the absorption contribution increases from each particle, giving rise to an asymmetric pattern. A cartoon of this shift is presented in Figure 3.9.

Another great advance to the efforts of this field came in 1962 and 1964 respectively, when S. Takagi and D. Taupin independently developed a dynamical theory which can be applied to a distorted or strained crystal [24, 25]. This theory removed any condition on thin crystals or small Bragg angles, treating the entire bulk as does the Laue formulation for the unstrained case by directly solving Maxwell's equations. The Takagi-Taupin equation is

$$\begin{aligned} i\tfrac{\lambda}{\pi}\boldsymbol{\beta}_0 \cdot \nabla \mathbf{D}_0(r) &= \psi_0 \mathbf{D}_0(r) + \psi_H \mathbf{D}_H(r) \\ i\tfrac{\lambda}{\pi}\boldsymbol{\beta}_H \cdot \nabla \mathbf{D}_H(r) &= \psi_0 \mathbf{D}_H(r) + \psi_H \mathbf{D}_0(r) - \alpha_H \mathbf{D}_H(r) \end{aligned} \tag{3.25}$$

where the parameters are given in Table 3.6. The Taukagi-Taupin equation expresses

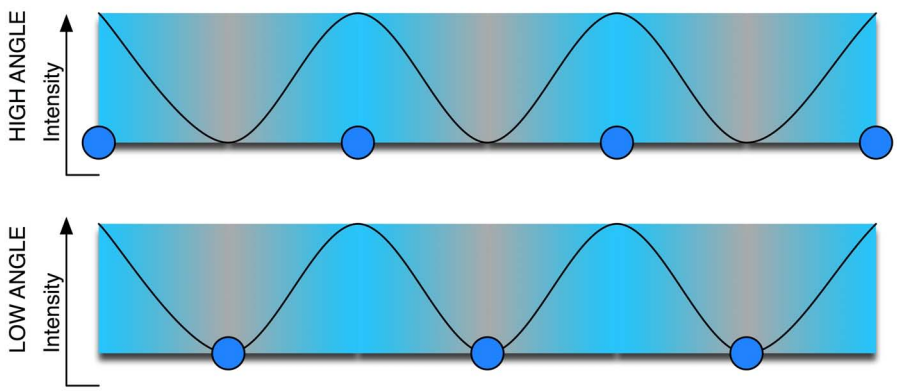

Figure 3.9: As the wave field moves from atoms residing at field nodes (lower figure) to having atoms at antinodes (upper figure), the absorption from an atom increases producing an asymmetric Bragg diffraction pattern. Figure adapted from [23].

the variation in the complex wave amplitudes in the incident and diffracted directions ($\mathbf{r}$). In 1986, C. R. Wie published a method to incorporate depth-dependent strain for an arbitrarily thick crystal [26]. This method builds on the Takagi-Taupin equation and has been indispensable when modeling Bragg diffraction from strained crystals [1, 4–7, 14, 27].

3.5 Numerical Modeling

The Wie method begins at the infinite atomic plane and calculates the rocking curve for the unstrained case, or the infinite crystal solution. At each depth iteration, the rocking curve is again calculated where the top layer solution is the fully strained case and comparable to diffraction data. The implementation of this method is most efficiently done by using the inner loop to iterate depth and the outer to iterate angle. The set of parameters shown in Table 3.6 are necessary for the Wie method [26, 28].

For F_H, the term in the exponential $\left(\exp[-(8\pi^2 \sin^2\theta_B/\lambda^2)u^2]\right)$ is the Debye-Waller factor from Equation 3.17 and can be taken into account when the structure

Wave Vectors:	$\boldsymbol{\beta}_{0,H}$
Complex Wave Amplitudes:	$\mathbf{D}_{0,H}(r)$
Polarizability per Unit Volume:	$\psi_{0,H} = -(e^2/mc^2)(\lambda^2/\pi^2)(F_{0,H}/V)(1/4\pi\epsilon_0)$
	$\psi_{0,H} = \psi'_{0,H} + i\psi''_{0,H}$
Structure Factor:	$F_0 = F_{000}$ and $F_H = F_{hkl}$
Unit Cell Volume:	V
Normalized Depth:	$A = z\pi\lvert\psi'_H\rvert/\lambda\sqrt{\gamma_0\gamma_H}$
Depth inside the crystal:	z
Direction of Cosines:	$\gamma_{0,H}, b = \lvert\gamma_0/\gamma_H\rvert = 1$ for symm. reflections
Incident Absorption Parameter:	$g = (1+b)\psi''_0$
Diffracted Absorption Parameter:	$k = \psi''_H/\psi'_H$
Deviation from Bragg Angle:	$y = \left[(1+b)\psi'_0 - b\alpha_H\right]/(2\lvert\psi'_H\rvert\sqrt{b})$
Displaced Structure Factor:	$F_H = F_H^0 \exp[-(8\pi^2\sin^2\theta_B/\lambda^2)u^2]$
Average Atomic Displacement:	u
Angle of Reflection:	$\alpha_H = -2(\theta-\theta_B)\sin 2\theta_B - (c_1\epsilon_1 + c_2\epsilon_2)$
Strain Perpendicular to Surface:	ϵ_1
Strain Parallel to Surface:	ϵ_2
Strain Strength:	$c_1 = 2\sin\theta_B[\cos^2\phi\tan\theta_B \pm \sin\phi\cos\phi]$
($\phi = 0$ for all symmetric bragg cases)	$c_2 = 2\sin\theta_B[\sin^2\phi\tan\theta_B \mp \sin\phi\cos\phi]$

Table 3.6: List of parameters for the Wie method of calculating rocking curves.

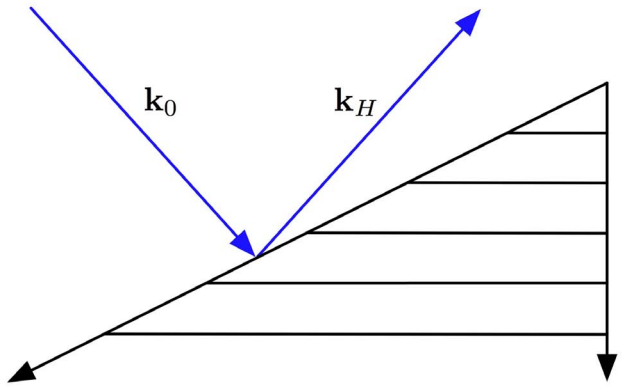

Figure 3.10: Example of an asymmetric Bragg reflection on a crystal cut such that the angle between the surface and reflecting plane is nonzero.

factor is calculated. The direction of cosines term b is to account for asymmetric Bragg reflections, where the crystal has not been oriented or cleaved along an atomic plane, in a geometry similar to Figure 3.10.

The scattering amplitude is given by the differential equation

$$i\frac{dX}{dA} = (1+ik)X^2 - 2(y+ig)X + (1+ik) \tag{3.26}$$

where $X = \sqrt{b}\frac{\mathbf{D}_H(r)}{\mathbf{D}_0(r)}$ is the scattering amplitude. Analytically integrating Equation 3.26 provides the iterative Wie solution,

$$X_{n+1}(A_{n,n-1}) = \frac{sX_{n-1} + i(B + CX_{n-1})\tan\left[s(A_n - A_{n-1})\right]}{s - i(C + BX_{n-1})\tan\left[s(A_n - A_{n-1})\right]}, \tag{3.27}$$

where A is dependent on the depth from the surface z, $B = -(1+ik), C = y+ig$, and $s = \sqrt{C^2 + B^2}$. A_0 is defined as the infinite crystal depth. The term s is not straight forward as it involves the square root of a complex number which must be carefully treated [26]. The notation of Equation 3.27 differs from that in Reference [26] where

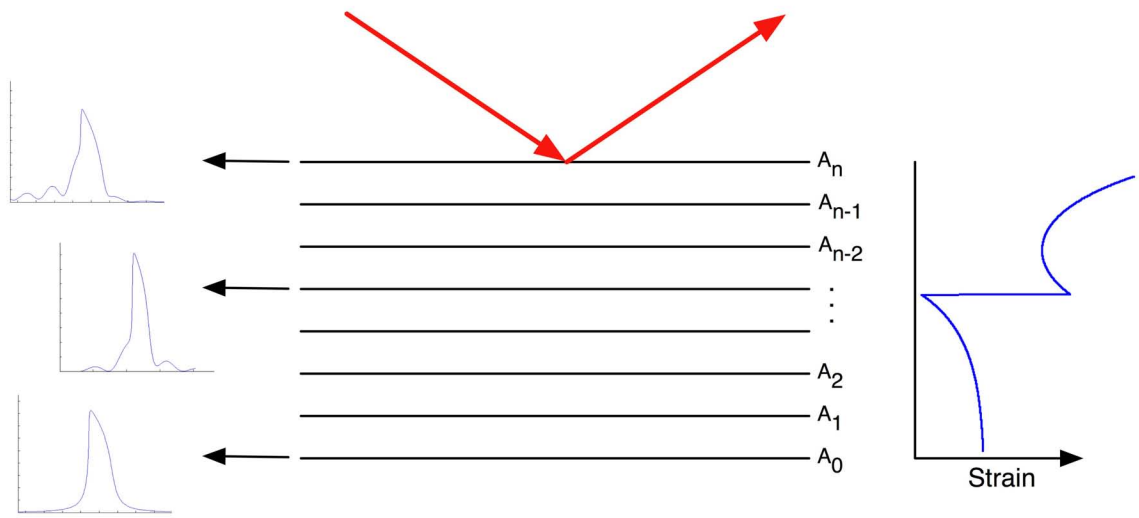

Figure 3.11: A schematic of the Wie algorithm. The solution originates at the infinite crystal solution depth (no strain) and builds a rocking curve at each layer towards the surface. The top layer solution gives the appropriate dynamical diffraction solution.

the subscript $n, n \pm 1$ are omitted. The Wie algorithm begins deep within the crystal where no strain exists, and the diffraction pattern is that of a perfect crystal. Then, it is imposed that at the maximum crystal depth (A_0), $X(A_0) = X_0$. A process schematic for the Wie method is given in Figure 3.11. This relation is easily derived from Equation 3.27, where the notation found in Reference [26] is used, setting the left hand side to X_0,

$$X_0 = \frac{sX_0 + i(B + CX_0)\tan(s(A - A_0))}{s - i(C + BX_0)\tan(s(A - A_0))}. \tag{3.28}$$

Collecting terms of X_0,

$$0 = BX_0^2 + 2CX_0 + B$$

and solving for X_0 gives

$$X_0 = \frac{-C \pm \sqrt{(C^2 - B^2)}}{B}$$

where the minus sign gives the appropriate and physically significant solution

$$X_0 = -\frac{B}{C - \sqrt{C^2 - B^2}}. \tag{3.29}$$

The infinite solution produces curves such as those shown in red in Figure 3.12. Strain in the crystal distorts the diffraction peak resulting in larger peak widths, reduced intensities and creates ripples off the Bragg peak. Experimental diffraction data usually can not resolve the sideband structures shown here as the angular divergence and energy spread of the x-ray beam are too large; however these distortions of the diffraction peak do appear as asymmetric peak shapes in strain crystal structure.

3.6 Comparison with $\chi_{0,H}$

To test the accuracy of the Wie calculation, an x-ray database that calculates crystal susceptibilities (in this formulation $\chi_{0,H} = \psi_{0,H}$) for scattering and Bragg diffraction, created by S. Stephanov, is used [29]. This database is heavily used within the x-ray community as an accepted source for accurate calculations of angles, widths, intensities and line shape of Bragg peaks. The database can produce diffraction peaks for more than 100 samples at any energy from 5 – 700 keV. The limitation of this calculator is that it is only applicable to the unstrained crystal case and is directly comparable to only the infinite solution from Wie. Unstrained InSb and GaAs crystals are compared to the solutions of $\chi_{0,H}$ in Figure 3.13 and 3.14 at room temperature.

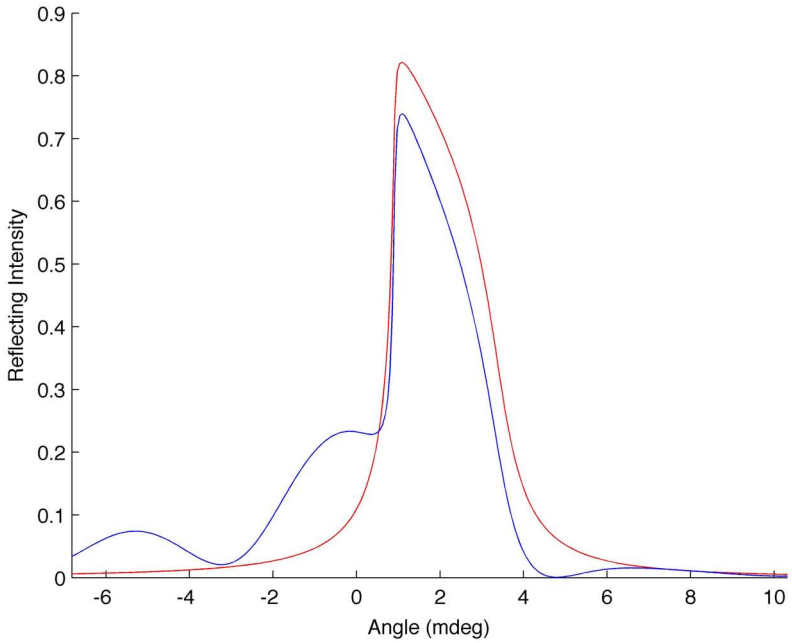

Figure 3.12: The unstrained crystal produces a smooth diffraction peak (red). After the strain has affected the crystal, the lattice deforms and produces lumps on either side of the peak (blue). Calculated using Equation 3.27 with a Thomsen model strain profile (Equation 2.2) for InSb. The wiggles on the sides of the peak are related to the phonon modes that exists in the crystal. A Fourier transform of the diffraction pattern will give the wave vectors present in the material.

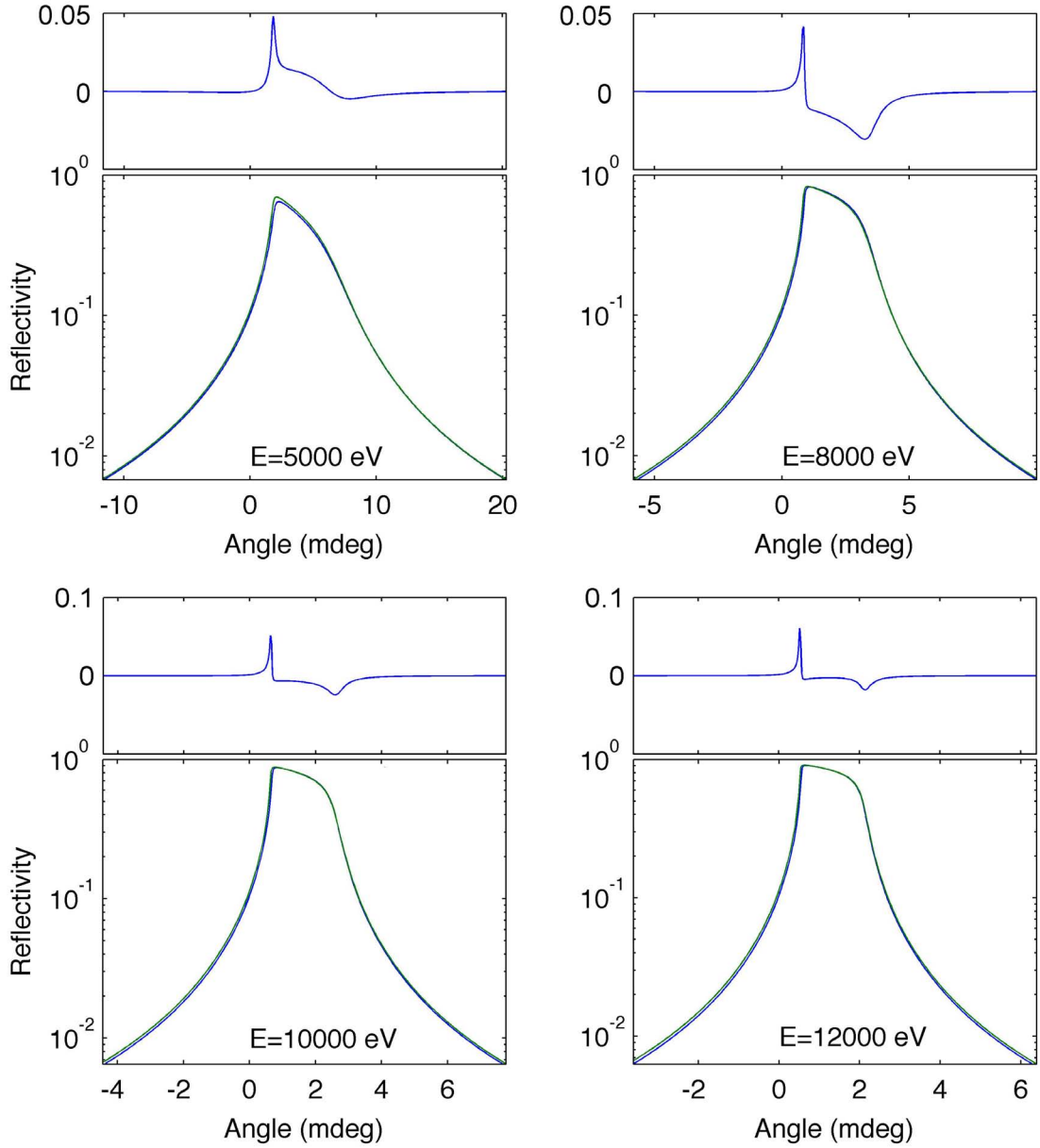

Figure 3.13: Direct comparison between the Wie ($\psi_{0,H}$) algorithm and $\chi_{0,H}$ for InSb at the (400) reflection. Wie is shown in blue, $\chi_{0,H}$ in green. A subtraction residual plot of the difference in the two algorithms ($\psi_{0,H} - \chi_{0,H}$) are shown above each plot. Sb absorption edge at 4.6984 keV.

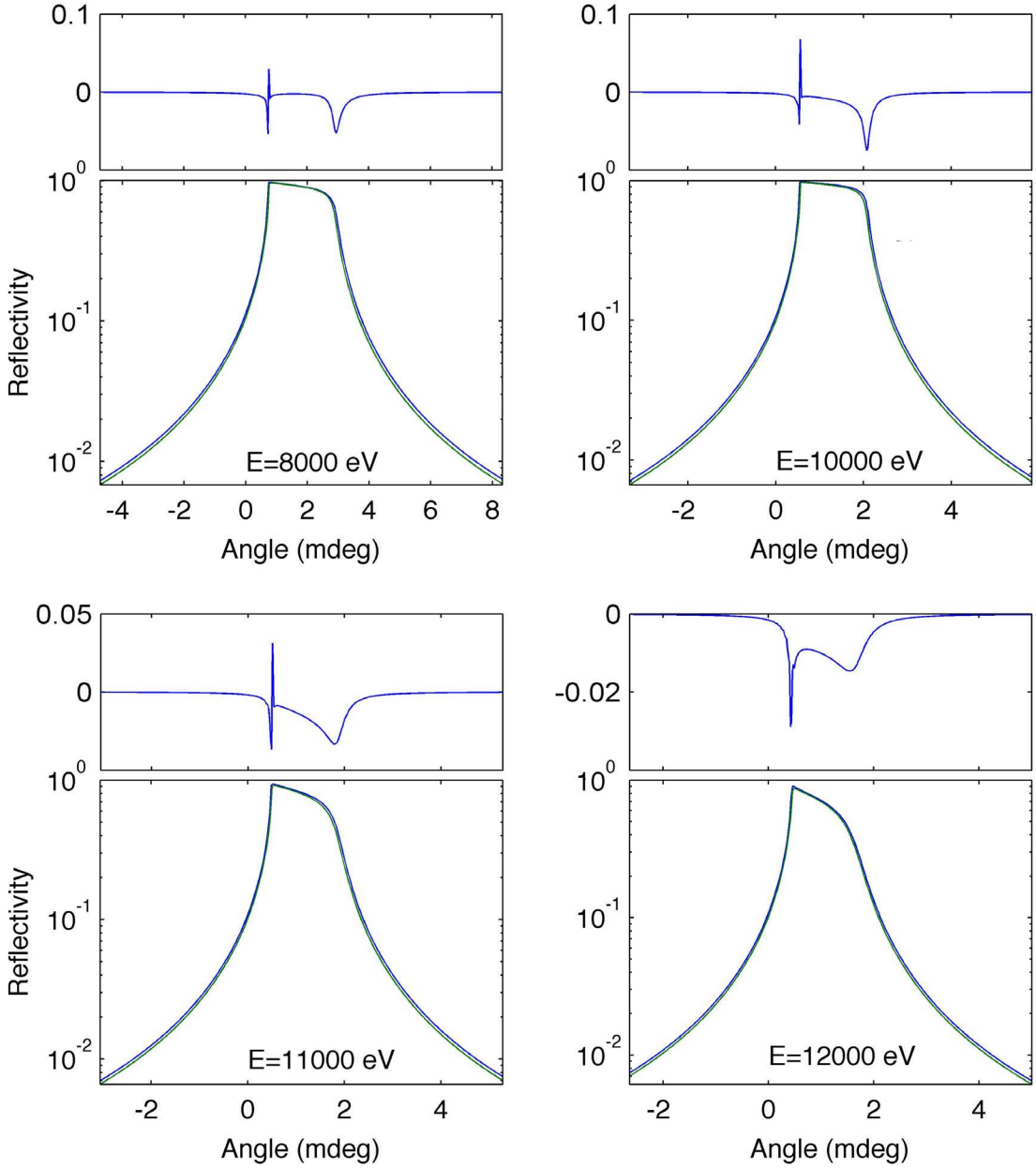

Figure 3.14: Direct comparison between the Wie ($\psi_{0,H}$) algorithm and $\chi_{0,H}$ for GaAs at the (400) reflection. Wie is shown in blue, $\chi_{0,H}$ in green. A subtraction residual plot of the difference in the two algorithms ($\psi_{0,H} - \chi_{0,H}$) are shown above each plot. Ga absorption edge at 10.3682 keV, As absorption edge at 11.865 keV.

CHAPTER IV

Experimental Setup

The experiments presented here were performed at the Advanced Photon Source (APS) at Argonne National Laboratory. The APS is a third generation synchrotron producing x-ray pulses near 1 Å in wavelength, allowing for precise measurements on the atomic scale. To produce x-rays of high brilliance, insertion devices (ID) are used at each of the 34 beamlines that comprise the APS. In addition, each beamline is equipped with a single bend magnet able to produce x-rays and support experiments. Sector 7 (7-ID) is part of the X-ray Science Division, operated by the Time Resolved Research Group, and was used to carry out the experiments of this study. Novel detector techniques were developed to use in time-resolved studies at 7ID for this study

4.1 X-ray source

Synchrotrons produce electromagnetic radiation through the acceleration of charged particles, usually electrons. At the APS, electrons are thermally emitted from a hot cathode and accelerated by an RF electric field in a linear accelerator (LINAC), after which bunches of electrons at 450 MeV are injected into a booster synchrotron where

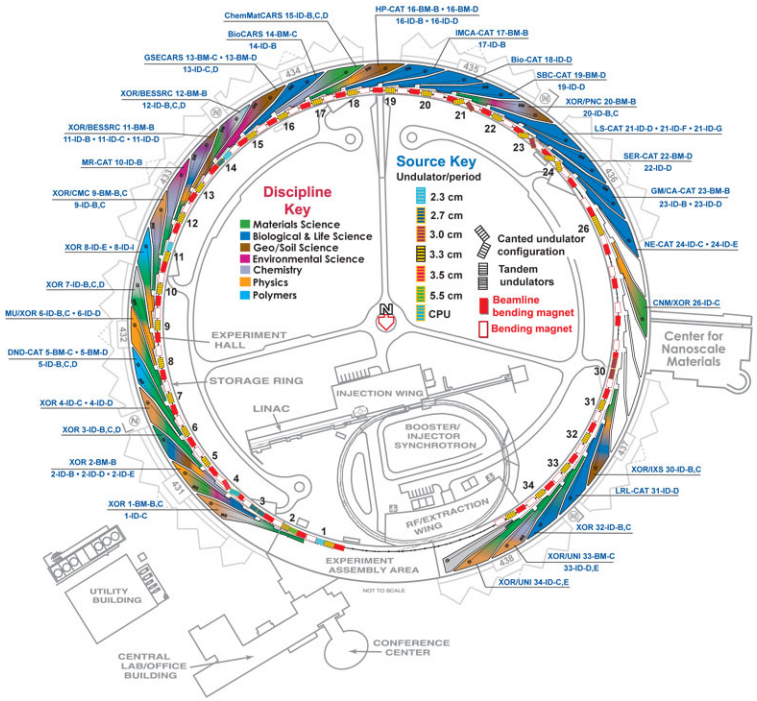

Figure 4.1: Schematic of experiment floor. Image taken from www.aps.anl.gov.

they are further accelerated (see Figure 4.1). The booster ring is synchronized to the outer storage ring with an external RF field.

The RF fields acts to compress individual bunches both spatially and temporally. The storage ring RF is set at 352 MHz where a single cycle defines a bucket, or electron bunch timing position. The APS has four operating modes with different electron distribution in the storage ring while keeping the average current constant through all modes. The standard operating mode consists of 24 bunches spaced evenly around the ring at about 153 ns apart. Other operating modes include 324 and 1296 bunch mode and a hybrid fill mode. Periodically, the extra electrons must be injected into the storage ring to keep the average current constant. In the standard operating mode, this is done by selecting a bunch and injecting additional electrons from the injector synchrotron. When this happens, the current in a single bunch will jump dramatically ($\sim$ 10 %), and is referred to as a top-up occurrence.

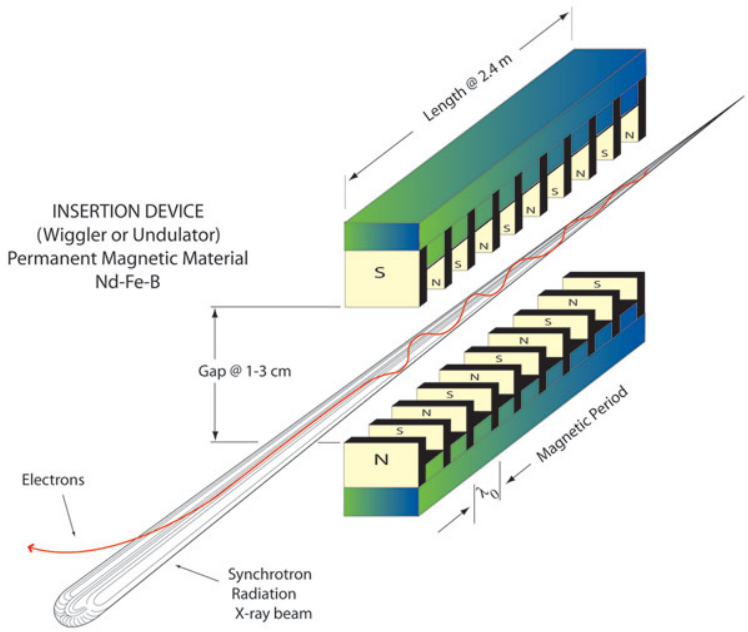

Figure 4.2: Schematic of undulator insertion device. Image taken from www.aps.anl.gov.

The APS storage ring circumference is 1104 m and contains more than 1,000 electromagnets to guide 7 Gev electrons traveling at nearly the speed of light. A third generation synchrotron like the APS is built in a geometry comprising many straight segments. At the intersection of two straight segments, a dipole magnet is placed in the electron beam to bend the electrons. The straight segments have insertion devices which produce the vast majority of the useable x-rays for each beamline. At the APS, most insertion devices are undulators, consisting of evenly spaced, alternating poled permanent magnets which vigorously accelerate electrons left and right, generating extremely bright x-ray pulses (see Figure 4.2).

When the direction of the magnetic field changes, the bunches accelerate (change directions) and emit photons. Since photons are released to conserve energy, the emitted photon wavelength is dependent on the strength of the magnetic field, B_0, the electron velocity, v_e, and the spacing of magnets in the undulator. The fundamental

wavelength, λ_1, of radiation from an undulator is related to the periodicity of the undulator, λ_u, by

$$\lambda_1(\theta) = \frac{\lambda_u}{2\gamma^2}\left(1 + \frac{K^2}{2} + (\gamma\theta)^2\right) \tag{4.1}$$

where θ is the angle between the undulator axis and observation,

$$\gamma \equiv \frac{1}{\sqrt{1-\beta^2}} = \frac{1}{\sqrt{1-\frac{v_e^2}{c^2}}}$$

and

$$K = \frac{eB_0\lambda_u}{2\pi m_e c} = 0.934\lambda_u(\mathrm{cm})B_0(\mathrm{T}) \tag{4.2}$$

where e is the charge of the electron, m_e is the mass of the electron, and c is the speed of light [23]. The relative bandwidth of the nth harmonic is

$$\frac{\Delta\lambda}{\lambda} \cong \frac{\Delta\omega}{\omega} \cong \frac{1}{nN} \tag{4.3}$$

where N is the number of magnetic poles in the undulator.

At sector 7, the undulator has a total length of 2.4 m with a magnetic period of 3.3 cm and produces photon fluxes of up to 10^{15} photons per second. The fundamental harmonic tuning range is roughly 3 to 12.5 keV, with a high harmonic generation able to produce 100 keV x-rays. For 24 bunch mode, the temporal pulse width of the x-rays is dictated by the electron bunch length of $\sim$ 70 ps at full width half maximum.

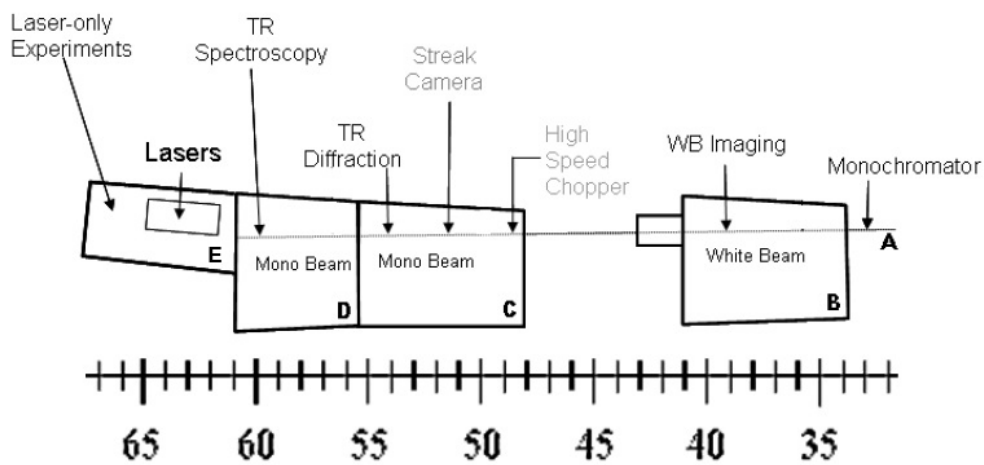

Figure 4.3: Sector 7 beamline layout. TR = time-resolved. WB = white beam. Scale in meters from storage ring. Image taken from [30].

4.2 Beamline layout

The spatial profile and spectral distribution of the x-ray beam from the undulator are much too large for accurate x-ray diffraction measurements. Using Equation 4.3, the spectral bandwidth is on the order of $\sim 1\%$. In order to measure changes in diffraction peak shifts, it is necessary to reduce the spectral bandwidth to $< 0.01\%$. This is accomplished by using Bragg diffraction from a water-cooled diamond (111) double-crystal monochromator to reduce the energy bandwidth to $\Delta E/E = \sim 5 \times 10^{-5}$. By choosing either the fundamental undulator radiation or a higher harmonic, the beamline can produce monochromatic x-ray at energies from 3 to 24 keV.

These experiments were performed in the C hutch (7-IDC) (see Figure 4.3). This hutch is dedicated to time-resolved diffraction experiments using monochromatic beam. An amplified femtosecond laser is brought in from Hutch E by evacuated beam pipe through Hutch D. As the x-rays arrive in Hutch C, they pass a set of collimating slits (JJ slits), which confine the x-rays to ~ 1 mm $\times$ 0.5 mm, and a set

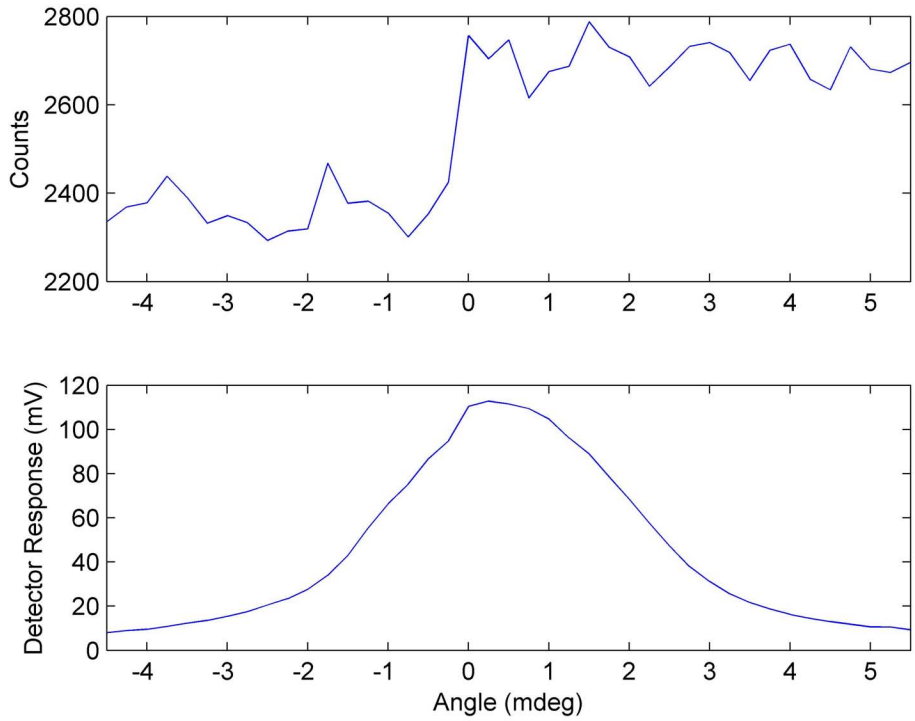

Figure 4.4: Top-up occurrence. The normalization detector (top) has a dramatic change in observed scattering events. The unexpected jump in diffracted intensity at the downstream detector (bottom) can be normalized to compensate for the jump. Data from Scan 784 on GaAs.

of attenuation filters before reaching a scattering foil. This foil has a low x-ray cross section and scatters only a small portion of the upstream x-rays where the scattered radiation is detected by a single photon counting detector. If a time resolved experiment is tracking a bunch that is topped up, the diffraction intensity will increase due to the increased photon flux. With this upstream detector, this additional intensity detected can be normalized, eliminating any discontinuous data (see Figure 4.4).

Beyond the upstream scattering detector are a pair of focusing Kirkpatrick Baez (KB) mirrors. The KB mirrors are 200 mm long, rhodium coated silicon trapezoidal mirrors in a helium-gas enclosure. The x-rays arrive at the sample, mounted on a six-circle Huber diffractometer. In the case of the experiments here, x-rays were

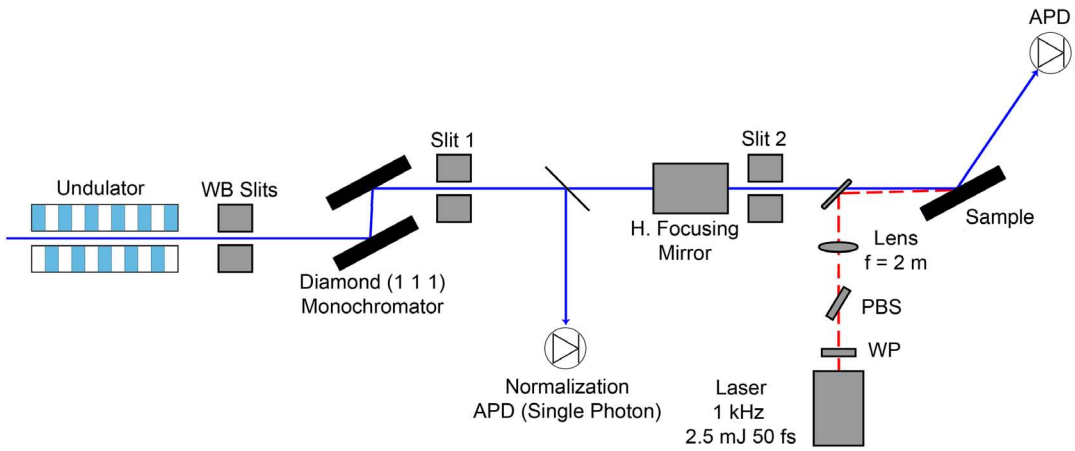

Figure 4.5: Experimental layout of a pump-probe experiment done at APS 7ID-C. WP = wave polarizer, PBS = polarizing beam splitter, WB = white beam.

focused to 20 μm horizontally and collimated with upstream slits to 50 μm vertically to achieve maximum x-ray intensity with minimal vertical divergence at the sample.

4.3 Pump-Probe X-ray Experiments

Ultrafast processes, which take place on the order of picoseconds or femtoseconds, are much too fast for any electronic detector system. To resolve effects with high temporal resolution, the shutter speed — or time over which the detector records information — must be on the order of the time scale of the action. It is then necessary to use ultrafast pulses of light to record ultrafast dynamics. If a long pulse, or continuous beam of radiation were used, the effects would be averaged over the length of the pulse and transient effects would be ignored. Therefore, in ultrafast experiments, very short pulses of light are needed to resolve the structural or optical properties of materials.

The experiments presented here consisted of an optical pump, x-ray probe setup. First a pump pulse being absorbed by the sample disturbing the structure of the material. At some fixed time later, a probe beam arrives. The change in system configuration can be inferred by the change in reflectivity, absorption, or diffracted intensity between the unperturbed and perturbed case. In the cases presented here, structural changes in crystal formation are examined using the change in x-ray diffraction. The pump beam is an optical-wavelength amplified femtosecond laser. An example of a pump-probe experiment layout is given in Figure 4.5.

In these x-ray experiments, samples are mounted on a six-circle Huber diffractometer. This has the capability of placing a sample at any orientation with respect to the incident beam. A crystal is rocked about a symmetric reflection on an axis perpendicular to the incident beam and parallel to the crystal planes, making an angle θ between the crystal and beam. Since the diffracted beam also makes an angle θ with the surface, the detector is positioned at an angle 2θ with respect to the beam. In the experiments presented here, the detector arm is left at a fixed 2θ position and the crystal is rocked about a Bragg angle, producing rocking curves. Additionally, the motors on the diffractometer controlling the changes in crystal orientation may be called by the orientation name (θ-motor, 2θ-motor, χ-motor, etc.).

4.4 Detectors

In order to record single diffraction events, detectors must be able to differentiate between x-ray bunches. This is essential to perform time-resolved experiments since low speed detectors average over multiple bunches losing the transient information recorded in each x-ray pulse. In normal operating mode, the bunches arrive nearly every 153 ns, therefore, it is required that the detectors completely recover from

residual changes resulting from the arrival of the previous bunch within $\sim$ 100 ns. The high-speed detector chosen for these experiments is a silicon avalanche photodiode (APD) which can be configured to be either a single photon counting device or a fast integrated intensity detector by adjusting the high voltage bias and amplifier gain.

4.4.1 Counting Mode

In photon counting mode, the APD is biased to nearly the breakdown voltage of silicon. This extreme biasing allows the detector to measure single x-ray events through a process known as avalanching. When photons of energy greater than the silicon energy gap are absorbed, an electron-hole pair is created and violently collides with other electrons due to the large bias. After a few collisions, the charge is enough to be detected by the electronics as a current. While the charge carriers exit the bulk of the silicon, the detector experiences a deadtime — a finite time needed to reestablish the biasing voltage, during which time the detector is unable to resolve additional photons. A detector deadtime underestimates the number of actual x-ray events and a statistical model must be used to estimate the actual number of counts. If a detector is dead for a time τ after each single event, the arrival of additional x-rays in the interval $0 \leq t \leq \tau$ is not counted. Additionally, the time needed to reestablish the bias is extended by a time $\delta\tau$. This is the extended deadtime model and is generally used for slower detectors such as scintillators using a single channel analyzer.

For the cases of fast detectors used at Sector 7 and other synchrotron-based applications, the model is slightly different [31]. If the deadtime is less than the x-ray pulse separation, any photons arriving during that time will be registered as a single

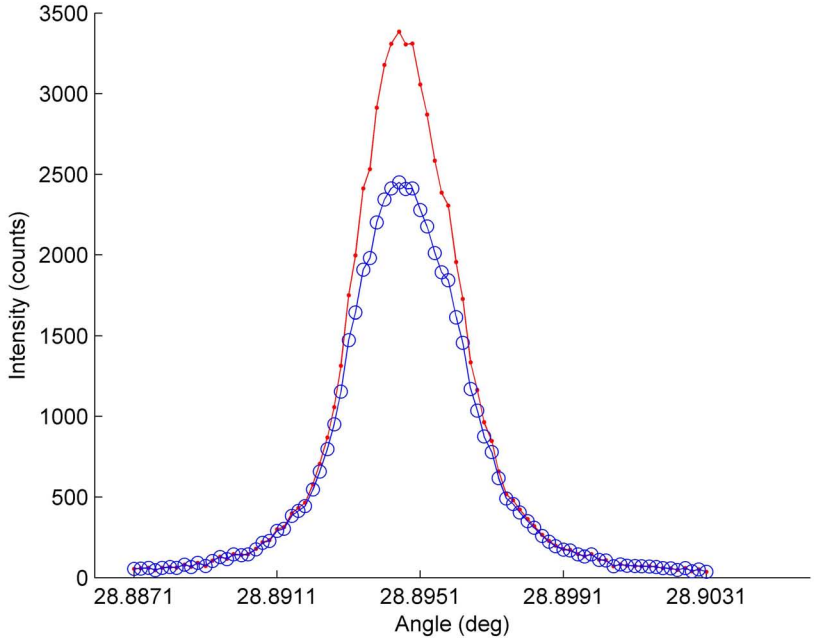

Figure 4.6: Deadtime correction for counting detectors. Observed counts shown in circles in blue, true counts in red. The number of true counts is given by Equation 4.4.

count. This is known as the isolated deadtime model and gives a true count rate of

$$N_T = -\frac{1}{\tau} \ln (1 - \tau N_O) \tag{4.4}$$

where N_T, N_O are the true and observed count rates. Figure 4.6 shows an example of the observed and true counts for an InSb reflection.

The associated uncertainty in the estimation of the true count rate is dependent on the statistical uncertainty in N_O given by the square root of the number of counts, $\sqrt{\sigma_{N_O}}$, and the uncertainty in the deadtime, σ_τ. The uncertainty in N_T, then, is found by propagating error in quadrature with respect to N_O and τ. The resulting

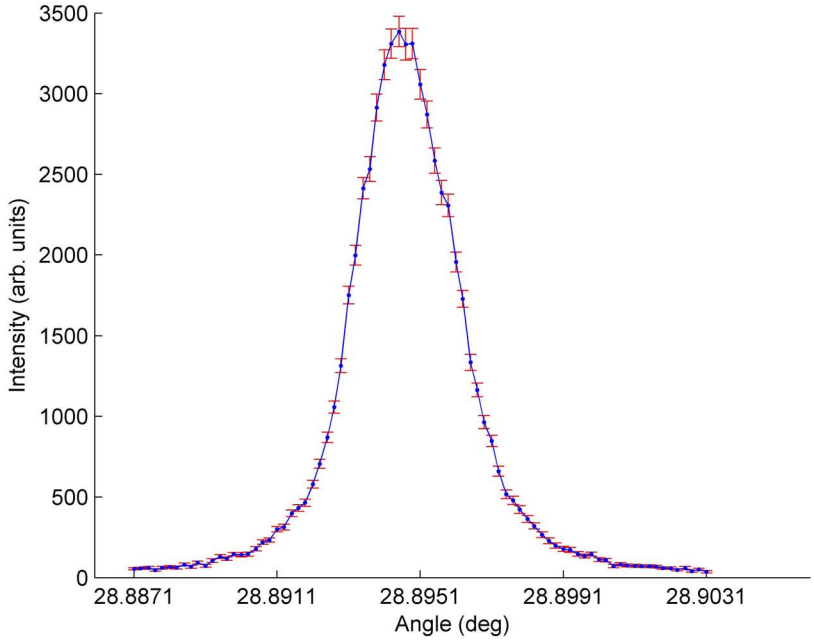

Figure 4.7: The counting statistics are slightly different for deadtime corrected measurements. Using Equation 4.5, error bars are fit to the corrected data.

relative error for the isolated deadtime model of Equation 4.4 is

$$\frac{\sigma_{N_T}}{N_T} = \frac{1}{N_T(1-\tau N_O)}\sqrt{\frac{N_O}{t}}. \tag{4.5}$$

When used in counting mode, the APD output is sent directly to a constant fraction discriminator (CFD). The CFD compares voltage pulses from the APD to a threshold level (typically $25 - 50$ mV) to separate signals originating from x-rays away from noise, which can be large at the output of a high-gain device such as an APD. The CFD outputs digital NIM signals which are then sorted into timing bins and individually counted.

4.4.2 Proportional Mode

When the APD is not critically biased, it can collect data using a proportional voltage mode. In this case, incident photons again create electron-hole pairs and an applied electric field moves them in opposite directions registering a current. The current is proportional to the number of incident photons and requires no deadtime corrections due to the ample number of valence electrons in the penetration depth of silicon and constant lower-voltage biasing. This method is very similar to that of an optical photodiode with a low bias. The output is recorded as a voltage reading with a constant error bound equal to the noise level of the APD. All efforts are taken to ensure that only diffracted x-rays arrive at the APD by shielding the detector with foil and black cloth as well as an extra set of slits on the detector arm.

There exists significant advantages to using an APD in proportional mode. Because of the high count rates associated with synchrotron radiation, counting mode often is plagued by high deadtime corrections which introduce significant uncertainty. In order to maximize the signal to deadtime error, the count rate is limited by reducing the number of x-rays in the monochromatic beam. In proportional mode, however, photon fluxes of up to 10^{13} photons per second, the maximum monochromatic flux at 7ID, are still within the linear range of the detector with proper choice of bias and gain.

4.5 Data Acquisition / Ztec Oscilloscope

For the proportional mode detectors, the x-ray pulse train is recorded through time. The analog voltage output is sent into a fast triggering oscilloscope to record the x-ray pulse shape and height. The APS systems control is an open source software

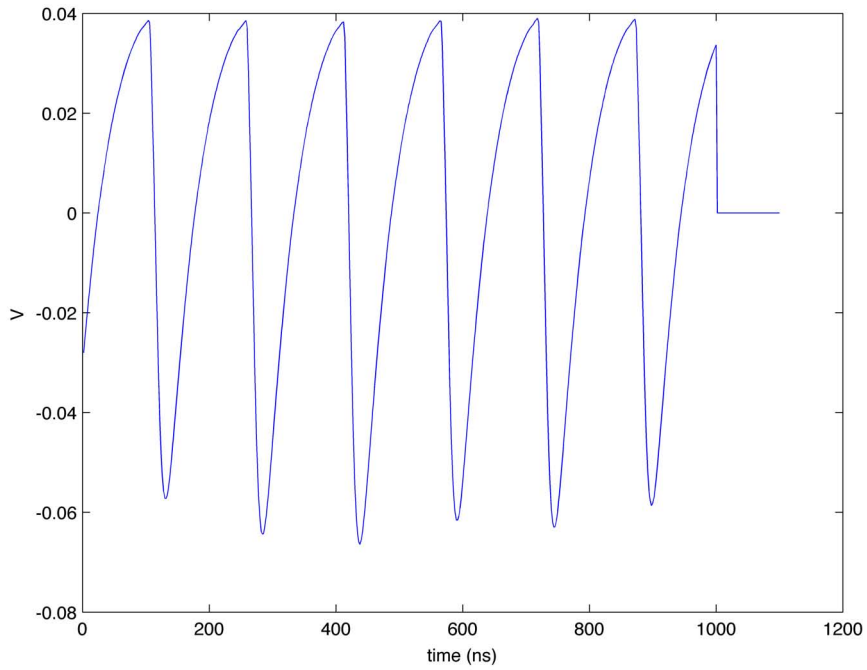

Figure 4.8: Raw data from averaged detector data in proportional mode. Figure shows negative-going spikes. The deviation in the pulse heights are due to the different current in each bunch. Data shown here has been averaged over 1024 triggers.

platform called EPICS, (Experimental Physics and Industrial Control System). In previous experiments where an oscilloscope was used, signals arriving from the detector were processed by an oscilloscope, then uploaded to a separate EPICS client, and finally uploaded to the EPICS servers. This processing and uploading has a finite time and results in the oscilloscope stalling, being unprepared for the next bunch and failing to trigger since it was still trying to offload data to the EPICS client.

The solution to this problem is a fast triggering oscilloscope that is a native EPICS client. In this situation, there is no need for an intermediate step and the oscilloscope passes data directly to the servers. Ztec Instruments provided an oscilloscope with exactly these specifications, able to sample every 2 ns, sufficiently fast for the recovery

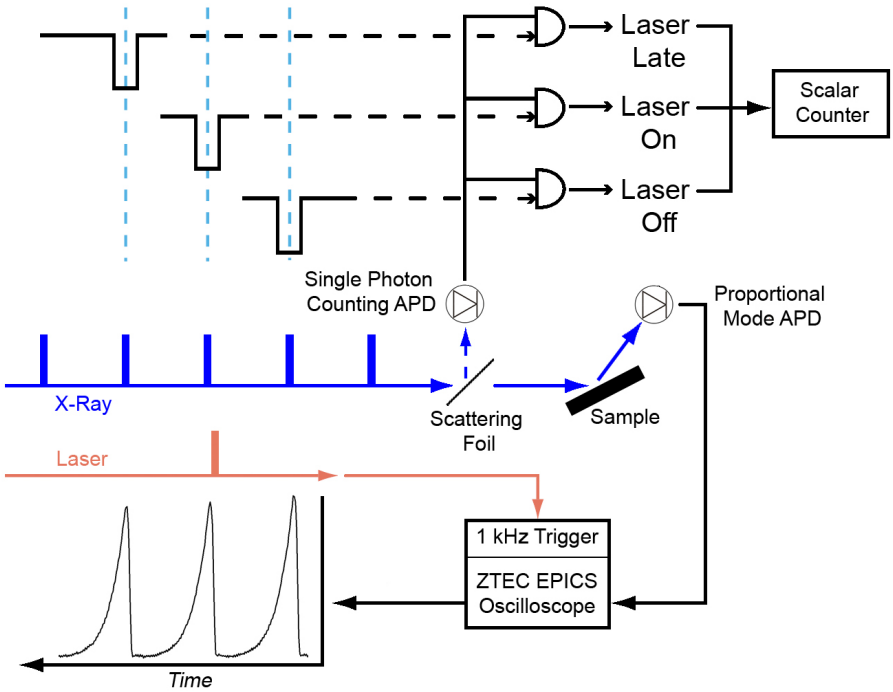

Figure 4.9: Timing diagram for a proportional mode pump-probe experiment at 7ID-C. When counting detectors are used, the detector outputs to a triggered analog to digital counter.

time of the APD ($\sim$ 75 ns). The Ztec will trigger every 1 kHz, given by the external triggering signal from the Pockels cell. The oscilloscope makes 1024 averages then offloads the data to the EPICS servers.

An example of the x-ray pulses, recorded by the Ztec oscilloscope, are shown in Figure 4.8 where the sharp negative edges are x-rays arriving at the detector and the curvature of the pulses is due to the recovery time of the APD since the x-ray pulses are only $\sim$ 100 ps long. Each pulse is segmented and a smoothing function is fitted to determine the peak height. The maximum value for each curve is recorded, defining the diffracted intensity for the particular x-ray pulse. Since the triggering is synchronized to the storage ring, each x-ray pulse corresponds to a particular electron bunch.

Typically, there are three bunches that are followed: laser-off, laser-on, and laser-late. Laser-on and laser-off are the x-rays immediately before the laser pulse arrives at the sample and immediately after the laser arrives. Laser-late is the second bunch after laser excitation. These three bunches gives the initial condition of the sample (laser-off), the excited state (laser-on), and the long time condition 153 ns later, showing thermalization (laser-late). A schematic of the timing system used for proportional mode is given in Figure 4.9

Running an experiment with proportional mode detectors currently has one major downfall. As an EPICS platform device, the oscilloscope is controlled using process variables (PV) files to carry out particular tasks. For the Ztec, technical problems such as reading in PVs, recalling saved PVs after a restart, and saving to the EPICS servers have been an ongoing issue. This is largely avoided by a specific protocol to load PVs and increasing the time between data points when the Ztec accesses the servers to upload data. This protocol is given in Appendix B.

4.6 Laser System

A titanium sapphire Kerr-Lens modelocked 20 fs laser oscillator (manufactured by Coherent, Inc) produces a pulse train at 88 MHz which is synchronized to the electron bunches in the storage ring to within 250 fs rms. The relative timing between the laser and x-rays is adjusted using an electronic phase shifter in the synchrotron feedback loop. The laser oscillator pulses are too weak ($\sim$2 nJ/pulse) to excite large amplitude motions in semiconductors and too frequent at the 88 MHz repetition rate to permit sample cooling between laser pulses. Therefore, single oscillator pulses are electro-optically selected by Pockels cells and amplified at a rate of 1 or 5 kHz up to energies of $0.5-2.5$ mJ/pulse using a regenerative chirped pulse laser amplifier (manufactured

by Coherent, Inc). The synchronization between x-rays and laser pulse is done using an antenna placed near the electron beam in the storage ring. This signal is amplified and filtered to produce an RF signal that is mixed with the output of a photodiode in the laser oscillator. The phase difference drives a piezo-mounted mirror to synchronize the laser. Delays between the x-ray and laser are generated electronically by phase shifting the electron beam RF.

CHAPTER V

Time-Resolved X-ray Diffraction

X-ray techniques may be employed to directly probe displacements at the atomic scale. In contrast, optical measurements are not directly sensitive to structural changes since the typical atomic spacing is on the order of 1 Å. An optical pump, X-ray probe technique is used to perform time resolved x-ray Bragg diffraction. At the APS, the temporal resolution is dictated by the bunch length of the electrons at $\sim$ 100 ps, averaging out any time-dependent effects below this limit. Given this restriction, information can still be extracted on the dynamics of strain by measuring rocking curves. Here, we present time resolved studies exploring strain generation and thermalization in InSb and GaAs semiconductor crystals.

5.1 Time Resolved X-ray Rocking Curves

As a crystal is rotated with respect to an incident beam of x-rays, it will pass through a geometry in which the three Laue conditions are simultaneously met and diffracted radiation will add coherently. In the Bragg geometry, the Laue conditions are satisfied by an angle θ_B, such that $d = \lambda/2\sin(\theta_B)$ where d is the distance between lattice planes and λ is the wavelength of the incident radiation. Due to the spatial

resolution of our experimental setup, Bragg peaks are best represented by a Gaussian distribution,

$$I(\theta) = I_0 e^{-\frac{(\theta-\theta_B)^2}{2(\delta\theta)^2}} + C \tag{5.1}$$

where I_0 and C are parameters defining the peak intensity and constant offset from zero, and $\delta\theta$ is the standard deviation which can be related to the full width at half maximum by $FWHM = 2(\delta\theta)\sqrt{2\ln 2}$. Knowing the wavelength and experimentally finding the Bragg angle, θ_B, the lattice parameter can be calculated.

There are several approaches to analyzing Bragg diffraction data. In this case, the aggregate change in lattice parameter is examined where Bragg peaks are fit to Gaussian distrobutions and the center position (centroid) is extracted. Using this information, these studies track structural change, Δd, in materials immediately after laser excitation. The position, however, is not the only information accessible with a rocking curve. The lineshape also contains information on the transient state of the crystal. This is summarized in Figure 5.1, where a broadened rocking curve indicates a portion of the probed crystal that has expanded or contracted in relation to the rest of the material.

As discussed in Chapter II, there are several hypotheses available to describe the dynamics of crystals under intense laser excitation. The Thomsen model states that all energy absorbed into the lattice is in the form of heat in the material. With this assumption, the temperature of a material can be measured by knowing the change in center peak position of the Bragg diffraction and linear expansion coefficient, β.

For example, if a 1.0 mdeg ($\Delta\theta/\theta = 0.0041\%$) shift in center peak position is observed for InSb at a Bragg angle of 24.5 degrees, the lattice expansion is 0.057

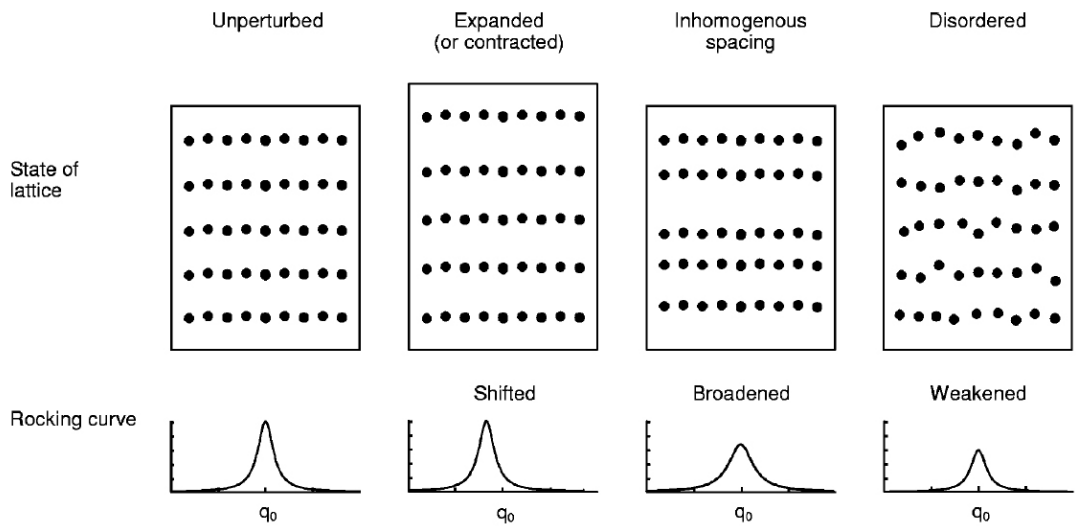

Figure 5.1: Rocking curves lineshape and position indicate the state of the lattice as transient effects pass through the penetration depth of x-rays. In these experiments, inhomogeneous spacing and lattice expansion are observed. Image taken from [32].

mÅ ($\Delta a/a = 0.0038\%$) and given a linear expansion coefficient $\beta = 5.37 \times 10^{-6}\,\mathrm{K}^{-1}$, the surface temperature rise of 7.1 °C. For any angle shift, $\Delta\theta$, the temperature jump can be calculated by

$$\Delta T = \left(1 - \frac{\sin(\theta_B)}{\sin(\theta_B + \Delta\theta)}\right)\frac{1}{\beta}. \tag{5.2}$$

The non-thermal effects following laser absorption, however, have a finite lifetime in the crystal. This approximation works well for long time periods after excitation (greater than 1 ns), but for the initial non-thermal regime (up to 750 ps), this calculation is not valid and underestimates the amount of stress in the lattice. In one case, the material responds linearly to absorbed laser fluence, qualitatively similar to the characteristics of the Thomsen model. In the other material, lattice response has a nonlinear fluence relationship.

To generate transient strain in these crystals, an 800 nm, 40 fs laser pulse illuminated the crystals, each cut in the [100] orientation. The optical penetration depth for InSb and GaAs are 0.1 μm and 1 μm respectively. The x-ray absorption depth is given by the imaginary part of the x-ray scattering susceptibility for the incident beam ψ_{0i}. The absorption factor μ_0 is given by $\mu_0 = (2\pi|\psi_{0i}|)/\lambda$ where the absorption length is $a_0 = \mu_0^{-1}$. For InSb and GaAs at 10 keV, the absorption length is 12 and 47 μm respectively. This value is only valid for cases when the Laue conditions are not met and there is no diffraction taking place. That is, this is the kinematical limit where the only attenuation effect is linear absorption and extinction (interaction between incident and diffracted waves) are negligible.

In the dynamical limit, when the Laue conditions are met the extinction length for a symmetric reflection is

$$L_{\text{ext}}^{Bragg} = \frac{\lambda \sin\theta_B}{\pi\sqrt{|\psi_H \psi_{\bar{H}}|}} \tag{5.3}$$

where ψ_H is the susceptibility of the diffracted beam and $\psi_{\bar{H}} = (\psi_H)^*$. The extinction length is the depth inside the crystal at which the intensity is attenuated by a value of e^2. The susceptibilities of these materials at arbitrary energies and reflections can be found using the computer program available in Appendix C.

The x-ray extinction depth for InSb and GaAs at 10 keV is 1.12 μm and 1.65 μm respectively, calculated using Equation 5.3. This is the depth at which x-rays probe into the sample at peak diffraction intensity, on top of the Bragg peak, when the effect is entirely in the dynamical regime. The differences between optical and x-ray extinction lengths allows for the distinction between the surface and bulk component of the impulsive strain wave. That is, the x-rays are able to probe well outside the

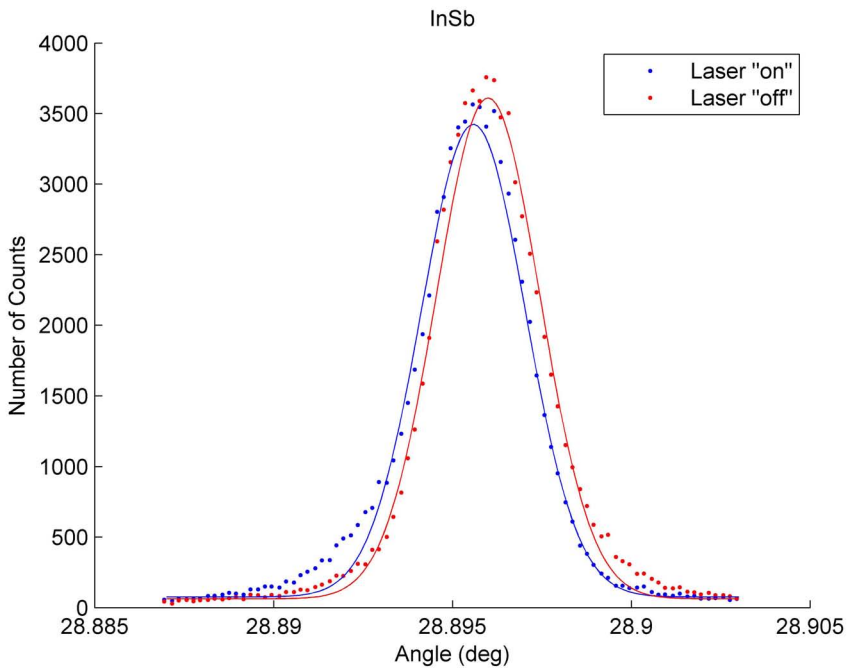

Figure 5.2: Rocking curves are fit to Gaussian distributions to extract center positions and standard deviations (FWHM) values. A disturbed (expanded) lattice is the result of ultrafast excitation (blue) compared to the equilibrium lattice (red).

penetration depth of the laser into the unperturbed crystal layers after excitation.

The symmetric (400) reflections of InSb and GaAs were observed, chosen since it is a strong reflection of zinc-blende structures. In each experiment data was collected with 10 keV x-rays and a spectral bandwidth of ~ 1 eV.

5.2 InSb Results

Rocking curves were produced with a pump-probe delay of 0 to 2.5 ns at absorbed fluences of 0.24 to 1.35 mJ/cm^2. At each time point, the rocking curve is fit to a Gaussian and the centroid extracted (see Figure 5.2). As the laser fluence is increased, the rocking curves are deformed with additional diffracted intensity on the low angle side of the peaks. This corresponds with an inhomogeneous lattice spac-

ing through the penetration depth of the x-rays. Extinction (destructive interference between incident and diffracted waves in the crystal) also plays a large role in the (400) reflection, further distorting the diffraction peak shape. At long time scales, the rocking curves remain significantly broadened indicating a persistent strain in the crystal. This is likely a result of thermal effects since heat takes a significant amount of time (hundreds of nanoseconds) to diffuse out of the extinction depth of the x-rays. Figure 5.3 shows rocking curves at 400 ps after laser excitation for a range of fluences. As the absorbed energy is increased, the low angle sidebands broaden and peak intensity decreases.

In order to determine whether the strain is induced thermally or electronicly, the centroid and full widths at half maximum of each rocking curve at each time point and each fluence are plotted in Figure 5.4 and Figure 5.5. By taking the centroid of the gaussian fit to a rocking curve, the average strain over the extinction depth of the x-rays is calculated. For InSb, the peak strain occurs at 400 ps, where the crystal quickly recovers to an equilibrium or quasi-steady-state lattice alignment. After 1 ns the rocking curve does not significantly change centroid position, signifying that the impulsive strain wave must be completely outside the probing depth of the x-rays, leaving behind only a thermally excited lattice. The width of the rocking curve gives an estimation on all parts of the extinction depth are thermalizing.

A measure of the full width at half maximum for each rocking curve is given in Figure 5.5. The InSb rocking curve width increases by nearly a factor of two in 200 ps, indicating that the lattice at the surface has expanded tremendously while the material deeper into the crystal remains unaltered. As the wave propagates and thermal energy diffuses, the width equilibrates with a 15% increase at the highest fluence. The quick recovery is evidence of thermally driven strain. The traveling wave

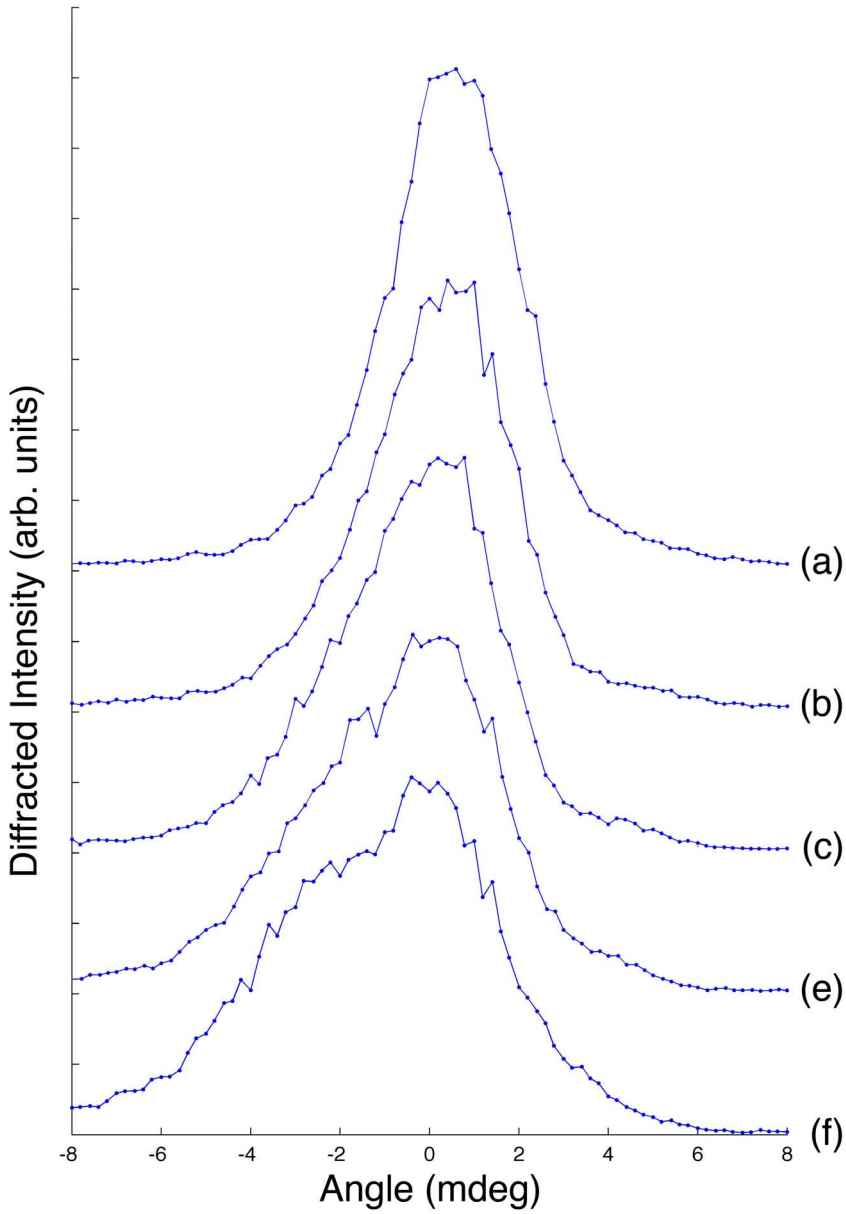

Figure 5.3: The lineshapes of InSb rocking curves significantly changes with absorbed laser fluence. The rocking curve of the lowest fluence (a) at 0.24 mJ/cm^2 begins to broaden as the fluence is incrementally increased to 0.46 (b), 0.74 (c), 1.05 (d), and 1.35 mJ/cm^2 (e). Here, the rocking curves broaden, shift, and decrease in amplitude denoting expansion and inhomogeneous spacing in the lattice. Plots are shown with a vertical displacement for clarity.

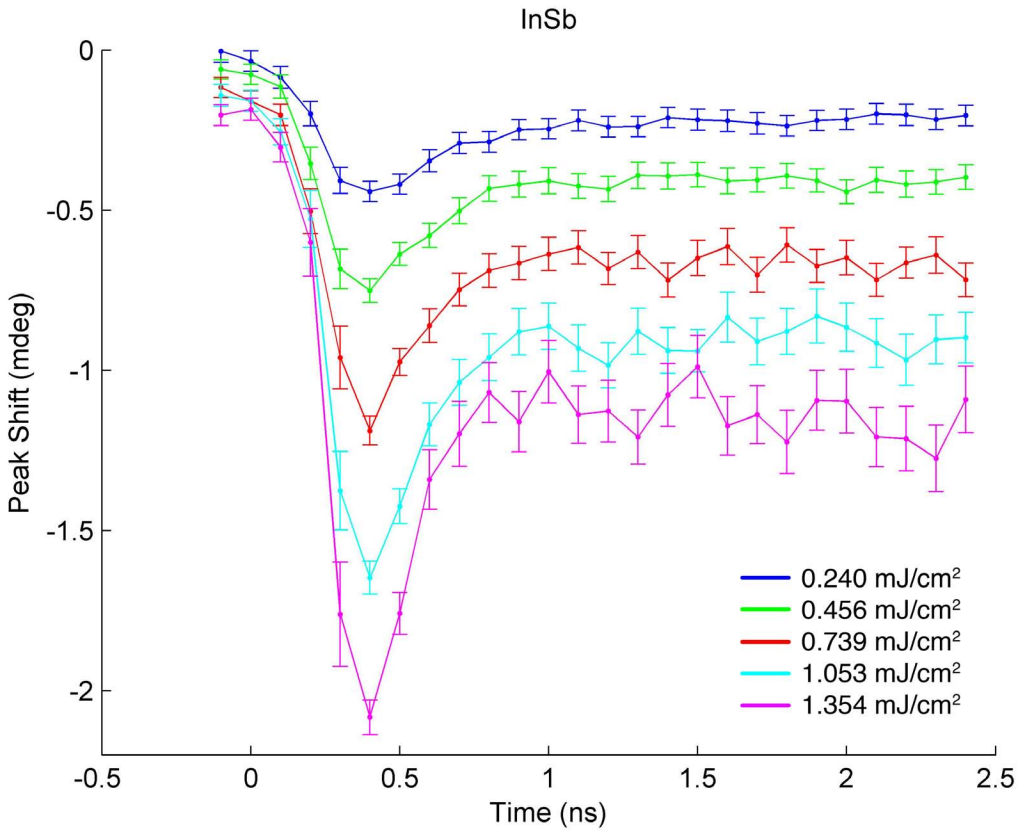

Figure 5.4: As an acoustic disturbance propagates into the crystal, the lattice responds by expanding (negative peak shift), followed by a recovery to a lattice at thermal equilibrium. Lattice expansion due to thermal contributions and transient effects are linear with fluence in InSb. Note that the lines connecting data points are there for visual aid and does not denote a model or fit.

propagates outside of the extinction depth leaving behind a temperature gradient which manifests as a slightly wider rocking curve. Here, there is no evidence that electrons play a role in the dynamic response of InSb.

Both the thermal heating and impulsive strain appear to be linear through the range of absorbed fluences. Additional data was collected suggesting that the peak strain continues to be linear up to the damage threshold of InSb. Figure 5.6 shows the peak strain (taken at 400 ps) and thermal strain (the average of centroid positions

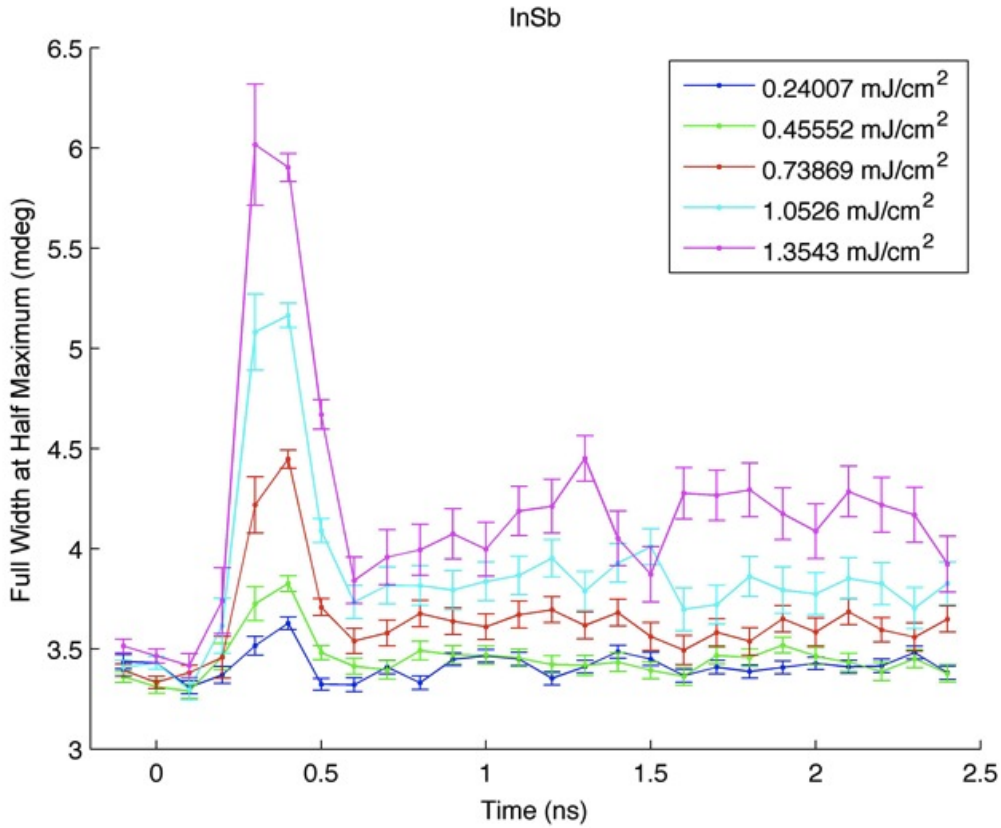

Figure 5.5: As the laser pulse is absorbed into the material and launches a bipolar strain wave, the lattice experiences inhomogeneous spacing, dramatically increasing the width of the Bragg peak.

from 1 to 2.5 ns) fitted with a linear slope versus laser fluence. The offset at time-zero is due to the inability of the crystal to cool in the 1 ms before the next laser pulse arrives. The rough curves are principally due to counting statistics and the inaccuracies in fitting gaussians to the asymmetric rocking curves (see Figure 5.3).

The counting statistics of the x-ray detectors used in this experiment (Equation 4.5) propagates into a weighted Gaussian curve fit used in determining the center of the rocking curve. The standard deviation of the fit parameter is extracted and plotted in Figure 5.4 and 5.6. The lower slope in Figure 5.6 uses an average uncertainty in the fit values between $1 - 2.5$ ns while the uncertainty in the upper slope

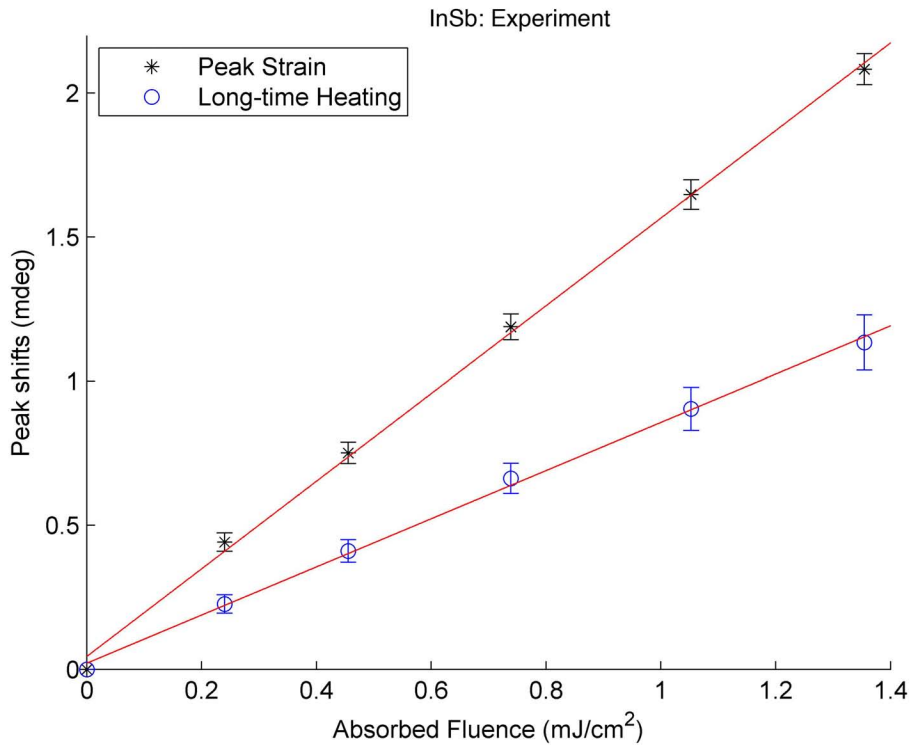

Figure 5.6: Peak (black) and thermal (blue) strain have a linear relationship with absorbed laser fluence. A linear fit was performed to each set of data, while a point at the origin was manually inserted.

are single values at 400 ps.

The linearity of InSb, with respect to both impulsive strain and thermal strain, is due to the partition of energy between thermal and electronic strains. InSb is frequently used as a near infrared detector since the band gap is only 0.17 eV, sensitive to photons of wavelength up to ~ 7.3 μm. When titanium sapphire laser light (1.55 eV) is absorbed, only a small fraction of the energy goes into promoting electrons, where almost all is deposited into the lattice as heat. It would appear that this is the physical limit of the Thomsen model with the vast majority of the energy is bundled as a thermally induced propagating wave. A discussion of the comparison and alterations to proposed models is given in Section 5.4. It is understood that the

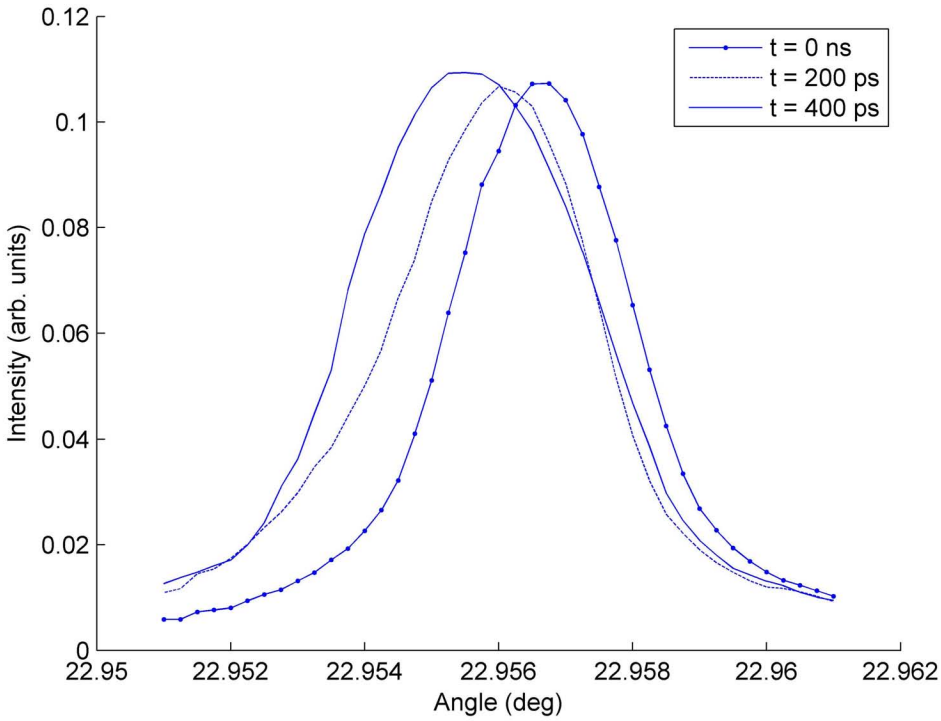

Figure 5.7: GaAs rocking curve for time-zero (solid with dot), 200 ps (dashed), and 400 ps (solid) after laser excitation. These rocking curves shift and broaden as the strain wave affects the lattice spacing.

response to heat in a crystal to be very linear, given by Equation 5.2 and shown in Figure 5.6.

5.3 GaAs Results

The sound speed, thermal expansion, and heat capacity are all very similar in magnitude between GaAs and InSb, yet the effects of laser excitation on the two materials are very different. This is at least partially due to the difference in band gap, which for GaAs is 1.424 eV. Therefore, the majority of the absorbed laser energy goes directly into producing electrons, leaving only a small remainder in the form of heat.

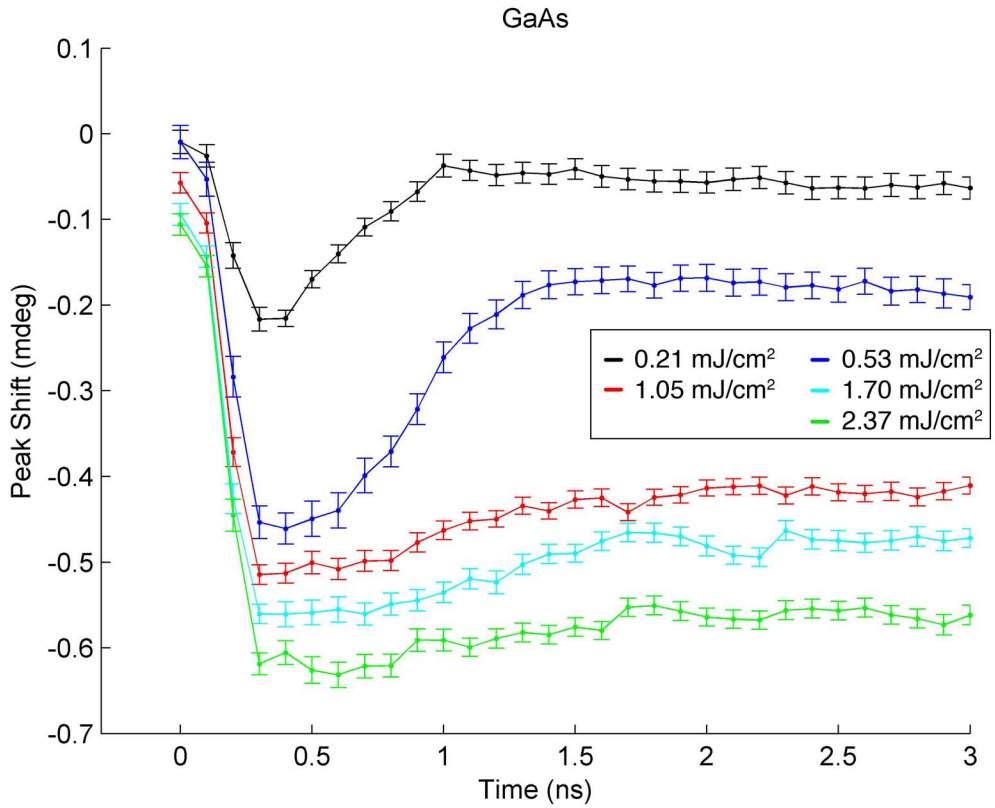

Figure 5.8: For low fluences, GaAs responses to laser-induced strain similar to InSb. As the crystal absorbs more energy, the response to the impulsive strain saturates, no longer responding in the linear manner seen in the low fluence case.

The GaAs rocking curve data again shows a centroid shift to the left indicating expansion of the lattice while also showing significant broadening of the lineshape as the impulsive strain wave moves through the crystal (see Figure 5.7). These rocking curves are exceptionally smooth due to the 1024 averages done in proportional mode, which is a great improvement over the InSb data set of highly distorted lineshapes taken with single photon counting detectors (Figure 5.3).

With this quality of data, Gaussian curve fitting produces very small confidence intervals. As well, since the measured uncertainty in the amplitude of diffracted intensity is a constant value of ~ 1 mV, further reducing the relative propagated error.

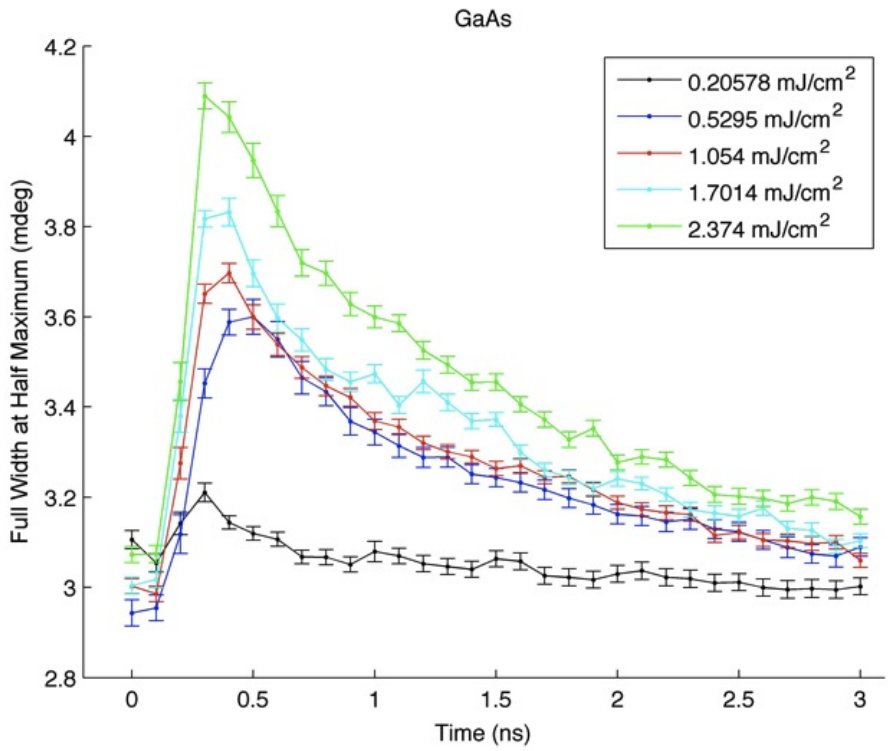

Figure 5.9: Time resolved changes in the rocking curve width of GaAs indicates a significant contribution from the energetic electrons created by the absorption of a laser pulse. The slow decay of the width shows that the lattice spacing recovers only after the electrons have recombined or diffused further than the extinction depth of the x-rays.

The reward for careful experimental setup and choice of detectors is summarized in Figure 5.8 where the centroid shift is measured with high confidence and high precision.

At low fluences (less than 0.5 mJ/cm^2), GaAs responds nearly identically to InSb. A large leftward peak shift begins the lattice reaction, cresting at 400 ps after excitation, with a quick recovery to a small, thermal offset. As the fluence is raised above 0.5 mJ/cm^2, however, the strain due to the impulsive acoustic wave is highly attenuated. At $\sim$ 400 ps, the lattice response saturates to increasing absorbed energy in the semiconductor. In spite of the nonlinear response to impulsive strain, the thermal

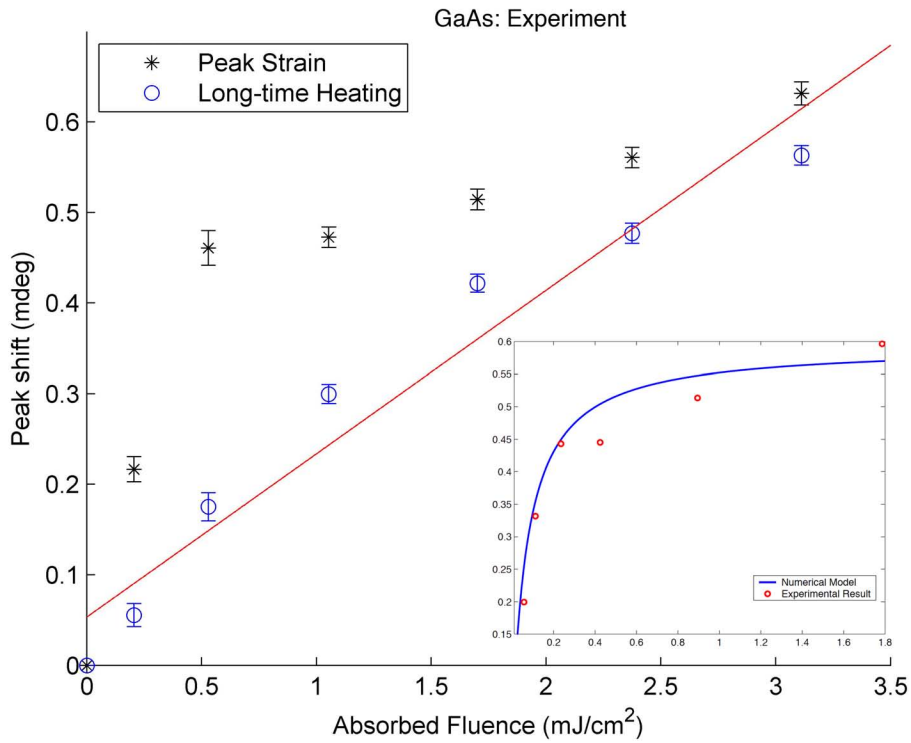

Figure 5.10: Thermal strain (blue) has a weak linear relationship with absorbed energy while the maximum peak shift (black) is nonlinear with laser fluence. A linear fit is performed on the data from the thermal regime with light agreement. Inset taken from [7] where the blue curve is a numerical model. It can be seen that the strain transition happens near the same fluence level in both cases.

regime continues to have a loosely linear response to fluence.

The rocking curve widths of GaAs in Figure 5.9 show a quick increase, qualitatively identical to that of InSb indicating that the lattice is thrown into a state of inhomogeneity. The recovery of the width, however, is quite different. Instead of recovering to within 15% of the original width, a gradient in the lattice spacing persists, taking nearly 1.5 ns to return to $\sim$ 15% where it took InSb a mere 200 ps for the highest fluence case. The additional time necessary to bring the lattice spacing into equilibrium is driven by hot electrons interacting with and diffusing into the crystal.

In Figure 5.10, the maximum Bragg peak deflection is shown to be nonlinear with

respect to absorbed fluence. The abrupt change in the trend of peak shift (near 0.5 mJ/cm^2) has been observed in previous time-resolved strain experiments with nearly this transition threshold (see inset) [7].

GaAs is also a saturable absorber where the penetration depth is a function of the laser intensity. A possible explanation for the high fluence cases is that excited electrons are generated deeper than 1 μm in the crystal. If carriers are located farther into the crystal, this would keep the lattice strained for a significant amount of time since the recombination rate is relatively small and the lifetime of electrons in the material is $\sim$ 1 ns.

5.4 Comparison with Models

Due to the majority of deposited energy being partitioned into thermal strain and the linear response in peak lattice distortion in InSb, the thermoelastic Thomsen model is an appropriate candidate. The Thomsen mode produces a linear peak strain (maximum distortion) and thermal strain ($>$ 2 ns after excitation) response in diffraction simulations. Despite an underestimation in the impulsive strain response, the model shows qualitative agreement with the results obtained experimentally for InSb. In Figure 5.11, the diffraction simulation shows the equivalent plot to Figure 5.6 for InSb, highlighting the linearity of the model. The ratio between the two slopes do not correspond quantitatively with the observed lattice motions, but the general trend is consistent with data and physical intuition.

The Thomsen model roughly underestimates the strength of the acoustic pulse by a factor of 1.5. This may be attributed to the omission of electron contributions in the impulsive wave. By changing the acoustic pulse amplitude — creating a constant thermal profile at the surface with a different amplitude than the traveling pulse —

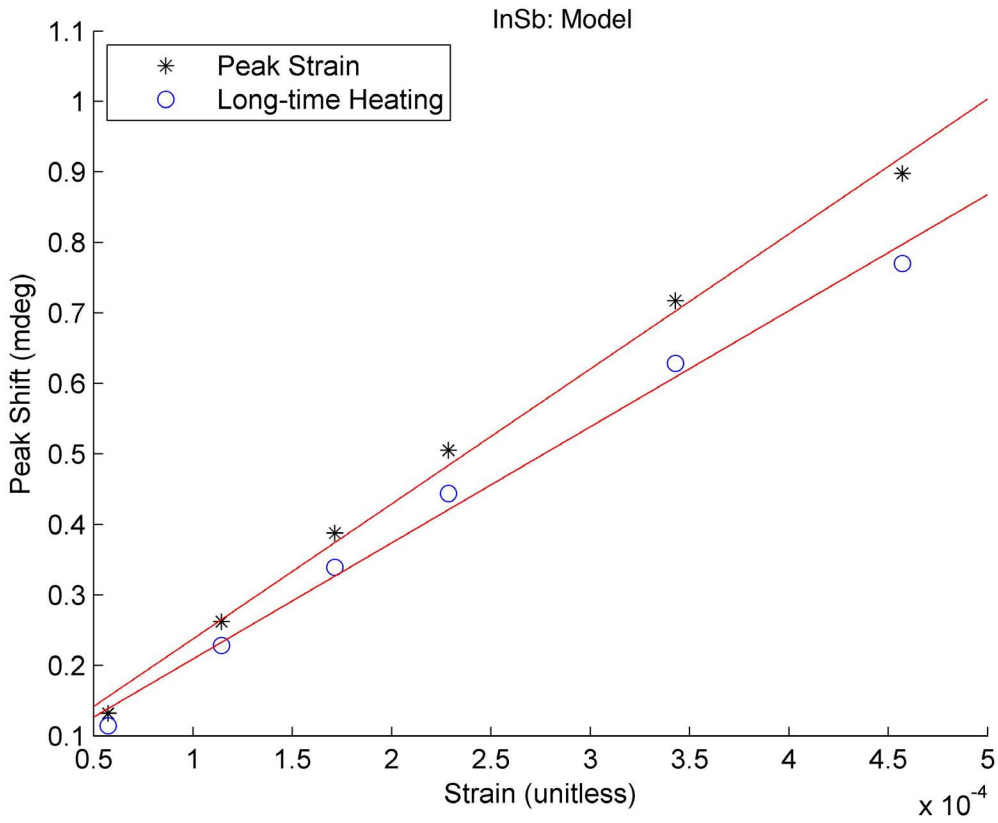

Figure 5.11: The Thomsen model shows peak strain and heating has a linear dependence with the amount of strain in the crystal. With InSb, the strain is directly related to the amount of absorbed energy. Although the ratio of the slopes contrast that of InSb data in Figure 5.6, the two are linear and represent the scalability of lattice response to absorbed energy.

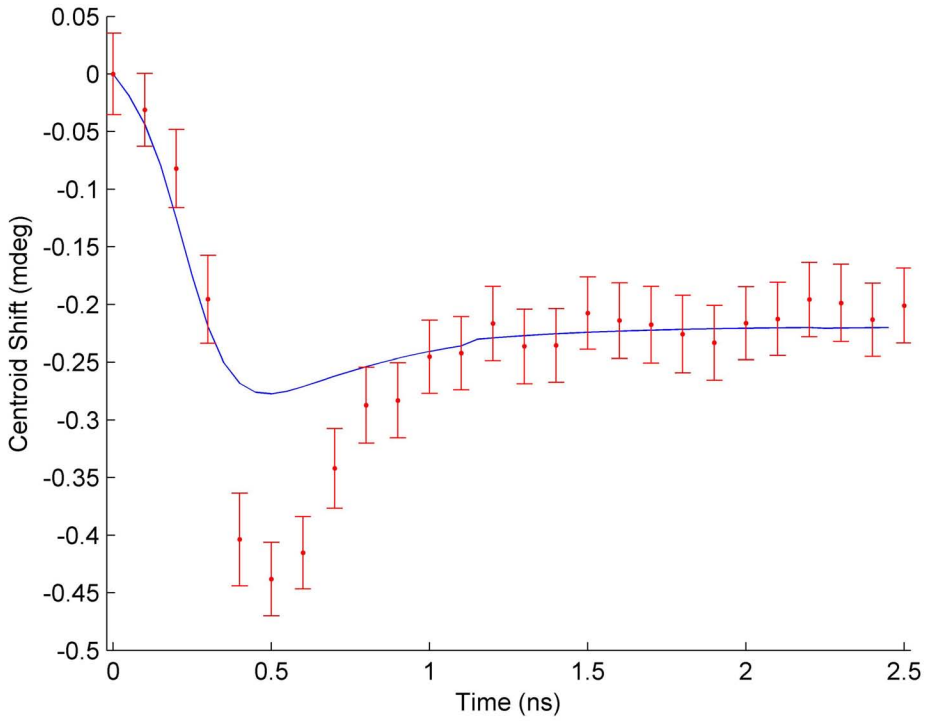

Figure 5.12: Thomsen model matched in the thermal regime to InSb data at 0.24 mJ/cm^2. The thermoelastic strain underestimates the contribution of non-thermal effects in the impulsive strain wave.

increases the peak strain response but fails to fully account for the magnitude of the impulsive component. Figure 5.12 shows the original, symmetric, Thomsen model with InSb data for the lowest fluence case. Since the Thomsen strain model is an analytic solution, numerical stability is not a problem. At high strain amplitudes, however, the leading edge of the bipolar strain is negative and results in a positive centroid shift. These high magnitudes of strain ($\sim 0.1\%$) lead to highly distorted and irregular diffraction patterns where a Gaussian approximation is no longer valid. For these cases, a center of mass analysis, is done to extract the center of the Bragg peak:

$$\text{Center of Mass} = \frac{\sum A_i \theta_i}{\sum A_i} \tag{5.4}$$

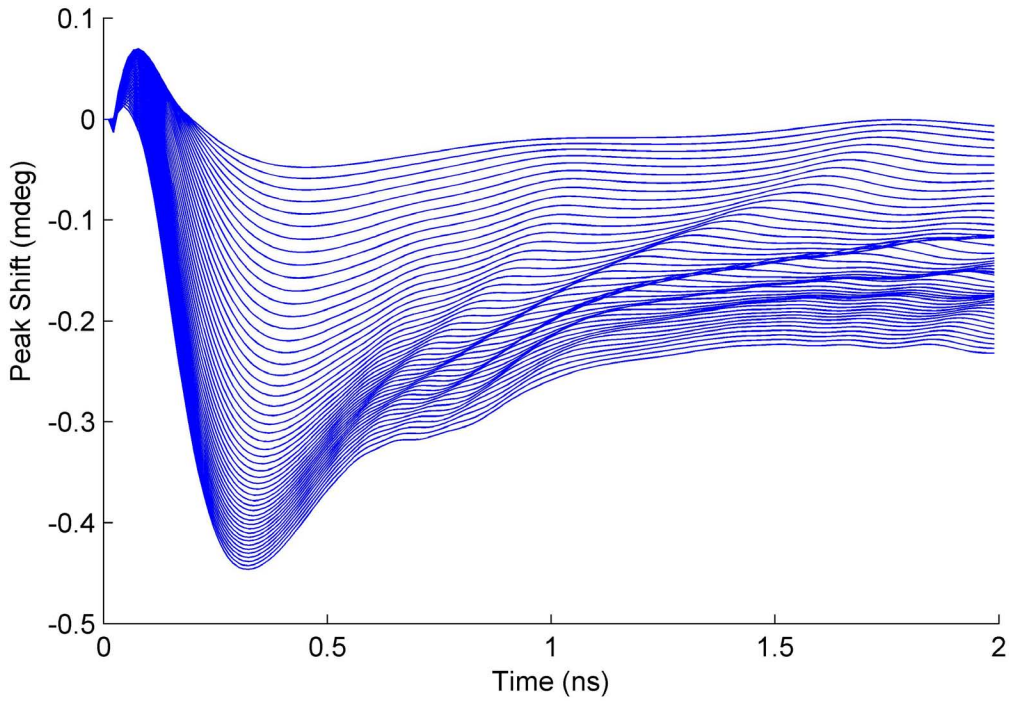

Figure 5.13: Time resolved centroid shifts calculated for GaAs with Auger recombination, electron diffusion, and thermal diffusion included shows a non-linear relation to fluence. Each plot is a even step size in fluence, and clearly shows the peak strain at a higher rate of saturation compared to the long-time condition. The ripple structure in the curves originate in the computation of the strain. To directly compare to data, the curves would be convoluted with a 100 ps gaussian, equivalent to the temporal resolution at the APS.

where A_i is the amplitude of the diffraction pattern in the ith column.

Qualitatively, the low fluence cases of GaAs are similar to that of any data set for InSb. Within the first nanosecond, the acoustic pulse disturbs the lattice producing a large shift in diffraction angle. Only thermal effects are detectable after the acoustic wave exists the x-ray extinction depth. The Thomsen model for GaAs, interestingly, appears to have similar characteristics to the high fluence data of Figure 5.8. This analysis, however, uses an inaccurate assumption that the highly energetic electrons in GaAs linearly couple with the lattice to produce strain. As shown in Equation 2.4,

the Auger recombination has a cubic dependence on the density and since the Auger recombination coefficient in GaAs is large, the resulting electron mean lifetime is $\sim$ 1 ns.

As such, a different model is necessary to handle these nonlinear features. To accomplish this, the electron and thermal diffusion equations,

$$\frac{\partial n}{\partial t} = D_e \frac{\partial^2 n}{\partial z^2} - An^3 \qquad \text{and} \qquad \frac{\partial T}{\partial t} = D_t \frac{\partial^2 T}{\partial z^2} - An^3 \frac{E_g}{C}, \tag{5.5}$$

must be solved for all time and space within the confines of the simulation. Finally, the strain is propagated through the crystal depth using a one-dimensional wave equation,

$$\frac{\partial^2 u}{\partial t^2} = v^2 \frac{\partial^2 u}{\partial z^2}. \tag{5.6}$$

Since this process involves taking the derivatives of several functions, the step size and initial parameterization is important. This method produces strain profiles with similar characteristics to a driven traveling wave and produces centroid diffraction shifts better resembling data seen in InSb or the low fluence cases of GaAs. These simulations involve a nonlinear dependence on fluence where the lattice response begins to saturate at higher absorbed energies (see Figure 5.13). The nonlinearities, without the addition of a free parameter in the penetration depth, are naturally incorporated in this model. A plot of the largest lattice deflection and amount of strain, $\Delta d/d$, is given in Figure 5.14 which shows the nonlinear relation to strain and the approximately linear strain in the thermal region ($>$ 2 ns). The transition into a nonlinear regime occurs around 0.4 mdeg, near where the GaAs data begins to behave nonlinearly. This imparts confidence into the theory behind this strain profile that

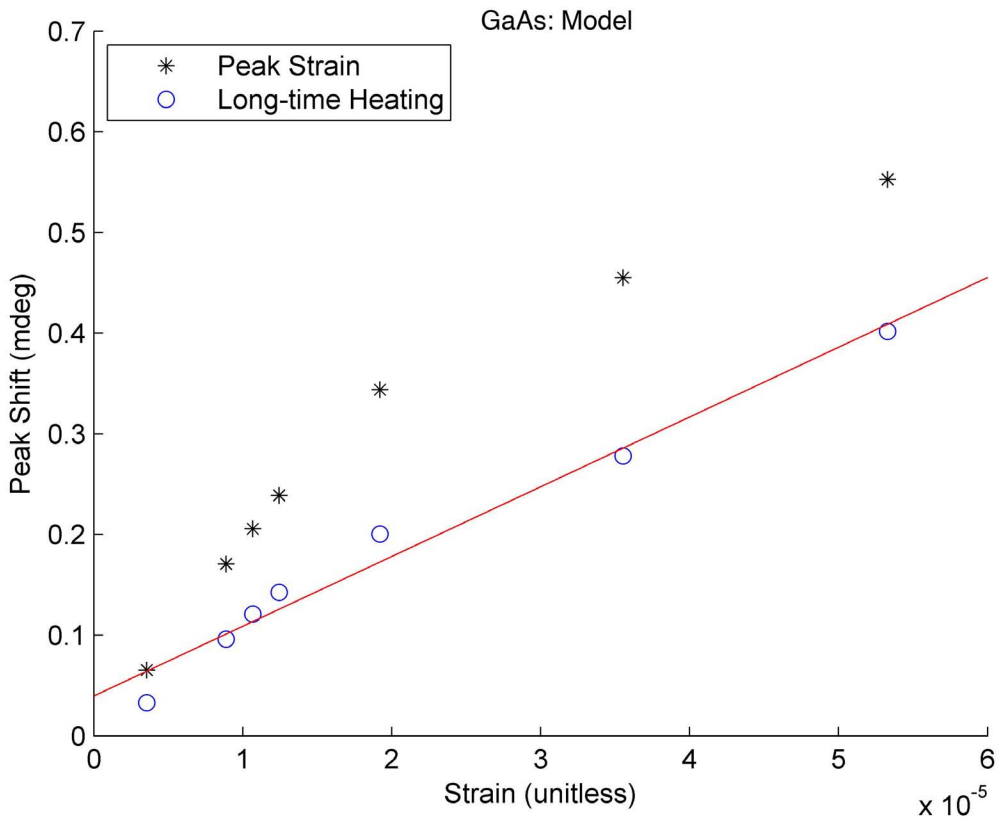

Figure 5.14: A nonlinear strain model shows that centroid shift due to heating has a rough linear dependence while the peak strain behaves nonlinear, even at low strain amplitudes. The trend of this simulation is similar to the data collected for GaAs and shown in Figure 5.10.

Auger recombination and electron diffusion must be contributing to the nonlinear response.

CHAPTER VI

Conclusions and Outlook

This thesis presents a study of strain and lattice dynamics in photo-excited InSb and GaAs. The techniques used to produce the high quality data can be extended to any time resolved diffraction experiment from any strong reflection. Additionally, a computer program was developed to calculate high resolution, benchmarked Bragg diffraction peaks for a strained crystal.

The diffraction data for InSb has a linear dependence on absorbed laser fluence. This is due to a partitioning of energy such that the majority transfers into the lattice as heat within the time resolution of these experiments. As the crystal heats, the lattice responds with linear expansion and generates a traveling acoustic impulsive wave. Future work will seeks to achieve quantitative agreement between measured and modeled strain. We also anticipate that the next generation of x-ray sources with better temporal resolution may be able to capture transient nonlinearities in InSb.

For GaAs, a linear response to absorbed fluence was observed at long times following laser excitation, however, while the impulsive strain remained within the probe depth of the x-rays, the response is nonlinear. This can have several explanations. Our model shows qualitatively that strain saturation and recovery may be explained by a coupled charge and temperature distribution which is continuing to evolve at

the time and length scales accessible by this experiment. Other alternative explanations may also be tested against the high-quality time-resolved diffraction data and strain analysis code developed for this thesis. Such nonlinear strain generation processes may include free carrier absorption, carrier-carrier scattering, and saturable absorption.

In conclusion, this thesis has shown for the first time that the approach to thermal equilibrium in a laser-excited semiconductor does not necessarily follow a linear stress-strain relationship at short timescales, even far away from phase transitions. This opens up the possibility of real-time manipulations of non-equilibrium states in these systems and motivates a more nuanced understanding of this common and important process.

APPENDICES

APPENDIX A

Physical Properties of GaAs and InSb

Symbol	Parameter	GaAs	InSb	Unit
θ_B	Bragg Angle [400], 10 keV	23.18	28.89	deg
R	Reflectivity	0.039	0.144	Unitless
β	Linear Expansion	5.73×10^{-6}	5.37×10^{-6}	1/K
A	Laser Spot Size	38.30	27.82	mm^2
n	Index of Refraction	$3.644 + i0.089$	$4.4 + i0.637$	Unitless
ζ, d	Absorption Length	1	0.1	μm
C	Heat Capacity	1.096×10^7	7.203×10^6	eV/K/μm^3
ν	Poisson's Ratio	0.31	0.35	Unitless
v	Sound Speed	4.73	3.4	μm/ns
ρ	Density	5.32×10^3	5.77×10^3	kg/m^3
B	Bulk Modulus (100)	75.3×10^9	40.9×10^9	Pa
E_g	Band Gap	1.424	0.17	eV
α_t	Thermal Expansion	5.73×10^{-6}	5.37×10^{-6}	1/K
α_e	Electronic Strain Coupling	2.019×10^{-11}	2.195×10^{-11}	μm^3
D_t	Temperature Diffusion	0.031	0.016	μm^2/ns
D_e	Electron Diffusion	10	200	μm^2/ns
A	Auger Recombination	1×10^{-15}	5×10^{-11}	μm^6/ns

Table A.1: Properties of GaAs and InSb at 300 K. Needed for calculations of Thomsen *et al.* and Decamp *et al.* strain models.

APPENDIX B

Ztec Oscilloscope Boot Protocol

Instructions for operating the Ztec Oscilloscope ZT4212 at 7IC-C.

Compiled by Eric Landahl, Dohn Arms, and Jackson Williams

For acquiring APD waveforms in proportional mode, the following should be noted:

APD output into Channel 1.
APD control voltage: 7.75 V.
APD high voltage: 210 V.
Detector is linear up to 100 mV.
Linearity can be corrected up to $\sim$ 150 mV.
Laser trigger (Pockel's cell signal) to External Trigger.
An external delay box is helpful for moving this trigger to the correct bunch.
User Array Calcs need to be set up properly:
$\rightarrow$ Array Variables: ztec:Inp1ScaledWave NPP NMS, Calculation: -aa[00,500] -amin(nsmoo(-aa[95,120],5)).
ScanH needs to be set up properly:
$\rightarrow$ DetTriggers: ztec:OpInitiate, Detectors: ztec:Inp1ScaledWave, Settling: 1.5 s.

For the initial boot running from bantu (use current IP address):

```
export EPICS_CA_ADDR_LIST = 164.54.107.56
```

Check if oscilloscope is communicating:

```
caget ztec:UtilID
```

Operational setup for acquiring APD waveforms in proportional mode:

```
caput ztec:Inp1Wave.SCAN 7
caput ztec:Inp1ScaledWave.SCAN 7
caput ztec:Inp1ScaledTime.SCAN 7
caput ztec:setInp1Enable 1
caput ztec:setInp1Imped 50
caput ztec:setInp1Couple DC
caput ztec:setInp1Range 0.25
caput ztec:setTrigSource EXT
caput ztec:setTrigLevExt -0.5
caput ztec:setTrigSlope NEG
caput ztec:setTrigImpedExt 50
caput ztec:setTrigMode NORM
caput ztec:setTrigType EDGE
caput ztec:setAcqType AVER
caput ztec:setAcqCount 1024
caput ztec:setHorzOffset 0
caput ztec:setHorzTime 1e-6
caput ztec:setHorzPoints 512
```

APPENDIX C

Matlab Code

C.1 Strained Crystal Dynamical Diffraction Routines

C.1.1 Main Routine for Dynamical Diffraction

```
%% Main Routine for Dynamical Diffraction Simulation
% X_top.m
% Written by G.J. Williams
% Last Updated 6/7/2010
clear all; tic
%Choose initial parameters:
crystal = 1;                        % GaAs = 1, InSb = 2, Ge = 3
E = 10000;                          % Energy currently fixed at 10 keV
reflect = [4 0 0];                  % Reflection fixed at [4 0 0]
T = 300;                            % Temperature (K)

% Find Atomic Form Factors, lattice parameters, reflection parameters:
[F_0,F_hkl,a,lambda,thetaB] = formf(reflect,crystal,E,T);
% Calculate psi_0 and psi_H (complex crystal susceptibilities):
[psi_0,psi_H] = X0H(F_0,F_hkl,a,lambda);

t_f = .5;                           % final time (must be in ns)
E_p = 1.55;                         % photon energy in eV
F = 4.5e-2;                         % Fluence in mJ/cm^2
fluence = F*6.242*10^7/E_p;         % Fluence in photons/micron^2

[s,x,t] = FStrain(crystal,fluence,t_f);     % Strain calculation

```

```
centshift = zeros(length(t),1);      % Prealocate space for centshift
for n = 1:length(t);                 % Time interation loop

    % Run the dynamical diffraction code for each time point
    [cent,dtheta] = Wie(psi_0,psi_H,thetaB,lambda,s(:,n),x);
    if(n == 1);          % Reference point to measure change in centroid
        cent0 = cent;                % Initial (t = 0) centroid position
    end
    centshift(n) = cent - cent0;     % Calculate centroid shift
end
A1 = smooth(t,centshift);            % Smoothing Function (running average)
if(crystal == 1);                    % Load Data for comparison
    zzz = load('GaAs_all.txt');      % GaAs Data
elseif(crystal == 2);
    zzz = load('InSb_all.txt');      % InSb Data
end

figure(6); clf; hold on
plot(t,A1,'b');
plot(t,centshift,'g');
errorbar(zzz(:,1),zzz(:,2),zzz(:,3),'k.');
errorbar(zzz(:,1),zzz(:,4),zzz(:,5),'b.');
errorbar(zzz(:,1),zzz(:,6),zzz(:,7),'r.');
errorbar(zzz(:,1),zzz(:,8),zzz(:,9),'c.');
errorbar(zzz(:,1),zzz(:,10),zzz(:,11),'g.');
xlabel('Time (ns)');
ylabel('Centroid Shift (mdeg)');

t3 = toc;
```

C.1.2 Structure Factor

```
%% Subroutine for dynamical diffraction simulation
% Calculates atomic form factors
% Written by G.J. Williams
% Last Updated 6/7/2010
function [F_0,F_hkl,a,lambda,thetaB] = formf(reflect,crystal,E,T)
warning off all;

% Choose which crystal to use, load form factor data and lattice parameter
if(crystal == 1);
    aa = load('Ga.txt');    bb = load('As.txt');    a = 5.65325;
elseif(crystal == 2);
    aa = load('In.txt');    bb = load('Sb.txt');    a = 6.4789;
elseif(crystal == 3);
    aa = load('Ge.txt.');   bb = 0;                 a = 5.64613;
elseif(crystal == 4);
    aa = load('Zn.txt');    bb = load('S.txt');     a = 5.420;
```

```
elseif(crystal == 5);
    aa = load('C.txt.');    bb = 0;                 a = 3.56683;
elseif(crystal == 6);
    aa = load('Si.txt');    bb = 0;                 a = 5.43095;
else
    fprintf('Warning: No Form Factor Could Be Calculated \n');
end

% Constants:
i = sqrt(-1);
planck = 4.13566733e-15;     % in ev*s
c = 299792458e10;            % in Angs/s
% Bragg's law calculations:
h = reflect(1); k = reflect(2); l = reflect(3);
d = a/sqrt(h^2 + k^2 + l^2);
Q = 2*pi/d;
lambda = planck*c/E;
theta2 = asin(lambda/(2*d))*2 * 180/pi;     % In degrees
thetaB = theta2/2 * pi/180;                 % In radians

% Load data for f' and f'' correction terms
fpp_data = aa(1:length(aa),3);
fp_data = aa(1:length(aa),2);
E1_data = aa(1:length(aa),1);
% Interpolate data at every 1 eV delineation
E1 = (min(E1_data):1:max(E1_data));
fpZ = interp1(E1_data,fp_data,E1);
fpp = interp1(E1_data,fpp_data,E1);
% Making sure the energy corresponds to the correct interpolated element
fp_aa = fpZ(E - min(E1) + 1);
fpp_aa = fpp(E - min(E1) + 1);

%% Finding f0.  Cromer-Mann coefficients taken from ruppweb, differs
% slightly from Cromer, DT and Mann, JB (Acta. Cryst. A., 1968)
% (http://www.ruppweb.org/new_comp/scattering_factors.htm)
    if(crystal == 1)    %Ga
        a1 = 15.235; a2 = 6.701; a3 = 4.359; a4 = 2.962;
        b1 = 3.067;  b2 = 0.241; b3 = 10.781;b4 = 61.414;
        c  = 1.719;
    elseif(crystal == 2) % In
        a1 = 19.162; a2 = 18.560; a3 = 4.295; a4 = 2.040;
        b1 = 0.548;  b2 = 6.378; b3 = 25.850; b4 = 92.803;
        c  = 4.939;
    elseif(crystal == 3) %Ge
        a1  = 16.082;   a2= 6.375;  a3= 3.707;  a4  = 3.683;
        b1  = 2.851;    b2= 0.252;  b3= 11.447; b4= 54.763;
        c   = 2.131;
    elseif(crystal == 4)  %Zn
        a1  = 14.074;   a2= 7.032; a3= 5.165;   a4= 2.410;
        b1  = 3.266;    b2= 0.233;  b3= 10.316; b4  = 58.710;
        c   = 1.304;
    elseif(crystal == 5) % C
        a1  = 2.310;    a2=1.020;   a3= 1.589;  a4 =0.865;
        b1  = 20.844;   b2= 10.208; b3= 0.569;  b4= 51.651;
```

```
        c   = 0.216;
    elseif(crystal == 6)  % Si
        a1 = 6.292; a2 = 3.035;  a3= 1.989;  a4=1.541;
        b1 = 2.439; b2 = 32.334; b3=0.678;  b4= 81.694;
        c =  1.141;
    else
        a1 = 0; a2 = 0; a3 = 0; a4 = 0;
        b1 = 0; b2 = 0; b3 = 0; b4 = 0;
        c  = 0;
    end
%Assimilate into: f0 = sum a_i*exp(b_i*(Q/4*pi)^2) + c:
f0_aa = c + a1*exp(-b1*(Q/(4*pi))^2) + a2*exp(-b2*(Q/(4*pi))^2)
+ a3*exp(-b3*(Q/(4*pi))^2) + a4*exp(-b4*(Q/(4*pi))^2);
% Finding incident form factor:
f0_aa0 = c + a1 + a2 + a3 + a4;

% Data for the second atom in the crystal:
if(bb == 0);
    f0_bb = f0_aa; fp_bb = fp_aa; f0_bb0 = f0_aa0; fpp_bb = fpp_aa;
elseif(bb ≠0);
    % Load data
    fpp_data = bb(1:length(bb),3);
    fp_data = bb(1:length(bb),2);
    E1_data = bb(1:length(bb),1);
    % Interpolate data
    E1 = (min(E1_data):1:max(E1_data));
    fpZ = interp1(E1_data,fp_data,E1);
    fpp = interp1(E1_data,fpp_data,E1);
    fp_bb = fpZ(E - min(E1) + 1);
    fpp_bb = fpp(E - min(E1) + 1);
    if(crystal == 1)
        a1 = 16.672; a2 = 6.070; a3 = 3.431; a4 = 4.278;
        b1 = 2.635;  b2 = 0.265; b3 = 12.948;b4 = 47.797;
        c  = 2.531;
    elseif(crystal == 2)
        a1 = 19.642; a2 = 19.045; a3 = 5.037;  a4 = 2.683;
        b1 = 5.303;  b2 = 0.461;  b3 = 27.907; b4 = 75.283;
        c  = 4.591;
    elseif(crystal == 4)
        a1 = 6.905; a2= 5.203;  a3= 1.438;  a4= 1.586;
        b1  = 1.468;    b2= 22.215; b3= 0.254;  b4= 56.172;
        c   = 0.867;
    else
        % keep all a_i,b_i,c constants the same
    end
% f0 = sum(a_i * exp(-b_i * Q^2)) + c
f0_bb = c + a1*exp(-b1*(Q/(4*pi))^2) + a2*exp(-b2*(Q/(4*pi))^2) ...
+ a3*exp(-b3*(Q/(4*pi))^2) + a4*exp(-b4*(Q/(4*pi))^2);
% Incident scattering power
f0_bb0 = c + a1 + a2 + a3 + a4;
end
%% Compiling the Atomic Form Factors
% Debye-Waller Factor [M_in M_sb] = debye(crystal,temperature)
[u2_aa u2_bb] = debye(2,T);
```

```
M_aa = 8*pi^2/3*(sin(thetaB)/lambda)^2*(u2_aa); %
M_bb = 8*pi^2/3*(sin(thetaB)/lambda)^2*(u2_bb); %
% Atomic form factor:
f_aa = (f0_aa + fp_aa + i*fpp_aa)*exp(-M_aa);
f_bb = (f0_bb + fp_bb + i*fpp_bb)*exp(-M_bb);
% Atomic form factor for reflection [0 0 0], needed for F_0
f_aa0 = f0_aa0 + fp_aa + i*fpp_aa;   %  -- these also seem reasonable
f_bb0 = f0_bb0 + fp_bb + i*fpp_bb;
% Full structure factor for the InSb crystal.
F_0 = 4*(f_aa0 + f_bb0);
F_hkl = f_aa*(1 + exp(pi*i*(h+k))+exp(pi*i*(h+l))+exp(pi*i*(k+l))) ...
+f_bb*(exp(.5*pi*i*(h+k+l))+exp(.5*pi*i*(3*h+3*k+l)) ...
+exp(.5*pi*i*(3*h+k+3*l))+exp(.5*pi*i*(h+3*k+3*l)));
end
```

C.1.3 Calculating the Debye-Waller Coefficient

```
%% Subroutine for dynamical diffraction simulation
% debye.m
% Calculates Debye-Waller factors
% Written by G.J. Williams
% Last Updated 6/7/2010

function [M1,M2] = debye(crystal,T)

temp = [0.001 100 200 400 600 800 1000];
temperature = 1:1:1000;

if(crystal == 1);       %GaAs
    e1 = [1.858e-3 3.397e-3 6.038e-3 0.011658 0.017368 0.023101 0.028844];
    e2 = [1.632e-3 2.949e-3 5.201e-3 0.010014 0.014909 0.019827 0.024754];
elseif(crystal == 2);   %InSb
    e1 = [1.958e-3 6.102e-3 0.011711 0.023163 0.034671 0.046194 0.057723];
    e2 = [1.724e-3 5.274e-3 0.010085 0.019926 0.029821 0.039728 0.049642];
elseif(crystal == 3);   %Ge - both atoms in the structure are the same
    e1 = [2.471e-3 3.196e-3 4.865e-3 8.772e-3 0.01287 0.017022 0.021198];
    e2 = [2.471e-3 3.196e-3 4.865e-3 8.772e-3 0.01287 0.017022 0.021198];
elseif(crystal == 4);   %ZnS
    e1 = [2.229e-3 3.942e-3 7.046e-3 0.013641 0.020335 0.027053 0.033781];
    e2 = [2.425e-3 3.504e-3 5.565e-3 0.010258 0.015132 0.020054 0.024997];
elseif(crystal == 5);   % C
    e1 = [1.611e-3 1.626e-3 1.690e-3 1.986e-3 2.436e-3 2.962e-3 3.529e-3];
    e2 = [1.611e-3 1.626e-3 1.690e-3 1.986e-3 2.436e-3 2.962e-3 3.529e-3];
elseif(crystal == 6);   % Si
    e1 = [1.718e-3 3.191e-3 5.665e-3 0.01093 0.01628 0.021653 0.027035];
    e2 = [1.718e-3 3.191e-3 5.665e-3 0.01093 0.01628 0.021653 0.027035];
else
    fprintf('Warning: Debye Waller Factor could not be calculated \n');
```

```
    e1 = [0 0 0 0 0 0 0];
    e2 = [0 0 0 0 0 0 0];
end
debye1 = interp1(temp,e1,temperature);
debye2 = interp1(temp,e2,temperature);

M1 = debye1(T);
M2 = debye2(T);
end
```

C.1.4 Determining $\psi_{0,H}$

```
%% Subroutine for dynamical diffraction simulation
% X0H.m
% Calculates susceptibilities
% Written by G.J. Williams
% Last Updated 6/7/2010
function [psi_0,psi_H] = X0H(F_0,F_hkl,a,lambda)
a = a*10^-10;                    % in meters
V = a^3;                         % Volume in m^3
e = 1.60217733*10^-19;           % in C
m = 9.1093897*10^-31;            % in kg
c = 299792458;                   % in m/s
e0 = 8.854187817*10^-12;         % F/m
lambda = lambda*10^-10;          % in meters
F_0H = F_0;                      % Undamaged structure factor
F_H = F_hkl;                     % Debye factor already taken care of.
% Structure parameter of incident wave
psi_0 = -(e^2/(m*c^2))*(lambda^2/pi)*(F_0H/V)/(4*pi*e0);
% Structure parameter of diffracted wave
psi_H = -(e^2/(m*c^2))*(lambda^2/pi)*(F_H/V)/(4*pi*e0);
end
```

C.1.5 Takagi-Taupin Rocking Curves

```
%% Subroutine for dynamical diffraction simulation
% Wie.m
% Calcualtes strained crystal diffraction peaks
% Written by G.J. Williams
% Last Updated 6/7/2010
% Everything in this program should be in SI units
function [cent,dtheta] = Wie(psi_0,psi_H,thetaB,lambda,s,x)

```

```
strain = flipud(s);
lambda = lambda*10^-10;

psi_0r = real(psi_0);       psi_0i = imag(psi_0);
psi_Hr = real(psi_H);       psi_Hi = imag(psi_H);

angstep = 10^-6;            % Angular steps (keep fixed at 1 urad)
nmax = 300;                 % 300 angular steps
A00 = max(x)*10^-6;         % Size of crystal (depth) (
jmax = length(x);           % 2000 depth steps
dstep = A00/(jmax - 1);     % step size is 2.5 nm

pXtop = zeros(1,nmax); ptheta = zeros(1,nmax);     % Prealocating Space

for n = 1:nmax          % Angluar loop
    % Calculate angluar range
    theta = thetaB - 0.4*nmax*angstep + n*angstep ;
    % Ratio of the deffracted/incident cosines
    b = 1;   % For symmetric Bragg reflections, b = 1
    % Incident absorbtion parameter
    g = ((1+b)*psi_0i)/(2*abs(psi_Hr)*sqrt(b));
    % Diffracted absorption parameter
    k = psi_Hi/psi_Hr;
    % Difrection of cosines
    gamma_0 = cos(pi/2 - thetaB);
    gamma_H = cos(pi/2 - thetaB);

    for j = 1:jmax      % Depth loop
        z = (A00 - (j)*dstep);      % Iterating through the crystal depth

        e1 = strain(j);             % Import strain depth position
        % For the first step, A01 is the infinite crystal solution
        A01 = (A00)*(pi*abs(psi_Hr))/(lambda*sqrt(gamma_H*gamma_0));
        % Normalizing iterative crystal depth
        A = (pi*z*abs(psi_Hr))/(lambda*sqrt(gamma_H*gamma_0));
        % Strain coefficient
        c1 = 2*sin(2*thetaB)*tan(thetaB);

        % Angle between the surface and reflecting plane is zero, c2 = 0
        c2 = 0;
        e2 = 0;                     % e2 set to 0 for consistency.
        % Angle of reflection (independent variable)
        alpha = -2*(theta - thetaB)*sin(2*thetaB) - (c1*e1 + c2*e2);
        % Deviation from Bragg angle
        y = ((1+b)*psi_0r - b*alpha)/(2*abs(psi_Hr)*sqrt(b));

        % Taking the square root of a complex number
        r1 = abs(y^2 - g^2 + k^2 - 1);          % APPENDIX FROM WIE et al.
        r2 = 2*(y*g - k);
        r  = sqrt(r1^2 + r2^2);
        s1 = sqrt((r+r1)/2);
        s2 = sqrt((r-r1)/2);
        q1 = sqrt(1 - k^2 + g^2);
        q2 = k/g;
```

```
        i = sqrt(-1);
        if(y ≤ - q1)
            s = s1 + i*s2;
        elseif(y ≤ q2) && (y ≥ -q1)
            s = s2 + i*s1;
        elseif(y ≤ q1) && (y ≥ q2)
            s = -s2 + i*s1;
        elseif(y ≥ q1);
            s = -s1 + i*s2;
        else
            fprintf('Error found in taking the square root');
        end
        i = sqrt(-1);
        B = -(1+i*k);
        C = y + i*g;
        X0 = -B/(C - s);                    % Zero-strain solution

        if(j == 1)
            Xj = X0;                 % Start with zero strain solution
            A0 = A01;                % Start with infinite depth
        end

        % Diffraction solution
 Xj = (s*Xj + i*(B+C*Xj)*tan(s*(A - A0)))/(s - i*(C+B*Xj)*tan(s*(A - A0)));
        A0 = A;                      % Update A0 as the previous A value
    end

    pXtop(n) = Xj;                        % Top layer soln vs theta
    ptheta(n) = theta;                    % Theta for plotting

end
amp = conj(pXtop).*pXtop;           % Total reflecting intensity
dtheta = (ptheta - thetaB)*180/pi*1000;       % In mdeg

% Angular Convolution
width = 2.5;           % Double Crystal curve FWHM of Diamond (111) in mdeg
c = width*1/(2*sqrt(2*log(2)));     % Convert from FWHM to "tau"
a = dtheta;                         % Independent variable

b1 = 0;
G = exp(-((a-b1)).^2/(2*c^2));      % Angular Gaussian to convolude
convamp = conv2(amp,G,'same');      % Convolution function
% Normalization value (same size as amp)
convamp = max(amp)/max(convamp)*convamp;

f = fittype('gauss1');                % Fitting a single gaussian to peak
ffit = fit(dtheta',convamp',f);
params = coeffvalues(ffit);           % Extracting fit parameters
cent = params(2);                     % Extraction centroid positon
end
```

C.1.6 Thomsen Strain Model for GaAs

```
%% strain.m
% Written by G. Jackson Williams 6/7/2010
% strainInSb.m creates the Thomsen strain for GaAs

function [strain] = strainGaAs(z,t,thetaB)
lambda = 800*10^-9;          % Center wavelength of laser (m)

% These numbers are for GaAs ONLY
H = 3.1894;                  % Width of beam (mm)
V = 4.7264/sin(thetaB);      % Height of beam (mm) (adjusted for the angle)
A = H*V*10^-6;               % Area of beam spot (m^2)

RepRate = 1000;              % Repetition Rate of the Laser (Hz)
P = 0.39;                    % Power (Watts)
Q = P/RepRate;               % Energy of the pulse (J)

C = 1.739*10^6;              % Heat Capacity (J/m^3-K)
nu = 0.31;                  % Poison's Ratio (unitless)
Y = 75.3*10^9;               % Youngs Modulus in (100) direction(Pa)
rho = 5.317*10^3;            % Denisity (kg/m^3)
beta = 5.73*10^-6;           % Coefficient of Thermal Expansion (1/K)

P = 1;                       % Light is P polarization
S = 0;

n1 = 1;                      % Index of refaction of air
n = 3.664;                   % Index of Refraction n(Real) for GaAs
k = 0.089;                   % n(Imag) for GaAs
n2 = n + i*k;                % Complex index of refraction for GaAs

% Finding the reflectation coefficient of light for GaAs
theta = (pi/2 - thetaB);
theta2 = asin(n1*sin(theta)/n2);
r_p = (-n2*cos(theta) + n1*cos(theta2))/(n2*cos(theta) + n1*cos(theta2));
r_s = -(n1*cos(theta) - n2*cos(theta2))/(n1*cos(theta) + n2*cos(theta2));

R_p = conj(r_p)*r_p;
R_s = conj(r_s)*r_s;
R = S*R_s + P*R_p;           % Reflectivity coefficient of light

alpha = k*pi*4/lambda;       % absorbtion coefficient
zeta = 1/alpha;              % Penetration depth (700 nm)

v = sqrt(3*(1-nu)/(1+nu)*Y/rho);      % Speed of Sound (100) (m/s)

strain = (1-R).*Q.*beta./(A.*zeta.*C).*(1+eta)./(1-eta).*(exp(-z./zeta)...
.*(1-0.5.*exp(-v.*t./zeta))-0.5.*exp(-abs(z-v.*t)./zeta).*(sign(z-v.*t)));
end
```

C.1.7 Thomsen Strain Model for InSb

```
%% strainInSb.m
% Written by G. Jackson Williams 6/7/2010
% strainInSb.m creates the Thomsen strain for InSb

function [strain] = strainInSb(z,t,thetaB)
lambda = 800*10^-9;          % Center wavelength of laser (m)

% These numbers are for InSb ONLY
H = 4.2105;                  % Width of beam (mm)
V = 3.1924/sin(thetaB);      % Height of beam (mm) (adjusted for the angle)
A = H*V*10^-6;               % Area of beam spot (m^2)

RepRate = 5000;              % Repetition Rate of the Laser (Hz)
P = 0.39;                    % Power (Watts)
Q = P/RepRate;               % Energy of the pulse (J)

C = 1.154*10^5;              % Specific Heat (J/m^3-K)
nu = 0.35;                   % Poison's Ratio (unitless)
Y = 40.9*10^9;               % Youngs Modulus for the (100) direction (Pa)
rho = 5.77*10^3;             % Denisity (kg/m^3)
beta = 5.37*10^-6;           % Coefficient of Thermal Expansion (1/K)

P = 1;                       % Light is P polarization
S = 0;

n1 = 1;                      % Index of refaction of air
n = 4.4;                     % Index of Refraction n(Real) for InSb
k = 0.63662;                 % n(Imag) for InSb
n2 = n + i*k;                % Complex index of refraction for InSb

% Finding the reflectation coefficient of light for InSb
theta = (pi/2 - thetaB);
theta2 = asin(n1*sin(theta)/n2);
r_p = (-n2*cos(theta) + n1*cos(theta2))/(n2*cos(theta) + n1*cos(theta2));
r_s = -(n1*cos(theta) - n2*cos(theta2))/(n1*cos(theta) + n2*cos(theta2));

R_p = conj(r_p)*r_p;
R_s = conj(r_s)*r_s;
R = S*R_s + P*R_p;           % Reflectivity coefficient of light

alpha = k*pi*4/lambda;       % absorbtion coefficient
zeta = 1/alpha;              % Penetration depth (100 nm)

v = sqrt(3*(1-nu)/(1+nu)*Y/rho);   % speed of sound in the (100) direction

strain = (1-R).*Q.*beta./(A.*zeta.*C).*(1+eta)./(1-eta).*(exp(-z./zeta)...
.*(1-0.5.*exp(-v.*t./zeta))-0.5.*exp(-abs(z-v.*t)./zeta).*(sign(z-v.*t)));
end
```

C.1.8 Asymmetric Thermoelastic Model for InSb

```
%% strainInSb1.m
% Written by G. Jackson Williams 6/7/2010
% Asymmetric Thomsen model strain using Auger and deformation potential

function [strain] = strainInSb1(z,t)
% z has units of meters, t has units of s, v has units of m/s
% Everything else is um, ns, eV, K
% Returns a matrix of strain elements for a particular time point.

fluence = 9e6;          % Fluence             (photons/um^2)

E_p = 1.55;             % Photon energy       (eV)
E_g = 0.17;             % Bandgap             (eV)
C = 7.203*10^6;         % Specific Heat       (ev/K/um^3)
d = 0.1;                % Pentration Depth    (um)
d1 = d*10^-6;           % Pentration Depth    (m)
v = 3.4*10^3;           % Speed of Sound      (m/s)
alpha_e = 2.195*10^-11; % electronic coupling (um^3)
alpha_t = 5.37*10^-6;   % Thermal expansion   (1/K)

strain = alpha_t.*(E_p-E_g).*fluence./C./d.*exp(-z./d1) - ...
alpha_e.*fluence./d.*(1/2.*exp((-z-v.*t)./d1) + ...
1/2.*exp(-abs(z-v.*t)/d1).*sign(z-v.*t));
end
```

C.2 Data Reduction and Analysis

C.2.1 Main Routine for GaAs Data Extraction

```
%% Angshift_GaAs.m
% Written by G. Jackson Williams 9/1/2009
% Top routine to analyze a 2-D diffraction scan.

clear all;
format short g;
hmax = 6;           % Number of waveplate points in the scan
tic                 % Start the timer for the program

for h = 1:hmax      % For each waveplate scan, do a centroid analysis

    [Dth,time,Etot,n,m] = chomplite_GaAs(h);
    if(h == 1);                 % 0.211 W
        Dth1(1:n) = Dth;
        E1(1:n) = Etot/2;
        time1(1:n) = time;
    elseif(h == 2);             % 1.24 W
        Dth2(1:n) = Dth;
        E2(1:n) = Etot/2;
    elseif(h == 3);             % 0.678 W
        Dth3(1:n) = Dth;
        E3(1:n) = Etot/2;
    elseif(h == 4);             % 0.964 W
        Dth4(1:n) = Dth;
        E4(1:n) = Etot/2;
    elseif(h == 5);             % 0.082 W
        Dth5(1:n) = Dth;
        E5(1:n) = Etot/2;
    else                        % 0.420 W
%---Experimental Problems occured on this run.  Do not use in Analysis---
        Dth6(1:n) = Dth;
        E6(1:n) = Etot/2;
    end
end

% Calculating the peak shift and residual heating of the crystal
% power   = laser power meter readings (in W)
% strain  = maximum centroid shift (in mdeg)
% heat    = averaged data from 1.5 ns to the end of the data run
% Estrain = error associated with the strain measurment at particular time
% Eheat   = error associated with heat measurement
power = [0;0.082;0.211;0.42;0.678;0.946;1.24];
strain = -1*[0;min(Dth5);min(Dth1);min(Dth6);min(Dth3);min(Dth4);min(Dth2)];
heat = -1*[0;mean(Dth5(15:n));mean(Dth1(15:n));mean(Dth6(15:n)); ...
    mean(Dth3(15:n));mean(Dth4(15:n));mean(Dth2(15:n))];
Estrain = [0;E5(4);E1(4);E6(4);E3(4);E4(4);E2(4)];
```

```
Eheat = [0;mean(E5(15:n));mean(E1(15:n));mean(E6(15:n));mean(E3(15:n)); ...
    mean(E4(15:n));mean(E2(15:n))];

H = 3.1894*10^-3;                        % Horizontal laser spot on sample
V = 4.7264*10^-3/sin(23.178*pi/180);     % Vertical laser spot on sample
Area = V*H;                              % Total beam spot
reprate = 1000;                          % Laser repitition rate
E = power./reprate;                      % Energy deposited on sample
R = .03887;                              % Reflectivity of S polarized light
Aflue =  E./Area.*(1 - R)./10;           % Absorbed laser fluence on sample

f = fittype('poly1');                    % Fit heat strain to linear slope
ffit = fit(Aflue,heat,f);

f1 = strcat(num2str(Aflue(2)),' mJ/cm^2');  % Create strings for legend
f2 = strcat(num2str(Aflue(3)),' mJ/cm^2');
f3 = strcat(num2str(Aflue(4)),' mJ/cm^2');
f4 = strcat(num2str(Aflue(5)),' mJ/cm^2');
f5 = strcat(num2str(Aflue(6)),' mJ/cm^2');

% Plot centroid shift as a function of time for 5 fluences with error bars
figure(15); clf; hold on
errorbar(time2,Dth5,E5,'.k-');  % 0.082 W
errorbar(time1,Dth1,E1,'.b-');  % 0.211 W
% errorbar(time,Dth6,E6,'.m-');   % 0.420 W     **** DO NOT USE ****
errorbar(time1,Dth3,E3,'.r-');  % 0.678 W
errorbar(time1,Dth4,E4,'.c-');  % 0.964 W
errorbar(time1,Dth2,E2,'.g-');  % 1.24 W
xlabel('Time (ns)');
ylabel('Peak Shift (mdeg)');
title('GaAs');
%legend({f1;f2;f3;f4;f5},'Location','SouthEast');
xlim([-0.3 3]);

% Plot peak strain and residual heat with error bars
figure(13); clf; hold on;
errorbar(Aflue,strain,Estrain,'k*');
errorbar(Aflue,heat,Eheat,'bo');
plot(ffit);
xlim([0 3.5]);
ylim([0 0.7]);
xlabel('Absorbed Fluence (mJ/cm^2)');
ylabel('Peak shift (mdeg)');
title('GaAs');
legend('Peak Strain','Long-time Heating','Location','NorthWest')

t = toc;     % Stop the clock
```

C.2.2 Extract Centroid Shifts for Each Fluence for GaAs

```
%% chomplite.m
% Written by G. Jackson Williams 9/1/2009

% This is a subroutine to a program takes a modified .mda file from any
% time resolved diffraction data and outputs peak shift vs time.
% This one is for GaAs data.

function [Dth,time,Etot,n,m] = chomplite_GaAs(h)
% Load scans.  These were done as individual rocking curve scans thru time
if(h == 1)
    a = load('-ascii','7idc_0789.txt');     % n time points
    m = 21; n = 31;                         % m angluar points
elseif(h == 2)
    a = load('-ascii','7idc_0794.txt');
    m = 41; n = 31;
elseif(h == 3)
    a = load('-ascii','7idc_0792.txt');
    m = 41; n = 31;
elseif(h == 4)
    a = load('-ascii','7idc_0784.txt');
    m = 41; n = 31;
elseif(h ==5)
    a = load('-ascii','7idc_0787.txt');
    m = 41; n = 31;
else
    a = load('-ascii','7idc_0778_0780_0781.txt');
    m = 41; n = 29;
end


for i = 1:n;                    % For a total of "n" time steps

    if(i == 1)                  % "m" angular points.  p is carried through
        A = p + 1:p + m;        % to index the entire scan file.
    else
        A = max(A)+1:max(A)+m;
    end

    lsroff = a(A,19);           % APD data for Laser Off bucket
    lsron = a(A,20);            % APD data for Laser on bucket
    angle = a(A,2);             % Theta positioner
% ** lsroff, lsron data normalized by hand for top-up occurances. No need
% to normalize to upstream counting APD as it introduces more uncertainty
    Eon = .001*max(lsron).*ones(1,length(angle));
    Eoff = .001*max(lsroff).*ones(1,length(angle));

    [outon] = gaussfit(angle,lsron,Eon);
    [outoff] = gaussfit(angle,lsroff,Eoff);

```

```
    centeroff(:,i) = outoff(1); % Store centroid positions, error
    Ecentoff(:,i) = outoff(2);  % Can not easily preallocate --> n changes

    centeron(:,i) = outon(1);
    Ecenton(:,i) = outon(2);

end
dtime = .1;                          % Each time step is 100 ps
time = dtime*(0:i-1);                % Start time at t = 0

Dth = (centeron - centeroff)*1000;  % Taking the peak shift, in mdeg
Etot = (Ecentoff + Ecenton)*1000;   % Error in the peak shift, in mdeg
end
```

C.2.3 Main Routine for InSb Data Extraction

```
%% Angshift_InSb.m
% Written by G. Jackson Williams 9/1/2009
% Top routine to analyze a 3-D diffraction scan.
%Runs through the 3-D scan of 7idc_0040.txt for InSb at different fluences
clear all;
format short g;

p = 0;                  % Initiating angular indexing
m = 81;                 % Number of angular points in scan
n = 26;                 % Number of time points in scan
hmax = 5;               % Number of waveplate points in the scan
shift = zeros(hmax,n);  % Prealocate space for shift matrix
tic                     % Start the timer for the program

% Calculating the peak shift and residual heating of the crystal
power = [0;0.39;0.74;1.20;1.71;2.20];   % Power meter reading (in W)
H = 4.2105*10^-3;                       % Horizontal beam spot on sample (m)
thetaB = 28.89*pi/180;          % Bragg angle (in radians)
V = 3.1924*10^-3/sin(thetaB);   % Vertiacal beam spot on sample (m)
Area = V*H;                     % Beam spot area
reprate = 5000;                 % Repetition rate of Laser (Hz) (approx)
E = power./reprate;             % Energy delivered on the sample
R = .14368;                     % Reflectivity (S-polarized) of InSb
Aflue =  E./Area.*(1 - R)./10;  % Absorbed laser fluence on the sample

for h = 1:hmax          % For each waveplate scan, do a centroid analysis
    [Dth,time,p,Etot] = chomplite_InSb(p,m,n);
    shift(h,1:n) = Dth;         % Store the centroid analysis array
    E(h,1:n) = Etot/2;          % Store error in centroid fit
end

% Split up shift matrix for ease of understanding
```

```
% All arrays are in increasing order of absorbed fluence
% Dth(X) = centroid shift for fluence index
% E(X) = error in centroid shift for fluence index
Dth1 = shift(1,1:n);    Dth2 = shift(2,1:n);
Dth3 = shift(3,1:n);    Dth4 = shift(4,1:n);    Dth5 = shift(5,1:n);
E1 = E(1,1:n); E2 = E(2,1:n); E3 = E(3,1:n); E4 = E(4,1:n); E5 = E(5,1:n);

f1 = strcat(num2str(Aflue(2)),' mJ/cm^2');
f2 = strcat(num2str(Aflue(3)),' mJ/cm^2');
f3 = strcat(num2str(Aflue(4)),' mJ/cm^2');
f4 = strcat(num2str(Aflue(5)),' mJ/cm^2');
f5 = strcat(num2str(Aflue(6)),' mJ/cm^2');

% Plot of the centroid shifts
figure(10); clf; hold on
errorbar(time,Dth1,E1,'.b-');
errorbar(time,Dth2,E2,'.g-');
errorbar(time,Dth3,E3,'.r-');
errorbar(time,Dth4,E4,'.c-');
errorbar(time,Dth5,E5,'.m-');
ylim([-2.2 0]);
xlabel('Time (ns)');
ylabel('Peak Shift (mdeg)');
title('InSb');
%legend(f1,f2,f3,f4,f5,'Location','SouthEast');

% Calculating the peak shift and residual heating of the crystal
% strain  = maximum centroid shift (in mdeg)
% heat    = averaged data from 1.5 ns to the end of the data run
% Estrain = error associated with the strain measurment at particular time
% Eheat   = error associated with heat measurement
strain = -1*[0;min(Dth1);min(Dth2);min(Dth3);min(Dth4);min(Dth5)];
Estrain = [0;E1(6);E2(6);E3(6);E4(6);E5(6)];
heat = -1*[0;mean(Dth1(10:n));mean(Dth2(10:n));mean(Dth3(10:n)); ...
mean(Dth4(10:n));mean(Dth5(10:n))];
Eheat = [0;mean(E1(10:n));mean(E2(10:n));mean(E3(10:n));mean(E4(10:n)); ...
mean(E5(10:n))];

f = fittype('poly1');  % Fitting both heat and strain to linear slopes
ffit = fit(Aflue,heat,f);
ffit2 = fit(Aflue,strain,f);

% Plot peak, heat strain
figure(12); clf; hold on;
errorbar(Aflue,strain,Estrain,'k*');
errorbar(Aflue,heat,Eheat,'bo');
plot(ffit);
plot(ffit2);
xlabel('Absorbed Fluence (mJ/cm^2)');
ylabel('Peak shifts (mdeg)');
title('InSb');
legend('Peak Strain','Long-time Heating','Location','NorthWest')
ylim([0 2.2]); hold off
xlim([0 1.4]);
```

```
t = toc;     % Stop the clock
```

C.2.4 Extract Centroid Shifts for Each Fluence for InSb

```
%% chomplite_InSb.m
% Written by G. Jackson Williams 9/1/2009
% This is a subroutine to a program takes a modified .mda file from any
% time resolved diffraction data and outputs peak shift vs time.

function [Dth,time,p,Etot] = chomplite_InSb(p,m,n)

a = load('-ascii','7idc_0040.txt');     % Load InSb data
A = p + 1:p + m;                        % Initialize indexing parameter

[lsroff1,lsron1,Eoff1,Eon1] = deadtime(a);

centeroff = zeros(1,n);     % Prealocate space for these arrays
Ecentoff = zeros(1,n);
centeron = zeros(1,n);
Ecenton = zeros(1,n);

for i = 1:n;            % For a total of "n" time steps
    if(i == 1)          % For each time step, the angle index is updated
        A = p + 1:p + m;
    else
        A = max(A)+1:max(A)+m;
    end
    % Detector data for each rocking curve scan:
    lsroff = lsroff1(A);    % APD Data from Laser Off bucket
    lsron = lsron1(A);      % APD Data from Laser On bucket
    Eoff = Eoff1(A);        % Counting statistics for off bucket
    Eon = Eon1(A);          % Counting statistics for off bucket

    apdon = a(A,15);        % Normalization APD Data for Laser On bucket
    apdtot = a(A,14);       % Normalization APD Data for Laser Off bucket
    angle = a(A,2);         % Angle Positioner

    normon = lsroff.*apdtot./(48*apdon);    % Normalize to upstream APD
    normoff = lsron.*apdtot./(48*apdon);    % To remove top-ups

    [outon] = gaussfit(angle,normon,Eon);   % Fit rocking curves to guassian
    [outoff] = gaussfit(angle,normoff,Eoff);

    centeroff(:,i) = outoff(1);      % Extract Centroid
    Ecentoff(:,i) = outoff(2);       % and error in fit due to counting
                                     % statistics and fit residuals
    centeron(:,i) = outon(1);        % for both lsr on and lsr off
```

```
    Ecenton(:,i) = outon(2);

end

Dth = (centeroff - centeron)*1000;  % Taking the peak shift, in mdeg

dtime = .1;                         % Each time step is 100 ps
time = dtime*(0:i-1);               % Start at t = 0
p = max(A);                         % keep file index to start at next 2-D scan
Etot = (Ecentoff+Ecenton)*1000; % Error in the peak shift, in mdeg
end

% Detector Definitions
%     Column 8     Det 6 Lsr Rep Rate
%     Column 9     Det 7  APD_B_tot             NO
%     Column 10    Det 8 APD_B_off              YES  lsroff
%     Column 11    Det 9 APD_B_on               YES  lsron
%     Column 12    Det 10 APD_B_off_late        NO
%     Column 13    Det 11 APD_B_on_late         YES  lsrlate
%     Column 14    Det 12 APD_A_tot (normalization)
%     Column 15    Det 13 APD_A_on (gated every bunch with P0 at 271 kHz)
%     Column 16    Det 14 APD_A_late (gated every bunch with P0 at 271 kHz)
```

C.2.5 Deadtime Correction Subroutine

```
%% Program to correct for the deadtime of photon counting APDs
% Written by G. Jackson Williams
% circa 9/1/2009

function [lsroff1,lsron1,Eoff,Eon] = deadtime(a)
    t = 1;                  % Counting time
    T = 1./a(:,8);          % Repitition Rate of the laser
    lsroff = a(:,10);       % N_O (observed count rate)
    lsron = a(:,11);        % N_O (observed count rate)
    tau = 1./a(:,8);        % Repetition rate of the laser
% Return corrected (true) count rate for entire data set-(fluence and angle)
    lsroff1 = -(1./tau).*log(1 - lsroff.*tau);
    lsron1 = -(1./tau).*log(1 - lsron.*tau);
% Return deadtime correction counting statistics
    Eoff = 1./((1-T.*lsroff)).*sqrt(lsroff./t);
    Eon = 1./((1-T.*lsron)).*sqrt(lsron./t);
end
```

C.3 Dispersion Correction Terms $\Delta f'$ and $\Delta f''$

Data taken from [19] or available on the web at
http://henke.lbl.gov/optical_constants/asf.html

C.3.1 Indium

```
% Energy (eV)   f'              f''
  1000.000      −9.620117       20.60602
  1100.000      −8.054237       18.47271
  1200.000      −7.008023       16.63640
  1300.000      −6.270947       15.05404
  1400.000      −5.770803       13.68025
  1500.000      −5.439097       12.48567
  1600.000      −5.212864       11.43919
  1700.000      −5.076109       10.51707
  1800.000      −5.081061       9.703634
  1900.000      −5.118416       8.995317
  2000.000      −5.143920       8.362679
  2100.000      −5.204079       7.794830
  2200.000      −5.294268       7.282991
  2300.000      −5.415628       6.819891
  2400.000      −5.558311       6.399615
  2500.000      −5.725870       6.016752
  2600.000      −5.918964       5.666907
  2700.000      −6.180744       5.348144
  2800.000      −6.431940       5.057722
  2900.000      −6.747009       4.792847
  3000.000      −7.077412       4.548751
  3100.000      −7.458972       4.326771
  3200.000      −7.910831       4.121375
  3300.000      −8.461382       3.930896
  3400.000      −9.162023       3.753936
  3500.000      −10.11621       3.589182
  3600.000      −11.60928       3.435501
  3633.000      −12.36531       3.387042
  3638.000      −12.50117       3.379793
  3643.000      −12.64437       3.372568
  3648.000      −12.79578       3.365368
  3653.000      −12.95641       3.358191
  3658.000      −13.12748       3.351039
  3663.000      −13.31050       3.343911
  3668.000      −13.50729       3.336806
  3673.000      −13.72018       3.329725
  3678.000      −13.95207       3.322668
  3683.000      −14.20684       3.315634
  3688.000      −14.48958       3.308623
  3693.000      −14.80739       3.301635
```

3698.000	−15.17043	3.294671
3700.000	−15.33152	3.291891
3703.000	−15.59412	3.287729
3708.000	−16.10328	3.280810
3713.000	−16.74225	3.273914
3718.000	−17.60205	3.267041
3723.000	−18.92500	3.260190
3728.000	−21.94412	3.253362
3733.000	−21.15192	11.04794
3738.000	−18.65468	11.01754
3743.000	−17.43659	10.98730
3748.000	−16.62749	10.95725
3753.000	−16.02358	10.92737
3758.000	−15.54389	10.89766
3763.000	−15.14781	10.86812
3768.000	−14.81213	10.83876
3773.000	−14.52228	10.80956
3778.000	−14.26855	10.78053
3783.000	−14.04416	10.75166
3788.000	−13.84414	10.72296
3793.000	−13.66484	10.69443
3798.000	−13.50342	10.66606
3800.000	−13.44335	10.65475
3803.000	−13.35770	10.63785
3808.000	−13.22596	10.60979
3813.000	−13.10684	10.58190
3818.000	−12.99924	10.55417
3823.000	−12.90230	10.52659
3828.000	−12.81532	10.49917
3841.000	−12.63241	10.42859
3846.000	−12.57788	10.40172
3851.000	−12.53192	10.37499
3856.000	−12.49459	10.34842
3861.000	−12.46603	10.32199
3866.000	−12.44654	10.29572
3871.000	−12.43659	10.26958
3876.000	−12.43685	10.24360
3881.000	−12.44824	10.21775
3886.000	−12.47201	10.19205
3891.000	−12.50989	10.16649
3896.000	−12.56427	10.14108
3900.000	−12.62188	10.12084
3901.000	−12.63853	10.11580
3906.000	−12.73760	10.09066
3911.000	−12.86905	10.06565
3916.000	−13.04523	10.04079
3921.000	−13.28822	10.01606
3926.000	−13.64383	9.991458
3931.000	−14.23485	9.966997
3936.000	−15.70340	9.942667
3941.000	−15.14090	13.78414
3946.000	−13.86299	13.74954
3951.000	−13.19963	13.71513
3956.000	−12.73658	13.68091

3961.000	−12.37510	13.64688
3966.000	−12.07558	13.61304
3971.000	−11.81815	13.57939
3976.000	−11.59133	13.54593
3981.000	−11.38792	13.51265
3986.000	−11.20307	13.47956
3991.000	−11.03338	13.44664
3996.000	−10.87636	13.41391
4000.000	−10.75858	13.38786
4001.000	−10.73012	13.38136
4006.000	−10.59320	13.34899
4011.000	−10.46446	13.31679
4016.000	−10.34299	13.28478
4021.000	−10.22800	13.25293
4026.000	−10.11888	13.22126
4031.000	−10.01512	13.18976
4036.000	−9.916277	13.15844
4100.000	−8.972916	12.77208
4140.000	−8.616801	12.54372
4145.000	−8.584288	12.51585
4150.000	−8.554716	12.48812
4155.000	−8.528238	12.46054
4160.000	−8.505053	12.43311
4165.000	−8.485400	12.40582
4170.000	−8.469594	12.37867
4175.000	−8.458027	12.35166
4180.000	−8.451204	12.32480
4185.000	−8.449775	12.29807
4190.000	−8.454600	12.27148
4195.000	−8.466843	12.24503
4200.000	−8.488109	12.21872
4205.000	−8.520723	12.19254
4210.000	−8.568189	12.16650
4215.000	−8.636155	12.14060
4220.000	−8.734588	12.11483
4225.000	−8.883768	12.08919
4230.000	−9.136117	12.06368
4235.000	−9.734893	12.03830
4240.000	−9.689471	13.86571
4245.000	−8.994583	13.83905
4250.000	−8.647552	13.81252
4255.000	−8.404243	13.78612
4260.000	−8.211948	13.75986
4265.000	−8.050273	13.73372
4270.000	−7.909103	13.70771
4275.000	−7.782726	13.68183
4280.000	−7.667568	13.65607
4285.000	−7.561257	13.63045
4290.000	−7.462104	13.60494
4295.000	−7.368905	13.57957
4300.000	−7.280745	13.55431
4305.000	−7.196927	13.52918
4310.000	−7.116878	13.50417
4315.000	−7.040160	13.47928

```
4320.000      −6.966408       13.45452
4325.000      −6.895326       13.42987
4330.000      −6.826648       13.40534
4335.000      −6.760167       13.38093
4400.000      −6.036684       13.07408
4500.000      −5.216025       12.63747
4600.000      −4.586904       12.23960
4700.000      −4.076517       11.87628
4800.000      −3.648225       11.54393
4900.000      −3.051923       11.21557
5000.000      −2.716684       10.88601
5100.000      −2.423279       10.57544
5200.000      −2.053329       10.26510
5300.000      −1.817399       9.965174
5400.000      −1.608070       9.678737
5500.000      −1.421609       9.404993
5600.000      −1.242030       9.141077
5700.000      −1.091969       8.887983
5800.000     −0.9573733       8.645290
5900.000     −0.8364584       8.412432
6000.000     −0.7276968       8.188873
6100.000     −0.6297747       7.974123
6200.000     −0.5415545       7.767715
6300.000     −0.4620449       7.569220
6400.000     −0.3903795       7.378234
6500.000     −0.3257951       7.194379
6600.000     −0.2676182       7.017301
6700.000     −0.2152517       6.846665
6800.000     −0.1681646       6.682161
6900.000     −0.1258835       6.523497
7000.000     −8.7984264E−02   6.370395
7100.000     −5.4086655E−02   6.222597
7200.000     −2.3848634E−02   6.079858
7300.000      3.0379370E−03   5.941947
7400.000      2.5742525E−02   5.808653
7500.000      3.9831575E−02   5.679974
7600.000      5.8204472E−02   5.555813
7700.000      7.4223846E−02   5.435678
7800.000      8.8077143E−02   5.319394
7900.000      9.5412686E−02   5.206873
8000.000      0.1053914       5.098123
8100.000      0.1136909       4.992754
8200.000      0.1204404       4.890626
8300.000      0.1257550       4.791605
8400.000      0.1289506       4.695578
8500.000      0.1261521       4.602493
8600.000      0.1277380       4.512395
8700.000      0.1282909       4.424940
8800.000      0.1278871       4.340022
8900.000      0.1265974       4.257545
9000.000      0.1245486       4.177756
9100.000      0.1217746       4.100235
9200.000      0.1183310       4.024898
9300.000      0.1142692       3.951659
```

```
9400.000      0.1096367       3.880442
9500.000      0.1044773       3.811170
9600.000      9.8831564E-02   3.743773
9700.000      9.2737019E-02   3.678183
9800.000      8.6228229E-02   3.614334
9900.000      7.9337433E-02   3.552165
10000.00      7.2094239E-02   3.491616
10100.00      6.4526290E-02   3.432629
10200.00      5.6659203E-02   3.375152
10300.00      4.8516531E-02   3.319132
10400.00      4.0120408E-02   3.264520
10500.00      3.1491078E-02   3.211268
10600.00      2.2647552E-02   3.159331
10700.00      1.3607492E-02   3.108665
10800.00      4.3870425E-03   3.059227
10900.00     -4.9984660E-03   3.010980
11000.00     -1.4535142E-02   2.963883
11100.00     -2.4209827E-02   2.917900
11200.00     -3.4010295E-02   2.872996
11300.00     -4.3925460E-02   2.829136
11400.00     -5.3944673E-02   2.786288
11500.00     -6.4058408E-02   2.744421
11600.00     -7.4257568E-02   2.703504
11700.00     -8.4533669E-02   2.663510
11800.00     -9.4879173E-02   2.624408
11900.00     -0.1052867       2.586174
12000.00     -0.1157497       2.548781
12100.00     -0.1262621       2.512203
12200.00     -0.1368179       2.476419
12300.00     -0.1474122       2.441403
12400.00     -0.1580406       2.407135
12500.00     -0.1701095       2.373597
12600.00     -0.1808073       2.340777
12700.00     -0.1915212       2.308642
12800.00     -0.2022513       2.277173
12900.00     -0.2129946       2.246352
13000.00     -0.2237483       2.216160
13100.00     -0.2345093       2.186581
13200.00     -0.2463433       2.157599
13300.00     -0.2571144       2.129208
13400.00     -0.2678905       2.101380
13500.00     -0.2786658       2.074101
13600.00     -0.2894384       2.047357
13700.00     -0.3002066       2.021133
13800.00     -0.3109696       1.995416
13900.00     -0.3217258       1.970193
14000.00     -0.3324746       1.945451
14100.00     -0.3432152       1.921177
14200.00     -0.3539466       1.897360
14300.00     -0.3646685       1.873988
14400.00     -0.3753802       1.851050
14500.00     -0.3860818       1.828535
14600.00     -0.3967727       1.806433
14700.00     -0.4074528       1.784734
```

14800.00	−0.4181222	1.763427
14900.00	−0.4287809	1.742503
15000.00	−0.4394290	1.721953
15100.00	−0.4500668	1.701768
15200.00	−0.4606945	1.681939
15300.00	−0.4713125	1.662459
15400.00	−0.4819210	1.643317
15500.00	−0.4925076	1.624508
15600.00	−0.5033034	1.606024
15700.00	−0.5138884	1.587856
15800.00	−0.5244666	1.569998
15900.00	−0.5350385	1.552442
16000.00	−0.5456047	1.535181
16100.00	−0.5561627	1.518209
16200.00	−0.5685115	1.501531
16300.00	−0.5790550	1.485150
16400.00	−0.5896059	1.469038
16500.00	−0.6001569	1.453189
16600.00	−0.6107085	1.437597
16700.00	−0.6212618	1.422258
16800.00	−0.6318178	1.407165
16900.00	−0.6423778	1.392314
17000.00	−0.6529418	1.377698
17100.00	−0.6650278	1.363322
17200.00	−0.6756017	1.349190
17300.00	−0.6861889	1.335278
17400.00	−0.6967878	1.321583
17500.00	−0.7073996	1.308100
17600.00	−0.7180257	1.294823
17700.00	−0.7286680	1.281750
17800.00	−0.7393280	1.268876
17900.00	−0.7500080	1.256197
18000.00	−0.7607096	1.243708
18100.00	−0.7714351	1.231406
18200.00	−0.7821867	1.219288
18300.00	−0.7929702	1.207349
18400.00	−0.8060690	1.195600
18500.00	−0.8169246	1.184048
18600.00	−0.8278037	1.172664
18700.00	−0.8387176	1.161446
18800.00	−0.8496690	1.150391
18900.00	−0.8606611	1.139494
19000.00	−0.8716962	1.128754
19100.00	−0.8827770	1.118167
19200.00	−0.8939061	1.107730
19300.00	−0.9050862	1.097440
19400.00	−0.9163203	1.087294
19500.00	−0.9276114	1.077291
19600.00	−0.9389625	1.067426
19700.00	−0.9503766	1.057698
19800.00	−0.9618567	1.048104
19900.00	−0.9734068	1.038642
20000.00	−0.9850299	1.029308
20100.00	−0.9967297	1.020101

20200.00	−1.008510	1.011019
20300.00	−1.020374	1.002059
20400.00	−1.032327	0.9932181
20500.00	−1.044371	0.9844953
20600.00	−1.056513	0.9758883
20700.00	−1.068755	0.9673947
20800.00	−1.081103	0.9590129
20900.00	−1.093562	0.9507405
21000.00	−1.106136	0.9425758
21100.00	−1.118830	0.9345169
21200.00	−1.131651	0.9265619
21300.00	−1.144603	0.9187092
21400.00	−1.157693	0.9109567
21500.00	−1.170927	0.9033028
21600.00	−1.184310	0.8957459
21700.00	−1.197851	0.8882844
21800.00	−1.211556	0.8809167
21900.00	−1.225432	0.8736409
22000.00	−1.239488	0.8664557
22100.00	−1.253731	0.8593596
22200.00	−1.268169	0.8523510
22300.00	−1.282812	0.8454286
22400.00	−1.297670	0.8385908
22500.00	−1.312753	0.8318363
22600.00	−1.328070	0.8251638
22700.00	−1.343634	0.8185719
22800.00	−1.359455	0.8120593
22900.00	−1.375547	0.8056247
23000.00	−1.391922	0.7992668
23100.00	−1.408595	0.7929844
23200.00	−1.425581	0.7867764
23300.00	−1.442896	0.7806416
23400.00	−1.460556	0.7745786
23500.00	−1.478580	0.7685865
23600.00	−1.496987	0.7626642
23700.00	−1.515797	0.7568104
23800.00	−1.535034	0.7510244
23900.00	−1.554720	0.7453048
24000.00	−1.574883	0.7396507
24100.00	−1.595548	0.7340611
24200.00	−1.616747	0.7285349
24300.00	−1.638511	0.7230715
24400.00	−1.660876	0.7176694
24500.00	−1.683881	0.7123281
24600.00	−1.707566	0.7070464
24700.00	−1.731978	0.7018237
24800.00	−1.757165	0.6966589
24900.00	−1.783184	0.6915511

C.3.2 Antimony

```
% Energy (eV)   f'              f''
  1000.000      −11.80711       24.04015
  1100.000      −9.505189       21.63727
  1200.000      −7.983030       19.55356
  1300.000      −6.937045       17.73706
  1400.000      −6.199494       16.15649
  1500.000      −5.661477       14.77380
  1600.000      −5.315005       13.55524
  1700.000      −5.055348       12.48680
  1800.000      −4.883482       11.53821
  1900.000      −4.797727       10.69303
  2000.000      −4.748501       9.936948
  2100.000      −4.742525       9.257375
  2200.000      −4.890482       8.655450
  2300.000      −4.945248       8.113972
  2400.000      −5.024939       7.621761
  2500.000      −5.127174       7.172884
  2600.000      −5.250607       6.762289
  2700.000      −5.394918       6.385658
  2800.000      −5.561098       6.039280
  2900.000      −5.757222       5.720049
  3000.000      −5.994437       5.425198
  3100.000      −6.222447       5.161564
  3200.000      −6.477096       4.917472
  3300.000      −6.765496       4.691054
  3400.000      −7.091969       4.480657
  3500.000      −7.468798       4.284714
  3600.000      −7.912734       4.101889
  3700.000      −8.450916       3.930999
  3800.000      −9.132996       3.771023
  3900.000      −10.05588       3.621086
  4000.000      −11.49109       3.480281
  4035.000      −12.26530       3.433017
  4040.000      −12.39764       3.426346
  4045.000      −12.53718       3.419696
  4050.000      −12.68478       3.413067
  4055.000      −12.84142       3.406457
  4060.000      −13.00835       3.399868
  4065.000      −13.18703       3.393298
  4070.000      −13.37927       3.386748
  4075.000      −13.58734       3.380218
  4080.000      −13.81419       3.373708
  4085.000      −14.06357       3.367217
  4090.000      −14.34055       3.360745
  4095.000      −14.65212       3.354294
  4100.000      −15.00836       3.347861
  4105.000      −15.42443       3.341448
  4110.000      −15.92482       3.335053
  4115.000      −16.55297       3.328679
```

```
4120.000      −17.39820       3.322323
4125.000      −18.69591       3.315986
4130.000      −21.61562       3.309667
4135.000      −21.02710       11.06989
4140.000      −18.47883       11.03836
4145.000      −17.24737       11.00703
4150.000      −16.42999       10.97591
4155.000      −15.81923       10.94498
4160.000      −15.33313       10.91426
4165.000      −14.93064       10.88373
4170.000      −14.58841       10.85339
4175.000      −14.29177       10.82325
4180.000      −14.03097       10.79331
4185.000      −13.79909       10.76355
4190.000      −13.59117       10.73398
4195.000      −13.40348       10.70459
4200.000      −13.23316       10.67540
4205.000      −13.07793       10.64639
4210.000      −12.93603       10.61755
4215.000      −12.80599       10.58891
4220.000      −12.68668       10.56044
4225.000      −12.57708       10.53215
4230.000      −12.47643       10.50404
4283.000      −11.84502       10.21658
4288.000      −11.82186       10.19042
4293.000      −11.80506       10.16443
4298.000      −11.79486       10.13859
4300.000      −11.79271       10.12830
4303.000      −11.79162       10.11291
4308.000      −11.79578       10.08739
4313.000      −11.80796       10.06202
4318.000      −11.82891       10.03681
4323.000      −11.85965       10.01175
4328.000      −11.90151       9.986842
4333.000      −11.95625       9.962086
4338.000      −12.02622       9.937481
4343.000      −12.11484       9.913022
4348.000      −12.22689       9.888711
4353.000      −12.36969       9.864546
4358.000      −12.55505       9.840529
4363.000      −12.80395       9.816654
4368.000      −13.15910       9.792922
4373.000      −13.73182       9.769332
4378.000      −15.04990       9.745885
4383.000      −14.90222       13.57064
4388.000      −13.52772       13.53626
4393.000      −12.85290       13.50208
4398.000      −12.39108       13.46813
4400.000      −12.23893       13.45460
4403.000      −12.03474       13.43438
4408.000      −11.74198       13.40083
4413.000      −11.49199       13.36750
4418.000      −11.27291       13.33437
4423.000      −11.07733       13.30145
```

4428.000	−10.90027	13.26872
4433.000	−10.73827	13.23620
4438.000	−10.58879	13.20388
4443.000	−10.44995	13.17176
4448.000	−10.32025	13.13983
4453.000	−10.19854	13.10810
4458.000	−10.08389	13.07656
4463.000	−9.975549	13.04522
4468.000	−9.872877	13.01406
4473.000	−9.775362	12.98309
4478.000	−9.682563	12.95232
4500.000	−9.321861	12.81909
4600.000	−8.350879	12.25607
4601.000	−8.345910	12.25077
4606.000	−8.322629	12.22437
4611.000	−8.302059	12.19813
4616.000	−8.284369	12.17204
4621.000	−8.269765	12.14611
4626.000	−8.258502	12.12033
4631.000	−8.250902	12.09470
4636.000	−8.247368	12.06922
4641.000	−8.248412	12.04389
4646.000	−8.254697	12.01871
4651.000	−8.267096	11.99367
4656.000	−8.286781	11.96878
4661.000	−8.315382	11.94404
4666.000	−8.355250	11.91944
4671.000	−8.409937	11.89498
4676.000	−8.485182	11.87067
4681.000	−8.591166	11.84650
4686.000	−8.748684	11.82247
4691.000	−9.012354	11.79857
4696.000	−9.646976	11.77482
4700.000	−9.793721	13.59795
4701.000	−9.514109	13.59295
4706.000	−8.859342	13.56806
4711.000	−8.526525	13.54332
4716.000	−8.293218	13.51871
4721.000	−8.109350	13.49423
4726.000	−7.955288	13.46990
4731.000	−7.821229	13.44569
4736.000	−7.701613	13.42163
4741.000	−7.592951	13.39769
4746.000	−7.492924	13.37389
4751.000	−7.399879	13.35022
4756.000	−7.312633	13.32668
4761.000	−7.230290	13.30327
4766.000	−7.152167	13.27999
4771.000	−7.077701	13.25684
4776.000	−7.006462	13.23381
4781.000	−6.938091	13.21092
4786.000	−6.872299	13.18815
4791.000	−6.808825	13.16550
4796.000	−6.747465	13.14297

```
4800.000      −6.699776       13.12504
4900.000      −5.765469       12.70139
5000.000      −5.102882       12.32126
5100.000      −4.583796       11.97982
5200.000      −4.157225       11.67296
5300.000      −3.795290       11.39715
5400.000      −3.122936       11.13059
5500.000      −2.821460       10.83750
5600.000      −2.555288       10.56187
5700.000      −2.147382       10.30077
5800.000      −1.922743       10.02468
5900.000      −1.721841       9.759982
6000.000      −1.541518       9.506063
6100.000      −1.379160       9.262341
6200.000      −1.220096       9.026402
6300.000      −1.086831       8.799265
6400.000     −0.9661846       8.580628
6500.000     −0.8568169       8.370067
6600.000     −0.7575686       8.167182
6700.000     −0.6674300       7.971601
6800.000     −0.5855171       7.782971
6900.000     −0.5110527       7.600965
7000.000     −0.4433494       7.425272
7100.000     −0.3817973       7.255600
7200.000     −0.3258536       7.091674
7300.000     −0.2750331       6.933233
7400.000     −0.2289017       6.780035
7500.000     −0.1870687       6.631847
7600.000     −0.1491827       6.488451
7700.000     −0.1149265       6.349641
7800.000     −8.4013142E−02   6.215221
7900.000     −5.6183465E−02   6.085007
8000.000     −3.1202115E−02   5.958823
8100.000     −8.8558793E−03   5.836503
8200.000      1.1047892E−02   5.717890
8300.000      2.2593230E−02   5.602978
8400.000      3.8073659E−02   5.491742
8500.000      5.1603872E−02   5.383783
8600.000      6.3303068E−02   5.278973
8700.000      7.3269002E−02   5.177189
8800.000      7.7152573E−02   5.078423
8900.000      8.3780266E−02   4.982624
9000.000      8.9963034E−02   4.890071
9100.000      9.4975851E−02   4.800124
9200.000      9.8902687E−02   4.712685
9300.000      0.1018212       4.627656
9400.000      0.1034972       4.544953
9500.000      0.1045515       4.464508
9600.000      0.1047990       4.386224
9700.000      0.1042965       4.310025
9800.000      0.1030971       4.235836
9900.000      0.1012531       4.163585
10000.00      9.8678328E−02   4.093205
10100.00      9.5506266E−02   4.024632
```

```
10200.00      9.1962896E-02   3.957804
10300.00      8.7934487E-02   3.892659
10400.00      8.3456486E-02   3.829142
10500.00      7.8560412E-02   3.767197
10600.00      7.3275670E-02   3.706771
10700.00      6.7629695E-02   3.647815
10800.00      6.1647858E-02   3.590281
10900.00      5.5354048E-02   3.534122
11000.00      4.8770312E-02   3.479294
11100.00      4.1917399E-02   3.425756
11200.00      3.4814678E-02   3.373466
11300.00      2.7480043E-02   3.322384
11400.00      1.9930463E-02   3.272475
11500.00      1.2181519E-02   3.223700
11600.00      4.2479681E-03   3.176027
11700.00     -3.8563842E-03   3.129421
11800.00     -1.2118864E-02   3.083849
11900.00     -2.0527324E-02   3.039283
12000.00     -2.9070716E-02   2.995691
12100.00     -3.7738487E-02   2.953044
12200.00     -4.6520751E-02   2.911317
12300.00     -5.5408530E-02   2.870480
12400.00     -6.4393088E-02   2.830511
12500.00     -7.3466599E-02   2.791382
12600.00     -8.2621500E-02   2.753071
12700.00     -9.1850720E-02   2.715556
12800.00     -0.1011479       2.678812
12900.00     -0.1105068       2.642820
13000.00     -0.1199219       2.607559
13100.00     -0.1293878       2.573008
13200.00     -0.1388994       2.539149
13300.00     -0.1484523       2.505962
13400.00     -0.1580421       2.473431
13500.00     -0.1676648       2.441537
13600.00     -0.1773168       2.410263
13700.00     -0.1869944       2.379595
13800.00     -0.1966945       2.349515
13900.00     -0.2064141       2.320009
14000.00     -0.2161506       2.291061
14100.00     -0.2259012       2.262659
14200.00     -0.2356635       2.234788
14300.00     -0.2456708       2.207434
14400.00     -0.2572366       2.180591
14500.00     -0.2670264       2.154254
14600.00     -0.2768171       2.128397
14700.00     -0.2866097       2.103008
14800.00     -0.2964028       2.078076
14900.00     -0.3061953       2.053590
15000.00     -0.3159861       2.029539
15100.00     -0.3257742       2.005913
15200.00     -0.3355593       1.982702
15300.00     -0.3466452       1.959902
15400.00     -0.3564211       1.937504
15500.00     -0.3661904       1.915492
```

15600.00	−0.3759529	1.893857
15700.00	−0.3857084	1.872590
15800.00	−0.3954565	1.851684
15900.00	−0.4051970	1.831129
16000.00	−0.4149298	1.810918
16100.00	−0.4246547	1.791044
16200.00	−0.4343716	1.771498
16300.00	−0.4440804	1.752273
16400.00	−0.4537815	1.733363
16500.00	−0.4634750	1.714760
16600.00	−0.4731609	1.696458
16700.00	−0.4828395	1.678449
16800.00	−0.4925109	1.660729
16900.00	−0.5021759	1.643290
17000.00	−0.5118346	1.626127
17100.00	−0.5214876	1.609234
17200.00	−0.5311353	1.592604
17300.00	−0.5407780	1.576234
17400.00	−0.5504167	1.560116
17500.00	−0.5600520	1.544246
17600.00	−0.5696844	1.528619
17700.00	−0.5793166	1.513229
17800.00	−0.5891474	1.498075
17900.00	−0.5988278	1.483148
18000.00	−0.6104063	1.468477
18100.00	−0.6200312	1.454026
18200.00	−0.6296562	1.439790
18300.00	−0.6392828	1.425764
18400.00	−0.6489127	1.411943
18500.00	−0.6585468	1.398324
18600.00	−0.6681861	1.384903
18700.00	−0.6778318	1.371676
18800.00	−0.6874846	1.358639
18900.00	−0.6971462	1.345788
19000.00	−0.7083941	1.333125
19100.00	−0.7180721	1.320661
19200.00	−0.7277620	1.308373
19300.00	−0.7374650	1.296258
19400.00	−0.7471827	1.284311
19500.00	−0.7569164	1.272531
19600.00	−0.7666674	1.260913
19700.00	−0.7764372	1.249454
19800.00	−0.7862270	1.238153
19900.00	−0.7960388	1.227006
20000.00	−0.8058740	1.216009
20100.00	−0.8157342	1.205161
20200.00	−0.8256211	1.194458
20300.00	−0.8355370	1.183899
20400.00	−0.8478423	1.173494
20500.00	−0.8578241	1.163248
20600.00	−0.8678378	1.153137
20700.00	−0.8778864	1.143159
20800.00	−0.8879718	1.133312
20900.00	−0.8980965	1.123593

21000.00	−0.9082623	1.114000
21100.00	−0.9184713	1.104530
21200.00	−0.9287258	1.095182
21300.00	−0.9390277	1.085954
21400.00	−0.9493799	1.076844
21500.00	−0.9597845	1.067848
21600.00	−0.9702440	1.058967
21700.00	−0.9807608	1.050196
21800.00	−0.9913374	1.041536
21900.00	−1.001977	1.032983
22000.00	−1.012682	1.024537
22100.00	−1.023455	1.016194
22200.00	−1.034300	1.007954
22300.00	−1.045219	0.9998155
22400.00	−1.056216	0.9917758
22500.00	−1.067293	0.9838335
22600.00	−1.078455	0.9759872
22700.00	−1.089705	0.9682353
22800.00	−1.101046	0.9605765
22900.00	−1.112482	0.9530089
23000.00	−1.124018	0.9455312
23100.00	−1.135657	0.9381419
23200.00	−1.147403	0.9308398
23300.00	−1.159261	0.9236235
23400.00	−1.171236	0.9164914
23500.00	−1.183332	0.9094423
23600.00	−1.195555	0.9024749
23700.00	−1.207909	0.8955880
23800.00	−1.220399	0.8887804
23900.00	−1.233033	0.8820506
24000.00	−1.245815	0.8753976
24100.00	−1.258751	0.8688202
24200.00	−1.271849	0.8623172
24300.00	−1.285115	0.8558877
24400.00	−1.298555	0.8495302
24500.00	−1.312179	0.8432438
24600.00	−1.325992	0.8370275
24700.00	−1.340004	0.8308802
24800.00	−1.354224	0.8248008
24900.00	−1.368660	0.8187884

C.3.3 Gallium

```
% Energy (eV)   f'              f''
  1000.000      −12.78024       2.622440
  1100.000      −23.67351       2.312109
  1200.000      −2.682566       11.65662
  1205.000      −3.065672       10.81520
  1210.000      −3.465937       10.08000
  1215.000      −3.875939       9.435927
  1220.000      −4.290639       8.870313
  1225.000      −4.706735       8.372511
  1230.000      −5.122201       7.933538
  1235.000      −5.535975       7.545800
  1240.000      −5.947742       7.202854
  1245.000      −6.357804       6.899230
  1250.000      −6.766998       6.630270
  1255.000      −7.176702       6.392002
  1260.000      −7.588907       6.181035
  1265.000      −8.006413       5.994472
  1270.000      −8.433251       5.829834
  1275.000      −8.875569       5.685009
  1280.000      −9.343676       5.558189
  1285.000      −9.857612       5.447840
  1290.000      −10.46733       5.352658
  1295.000      −11.39250       5.271546
  1300.000      −11.80414       7.023297
  1305.000      −11.45599       6.967597
  1310.000      −11.47662       6.923607
  1315.000      −11.60475       6.890850
  1320.000      −11.78719       6.868974
  1325.000      −12.00424       6.857738
  1330.000      −12.24675       6.857008
  1335.000      −12.51003       6.866754
  1340.000      −12.79155       6.887047
  1345.000      −13.09006       6.918058
  1350.000      −13.40507       6.960057
  1355.000      −13.73658       7.013420
  1360.000      −14.08498       7.078628
  1365.000      −14.45092       7.156275
  1370.000      −14.83532       7.247075
  1375.000      −15.23928       7.351871
  1380.000      −15.66408       7.471646
  1385.000      −16.11121       7.607537
  1390.000      −16.58234       7.760849
  1395.000      −17.07932       7.933075
  1400.000      −17.60420       8.125916
  1500.000      −4.018536       12.44893
  1600.000      −2.885425       11.31038
  1700.000      −2.145375       10.32254
  1800.000      −1.592947       9.482872
  1900.000      −1.184808       8.750233
```

```
2000.000     −0.8953396       8.107148
2100.000     −0.6709451       7.539242
2200.000     −0.4910424       7.033835
2300.000     −0.2669138       6.570822
2400.000     −0.1589576       6.143772
2500.000     −7.8631461E−02   5.756646
2600.000     −2.8784975E−02   5.404647
2700.000      1.1684831E−02   5.085346
2800.000      3.8398005E−02   4.793488
2900.000      5.4030951E−02   4.525991
3000.000      5.7593603E−02   4.280249
3100.000      5.6503318E−02   4.055951
3200.000      4.9936719E−02   3.849130
3300.000      3.8955834E−02   3.657989
3400.000      2.4415979E−02   3.480960
3500.000      7.0093237E−03   3.316668
3600.000     −1.2702152E−02   3.163903
3700.000     −3.4260809E−02   3.021596
3800.000     −5.7292998E−02   2.888803
3900.000     −8.1493519E−02   2.764682
4000.000     −0.1066125       2.648485
4100.000     −0.1324460       2.539543
4200.000     −0.1588271       2.437257
4300.000     −0.1856200       2.341089
4400.000     −0.2127144       2.250556
4500.000     −0.2400214       2.165220
4600.000     −0.2674696       2.084686
4700.000     −0.2950028       2.008598
4800.000     −0.3225760       1.936629
4900.000     −0.3527754       1.868593
5000.000     −0.3820444       1.804215
5100.000     −0.4095708       1.743193
5200.000     −0.4370374       1.685247
5300.000     −0.4644422       1.630172
5400.000     −0.4917867       1.577779
5500.000     −0.5190772       1.527894
5600.000     −0.5463270       1.480357
5700.000     −0.5766885       1.435150
5800.000     −0.6039156       1.392048
5900.000     −0.6311359       1.350885
6000.000     −0.6583713       1.311545
6100.000     −0.6856458       1.273920
6200.000     −0.7129853       1.237912
6300.000     −0.7404187       1.203427
6400.000     −0.7679761       1.170380
6500.000     −0.7956909       1.138691
6600.000     −0.8235986       1.108286
6700.000     −0.8517374       1.079096
6800.000     −0.8801485       1.051055
6900.000     −0.9088759       1.024103
7000.000     −0.9379674      0.9981853
7100.000     −0.9674743      0.9732476
7200.000     −0.9974524      0.9492409
7300.000      −1.027962      0.9261189
```

7400.000	−1.059070	0.9038382
7500.000	−1.090847	0.8823581
7600.000	−1.123374	0.8616402
7700.000	−1.156737	0.8416483
7800.000	−1.191034	0.8223487
7900.000	−1.226374	0.8037095
8000.000	−1.262904	0.7857007
8100.000	−1.300705	0.7682937
8200.000	−1.339959	0.7514619
8300.000	−1.380844	0.7351796
8400.000	−1.423561	0.7194232
8500.000	−1.468345	0.7041699
8600.000	−1.515470	0.6893983
8700.000	−1.565254	0.6750884
8800.000	−1.618083	0.6612206
8900.000	−1.674413	0.6477770
9000.000	−1.734817	0.6348592
9100.000	−1.799964	0.6223299
9200.000	−1.870713	0.6101736
9300.000	−1.948166	0.5983752
9400.000	−2.033750	0.5869208
9500.000	−2.129380	0.5757968
9600.000	−2.237686	0.5649906
9700.000	−2.362435	0.5544900
9800.000	−2.509282	0.5442833
9900.000	−2.687268	0.5343597
10000.00	−2.912190	0.5247084
10100.00	−3.215471	0.5153197
10200.00	−3.674937	0.5061839
10270.00	−4.222119	0.4999343
10275.00	−4.276143	0.4994925
10280.00	−4.333321	0.4990512
10285.00	−4.394018	0.4986105
10290.00	−4.458680	0.4981703
10295.00	−4.527843	0.4977308
10300.00	−4.602160	0.4972918
10305.00	−4.682434	0.4968535
10310.00	−4.769671	0.4964157
10315.00	−4.865138	0.4959786
10320.00	−4.970545	0.4955420
10325.00	−5.088117	0.4951059
10330.00	−5.220948	0.4946705
10335.00	−5.373483	0.4942356
10340.00	−5.552439	0.4938013
10345.00	−5.768679	0.4933676
10350.00	−6.041520	0.4929345
10355.00	−6.410619	0.4925020
10360.00	−6.981718	0.4920700
10365.00	−8.292125	0.4916386
10370.00	−7.948841	3.892291
10375.00	−6.856984	3.888264
10380.00	−6.320314	3.884248
10385.00	−5.960458	3.880240
10390.00	−5.688938	3.876241

10395.00	−5.470593	3.872252
10400.00	−5.287859	3.868273
10405.00	−5.130586	3.864302
10410.00	−4.992494	3.860340
10415.00	−4.869360	3.856387
10420.00	−4.758223	3.852444
10425.00	−4.656924	3.848509
10430.00	−4.563839	3.844584
10435.00	−4.477720	3.840667
10440.00	−4.397598	3.836760
10445.00	−4.322653	3.832861
10450.00	−4.252260	3.828971
10455.00	−4.185891	3.825090
10460.00	−4.123104	3.821218
10465.00	−4.063528	3.817355
10500.00	−3.714567	3.790558
10600.00	−3.067343	3.716298
10700.00	−2.652269	3.645302
10800.00	−2.347398	3.577394
10900.00	−2.107723	3.512410
11000.00	−1.911404	3.450194
11100.00	−1.746119	3.390604
11200.00	−1.604182	3.333506
11300.00	−1.480459	3.278773
11400.00	−1.371341	3.226288
11500.00	−1.274183	3.175941
11600.00	−1.186988	3.127628
11700.00	−1.108208	3.081252
11800.00	−1.036615	3.036722
11900.00	−0.9712204	2.993952
12000.00	−0.9112132	2.952861
12100.00	−0.8559216	2.913374
12200.00	−0.8047814	2.875419
12300.00	−0.7573131	2.838929
12400.00	−0.7131080	2.803839
12500.00	−0.6718121	2.770091
12600.00	−0.6331190	2.737627
12700.00	−0.5967606	2.706394
12800.00	−0.5624999	2.676341
12900.00	−0.5301288	2.647420
13000.00	−0.4994608	2.619587
13100.00	−0.4703301	2.592797
13200.00	−0.4425876	2.567012
13300.00	−0.4160981	2.542190
13400.00	−0.3907388	2.518298
13500.00	−0.2629591	2.493533
13600.00	−0.2365060	2.463472
13700.00	−0.2113342	2.433945
13800.00	−0.1873535	2.404938
13900.00	−0.1644931	2.376440
14000.00	−0.1426874	2.348438
14100.00	−0.1218766	2.320921
14200.00	−0.1020055	2.293878
14300.00	−8.3022378E−02	2.267297

14400.00	−6.4879976E−02	2.241168
14500.00	−4.7533680E−02	2.215482
14600.00	−3.0942462E−02	2.190227
14700.00	−1.5068039E−02	2.165395
14800.00	1.2577558E−04	2.140975
14900.00	1.4672253E−02	2.116958
15000.00	2.8603101E−02	2.093337
15100.00	4.1947644E−02	2.070101
15200.00	5.4733433E−02	2.047243
15300.00	6.6986710E−02	2.024754
15400.00	7.8731716E−02	2.002627
15500.00	8.9991711E−02	1.980853
15600.00	0.1007883	1.959426
15700.00	0.1111419	1.938337
15800.00	0.1210721	1.917580
15900.00	0.1305971	1.897147
16000.00	0.1397342	1.877033
16100.00	0.1484999	1.857229
16200.00	0.1569097	1.837731
16300.00	0.1649782	1.818532
16400.00	0.1727197	1.799624
16500.00	0.1801474	1.781004
16600.00	0.1872739	1.762664
16700.00	0.1941113	1.744599
16800.00	0.2006708	1.726804
16900.00	0.2069636	1.709274
17000.00	0.2130000	1.692002
17100.00	0.2187899	1.674985
17200.00	0.2243427	1.658216
17300.00	0.2296673	1.641692
17400.00	0.2347725	1.625407
17500.00	0.2396665	1.609357
17600.00	0.2443571	1.593537
17700.00	0.2488518	1.577943
17800.00	0.2531577	1.562572
17900.00	0.2572820	1.547417
18000.00	0.2612309	1.532475
18100.00	0.2650110	1.517744
18200.00	0.2686282	1.503217
18300.00	0.2720882	1.488893
18400.00	0.2753968	1.474766
18500.00	0.2785591	1.460833
18600.00	0.2815804	1.447092
18700.00	0.2844656	1.433537
18800.00	0.2872191	1.420167
18900.00	0.2898459	1.406977
19000.00	0.2923500	1.393965
19100.00	0.2947358	1.381127
19200.00	0.2970072	1.368460
19300.00	0.2991680	1.355961
19400.00	0.3012221	1.343627
19500.00	0.3031730	1.331455
19600.00	0.3050241	1.319443
19700.00	0.3067788	1.307588

19800.00	0.3084402	1.295886
19900.00	0.3100115	1.284336
20000.00	0.3114955	1.272934
20100.00	0.3128952	1.261679
20200.00	0.3142134	1.250567
20300.00	0.3154525	1.239597
20400.00	0.3166154	1.228765
20500.00	0.3177043	1.218071
20600.00	0.3187217	1.207510
20700.00	0.3196698	1.197081
20800.00	0.3165946	1.186852
20900.00	0.3173937	1.176786
21000.00	0.3181323	1.166845
21100.00	0.3188125	1.157028
21200.00	0.3194361	1.147333
21300.00	0.3200049	1.137757
21400.00	0.3205208	1.128299
21500.00	0.3209854	1.118956
21600.00	0.3214004	1.109727
21700.00	0.3217674	1.100609
21800.00	0.3220879	1.091602
21900.00	0.3223633	1.082703
22000.00	0.3225952	1.073911
22100.00	0.3227850	1.065223
22200.00	0.3229339	1.056639
22300.00	0.3230432	1.048156
22400.00	0.3231143	1.039773
22500.00	0.3231483	1.031489
22600.00	0.3231463	1.023301
22700.00	0.3231097	1.015209
22800.00	0.3230393	1.007210
22900.00	0.3229364	0.9993043
23000.00	0.3228019	0.9914892
23100.00	0.3226368	0.9837637
23200.00	0.3224420	0.9761264
23300.00	0.3222186	0.9685761
23400.00	0.3219673	0.9611112
23500.00	0.3216892	0.9537306
23600.00	0.3213849	0.9464331
23700.00	0.3210554	0.9392173
23800.00	0.3203978	0.9320825
23900.00	0.3200224	0.9250281
24000.00	0.3196232	0.9180520
24100.00	0.3192016	0.9111528
24200.00	0.3187584	0.9043294
24300.00	0.3182942	0.8975810
24400.00	0.3175611	0.8909068
24500.00	0.3170580	0.8843057
24600.00	0.3165355	0.8777761
24700.00	0.3159943	0.8713171
24800.00	0.3154348	0.8649277
24900.00	0.3148576	0.8586066

C.3.4 Arsenide

```
% Energy (eV)   f'              f''
  1000.000      -9.429335       3.484835
  1100.000      -10.50740       3.068583
  1200.000      -12.45976       2.726221
  1226.000      -13.32295       2.647042
  1231.000      -13.52381       2.632231
  1236.000      -13.73969       2.617549
  1241.000      -13.97290       2.602995
  1246.000      -14.22623       2.588568
  1251.000      -14.50320       2.574266
  1256.000      -14.80822       2.560088
  1261.000      -15.14697       2.546031
  1266.000      -15.52682       2.532096
  1271.000      -15.95758       2.518280
  1276.000      -16.45258       2.504581
  1281.000      -17.03035       2.490999
  1286.000      -17.71758       2.477531
  1291.000      -18.55410       2.464178
  1296.000      -19.60247       2.450936
  1300.000      -20.66173       2.440423
  1301.000      -20.96742       2.437805
  1306.000      -22.84129       2.424784
  1311.000      -25.63062       2.411871
  1316.000      -30.43916       2.399066
  1321.000      -42.96489       2.386366
  1326.000      -36.88134       37.12148
  1331.000      -23.81698       32.86283
  1336.000      -18.21088       29.21878
  1341.000      -15.38761       26.09086
  1346.000      -14.29931       23.39770
  1351.000      -14.89571       21.07187
  1356.000      -19.10551       19.05730
  1361.000      -17.71439       34.55799
  1366.000      -9.902804       30.98588
  1371.000      -6.451541       27.89469
  1376.000      -4.473392       25.21188
  1381.000      -3.272238       22.87692
  1386.000      -2.547956       20.83909
  1391.000      -2.139610       19.05578
  1396.000      -1.947594       17.49110
  1400.000      -1.906566       16.37623
  1401.000      -1.908722       16.11472
  1406.000      -1.979324       14.90097
  1411.000      -2.128795       13.82806
  1416.000      -2.335210       12.87744
  1421.000      -2.582657       12.03327
  1429.000      -3.035664       10.87096
  1431.000      -3.156718       10.61208
  1434.000      -3.342456       10.24493
```

1436.000	−3.468604	10.01348
1439.000	−3.660655	9.684943
1441.000	−3.790241	9.477643
1444.000	−3.986477	9.183137
1446.000	−4.118299	8.997155
1449.000	−4.317206	8.732725
1451.000	−4.450428	8.565610
1454.000	−4.650976	8.327834
1456.000	−4.785047	8.177460
1459.000	−4.986594	7.963365
1464.000	−5.323416	7.634889
1469.000	−5.661268	7.338550
1474.000	−6.000402	7.070988
1479.000	−6.341493	6.829267
1484.000	−6.685682	6.610822
1489.000	−7.034696	6.413407
1494.000	−7.391076	6.235057
1499.000	−7.758647	6.074046
1500.000	−7.833984	6.043787
1504.000	−8.143474	5.928864
1509.000	−8.556079	5.798186
1514.000	−9.017524	5.680850
1519.000	−9.581702	5.575845
1524.000	−10.49753	5.482283
1529.000	−10.74992	7.293207
1534.000	−10.33972	7.215660
1539.000	−10.28549	7.147589
1544.000	−10.33768	7.088501
1549.000	−10.44271	7.037976
1554.000	−10.58016	6.995667
1559.000	−10.74015	6.961286
1564.000	−10.91732	6.934611
1569.000	−11.10853	6.915473
1574.000	−11.31185	6.903756
1579.000	−11.52614	6.899396
1584.000	−11.75070	6.902381
1589.000	−11.98520	6.912745
1594.000	−12.22952	6.930571
1599.000	−12.48373	6.955991
1600.000	−12.53578	6.962002
1604.000	−12.74801	6.989188
1609.000	−13.02272	7.030393
1614.000	−13.30825	7.079892
1619.000	−13.60511	7.138022
1624.000	−13.91390	7.205182
1700.000	−20.74950	9.869416
1800.000	−3.552651	11.95705
1900.000	−2.690663	11.04163
2000.000	−2.021769	10.23876
2100.000	−1.535833	9.514412
2200.000	−1.162870	8.867381
2300.000	−0.8732193	8.286686
2400.000	−0.6465170	7.763263
2500.000	−0.4682811	7.289583

```
2600.000     -0.3279317       6.859340
2700.000     -0.2076773       6.464999
2800.000     -0.1174221       6.100526
2900.000     -5.1044028E-02   5.765710
3000.000     -3.8216980E-03   5.457530
3100.000      3.1523775E-02   5.175311
3200.000      5.6195986E-02   4.914834
3300.000      7.2109155E-02   4.673888
3400.000      8.0811761E-02   4.450536
3500.000      8.3562613E-02   4.243082
3600.000      8.1391051E-02   4.050028
3700.000      7.5142905E-02   3.870053
3800.000      6.5516859E-02   3.701986
3900.000      5.2611321E-02   3.544797
4000.000      3.7832122E-02   3.397550
4100.000      2.1137524E-02   3.259409
4200.000      2.8622695E-03   3.129628
4300.000     -1.6713578E-02   3.007537
4400.000     -3.7355002E-02   2.892534
4500.000     -5.8865067E-02   2.784072
4600.000     -8.1078410E-02   2.681660
4700.000     -0.1038563       2.584851
4800.000     -0.1270824       2.493236
4900.000     -0.1506592       2.406449
5000.000     -0.1745056       2.324152
5100.000     -0.1985538       2.246036
5200.000     -0.2227479       2.171820
5300.000     -0.2470421       2.101246
5400.000     -0.2713985       2.034077
5500.000     -0.2957873       1.970095
5600.000     -0.3201844       1.909100
5700.000     -0.3445683       1.850907
5800.000     -0.3722760       1.795460
5900.000     -0.3987048       1.742554
6000.000     -0.4229532       1.692062
6100.000     -0.4471485       1.643750
6200.000     -0.4712933       1.597494
6300.000     -0.4953918       1.553177
6400.000     -0.5194498       1.510691
6500.000     -0.5434756       1.469935
6600.000     -0.5674836       1.430815
6700.000     -0.5951601       1.393386
6800.000     -0.6191666       1.357447
6900.000     -0.6431822       1.322897
7000.000     -0.6672234       1.289664
7100.000     -0.6913077       1.257681
7200.000     -0.7154541       1.226885
7300.000     -0.7396829       1.197217
7400.000     -0.7640153       1.168624
7500.000     -0.7884746       1.141051
7600.000     -0.8130853       1.114452
7700.000     -0.8378736       1.088781
7800.000     -0.8628673       1.063993
7900.000     -0.8880959       1.040049
```

8000.000	−0.9135913	1.016910
8100.000	−0.9393874	0.9945406
8200.000	−0.9655202	0.9729064
8300.000	−0.9920292	0.9519748
8400.000	−1.018956	0.9317159
8500.000	−1.046346	0.9121004
8600.000	−1.074249	0.8931014
8700.000	−1.102717	0.8746931
8800.000	−1.131810	0.8568507
8900.000	−1.161590	0.8395514
9000.000	−1.192185	0.8228930
9100.000	−1.223608	0.8067341
9200.000	−1.255944	0.7910547
9300.000	−1.289289	0.7758356
9400.000	−1.323748	0.7610589
9500.000	−1.359442	0.7467071
9600.000	−1.396506	0.7327641
9700.000	−1.435091	0.7192142
9800.000	−1.475373	0.7060425
9900.000	−1.517552	0.6932349
10000.00	−1.561863	0.6807779
10100.00	−1.608575	0.6686586
10200.00	−1.658008	0.6568649
10300.00	−1.710545	0.6453850
10400.00	−1.766640	0.6342077
10500.00	−1.826852	0.6233222
10600.00	−1.891866	0.6127184
10700.00	−1.962539	0.6023866
10800.00	−2.039969	0.5923173
10900.00	−2.125583	0.5825018
11000.00	−2.221288	0.5729312
11100.00	−2.329711	0.5635975
11200.00	−2.454608	0.5544930
11300.00	−2.601625	0.5456098
11400.00	−2.779780	0.5369410
11500.00	−3.004832	0.5284795
11600.00	−3.308127	0.5202186
11700.00	−3.767294	0.5121522
11769.00	−4.303414	0.5066964
11774.00	−4.356803	0.5063044
11779.00	−4.413270	0.5059130
11784.00	−4.473176	0.5055220
11789.00	−4.536944	0.5051315
11794.00	−4.605115	0.5047414
11799.00	−4.678308	0.5043518
11800.00	−4.693621	0.5042739
11804.00	−4.757299	0.5039626
11809.00	−4.843057	0.5035739
11814.00	−4.936817	0.5031856
11819.00	−5.040181	0.5027978
11824.00	−5.155290	0.5024104
11829.00	−5.285084	0.5020235
11834.00	−5.433736	0.5016371
11839.00	−5.607609	0.5012511

11844.00	−5.816780	0.5008656
11849.00	−6.078978	0.5004805
11854.00	−6.429896	0.5000958
11859.00	−6.960586	0.4997116
11864.00	−8.076112	0.4993278
11869.00	−8.254848	3.865319
11874.00	−7.011160	3.861774
11879.00	−6.446832	3.858236
11884.00	−6.076585	3.854706
11889.00	−5.800160	3.851182
11894.00	−5.579269	3.847666
11899.00	−5.395152	3.844157
11900.00	−5.361740	3.843457
11904.00	−5.237200	3.840655
11909.00	−5.098830	3.837161
11914.00	−4.975692	3.833674
11919.00	−4.864691	3.830194
11924.00	−4.763636	3.826720
11929.00	−4.670869	3.823254
11934.00	−4.585117	3.819795
11939.00	−4.505380	3.816343
11944.00	−4.430857	3.812897
11949.00	−4.360900	3.809459
11954.00	−4.294974	3.806028
11959.00	−4.232644	3.802605
11964.00	−4.173512	3.799188
12000.00	−3.819016	3.774788
12100.00	−3.181885	3.708845
12200.00	−2.772388	3.645494
12300.00	−2.470868	3.584609
12400.00	−2.233180	3.526073
12500.00	−2.037926	3.469776
12600.00	−1.873044	3.415612
12700.00	−1.731026	3.363485
12800.00	−1.606859	3.313302
12900.00	−1.497025	3.264975
13000.00	−1.398948	3.218422
13100.00	−1.310685	3.173567
13200.00	−1.230730	3.130335
13300.00	−1.157891	3.088657
13400.00	−1.091206	3.048468
13500.00	−1.029888	3.009706
13600.00	−0.9732839	2.972312
13700.00	−0.9208464	2.936231
13800.00	−0.8721094	2.901409
13900.00	−0.8266758	2.867798
14000.00	−0.7842017	2.835349
14100.00	−0.7443893	2.804018
14200.00	−0.7069778	2.773762
14300.00	−0.6717373	2.744539
14400.00	−0.6384651	2.716313
14500.00	−0.6069801	2.689046
14600.00	−0.5771215	2.662703
14700.00	−0.5487446	2.637251

14800.00	−0.5217186	2.612658
14900.00	−0.4959261	2.588894
15000.00	−0.4712596	2.565931
15100.00	−0.4476219	2.543740
15200.00	−0.4249241	2.522297
15300.00	−0.4030842	2.501575
15400.00	−0.3820317	2.481552
15500.00	−0.2537031	2.457054
15600.00	−0.2314214	2.431130
15700.00	−0.2100757	2.405610
15800.00	−0.1896170	2.380485
15900.00	−0.1699997	2.355747
16000.00	−0.1511804	2.331387
16100.00	−0.1331194	2.307398
16200.00	−0.1157795	2.283772
16300.00	−9.9125974E−02	2.260503
16400.00	−8.3125629E−02	2.237581
16500.00	−6.7748182E−02	2.215002
16600.00	−5.2964929E−02	2.192758
16700.00	−3.8748894E−02	2.170842
16800.00	−2.5074953E−02	2.149248
16900.00	−1.1918684E−02	2.127970
17000.00	7.4218388E−04	2.107000
17100.00	1.2928919E−02	2.086334
17200.00	2.4661615E−02	2.065966
17300.00	3.5959065E−02	2.045889
17400.00	4.6839688E−02	2.026098
17500.00	5.7320297E−02	2.006588
17600.00	6.7417055E−02	1.987354
17700.00	7.7145278E−02	1.968389
17800.00	8.6519368E−02	1.949690
17900.00	9.5553502E−02	1.931251
18000.00	0.1042607	1.913067
18100.00	0.1126534	1.895134
18200.00	0.1207435	1.877446
18300.00	0.1285424	1.860001
18400.00	0.1360610	1.842792
18500.00	0.1433097	1.825816
18600.00	0.1502983	1.809069
18700.00	0.1570361	1.792546
18800.00	0.1635175	1.776244
18900.00	0.1697807	1.760158
19000.00	0.1758191	1.744285
19100.00	0.1816405	1.728621
19200.00	0.1872524	1.713162
19300.00	0.1926621	1.697905
19400.00	0.1978766	1.682846
19500.00	0.2029025	1.667982
19600.00	0.2077461	1.653309
19700.00	0.2124137	1.638824
19800.00	0.2169109	1.624525
19900.00	0.2212437	1.610407
20000.00	0.2254172	1.596468
20100.00	0.2294368	1.582704

20200.00	0.2333074	1.569113
20300.00	0.2370338	1.555692
20400.00	0.2406207	1.542439
20500.00	0.2440726	1.529349
20600.00	0.2473937	1.516421
20700.00	0.2505882	1.503651
20800.00	0.2536599	1.491039
20900.00	0.2566130	1.478580
21000.00	0.2594509	1.466272
21100.00	0.2621772	1.454113
21200.00	0.2647954	1.442100
21300.00	0.2673087	1.430232
21400.00	0.2697205	1.418505
21500.00	0.2720338	1.406918
21600.00	0.2742515	1.395469
21700.00	0.2763766	1.384154
21800.00	0.2784117	1.372973
21900.00	0.2803596	1.361922
22000.00	0.2822230	1.351001
22100.00	0.2840042	1.340206
22200.00	0.2857057	1.329536
22300.00	0.2873298	1.318990
22400.00	0.2888789	1.308565
22500.00	0.2903550	1.298259
22600.00	0.2917604	1.288070
22700.00	0.2930970	1.277997
22800.00	0.2943668	1.268039
22900.00	0.2955718	1.258192
23000.00	0.2967138	1.248456
23100.00	0.2977946	1.238830
23200.00	0.2988158	1.229310
23300.00	0.2997794	1.219897
23400.00	0.3006867	1.210587
23500.00	0.3015394	1.201380
23600.00	0.3023391	1.192275
23700.00	0.3030872	1.183269
23800.00	0.3003767	1.174414
23900.00	0.3010126	1.165682
24000.00	0.3016027	1.157046
24100.00	0.3021481	1.148504
24200.00	0.3026502	1.140054
24300.00	0.3031102	1.131696
24400.00	0.3035291	1.123428
24500.00	0.3039081	1.115249
24600.00	0.3042483	1.107157
24700.00	0.3045507	1.099151
24800.00	0.3048164	1.091230
24900.00	0.3050463	1.083393

BIBLIOGRAPHY

BIBLIOGRAPHY

1. AM Lindenberg, I. Kang, SL Johnson, T. Missalla, PA Heimann, Z. Chang, J. Larsson, PH Bucksbaum, HC Kapteyn, HA Padmore, et al. Time-resolved x-ray diffraction from coherent phonons during a laser-induced phase transition. *Physical Review Letters*, 84(1):111–114, 2000.

2. A. Cavalleri, CW Siders, FLH Brown, DM Leitner, C. Toth, JA Squier, CPJ Barty, KR Wilson, K. Sokolowski-Tinten, M. Horn von Hoegen, et al. Anharmonic lattice dynamics in germanium measured with ultrafast X-ray diffraction. *Physical review letters*, 85(3):586–589, 2000.

3. A. Cavalleri, CW Siders, C. Rose-Petruck, R. Jimenez, C. Toth, JA Squier, CPJ Barty, KR Wilson, K. Sokolowski-Tinten, M. Horn von Hoegen, et al. Ultrafast x-ray measurement of laser heating in semiconductors: Parameters determining the melting threshold. *Physical Review B*, 63(19):193306, 2001.

4. DA Reis, MF DeCamp, PH Bucksbaum, R. Clarke, E. Dufresne, M. Hertlein, R. Merlin, R. Falcone, H. Kapteyn, MM Murnane, et al. Probing impulsive strain propagation with X-ray pulses. *Physical Review Letters*, 86(14):3072–3075, 2001.

5. MF DeCamp, DA Reis, PH Bucksbaum, B. Adams, JM Caraher, R. Clarke, CWS Conover, EM Dufresne, R. Merlin, V. Stoica, et al. Coherent control of pulsed X-ray beams. *Nature*, 413(6858):825–828, 2001.

6. MF DeCamp, DA Reis, A. Cavalieri, PH Bucksbaum, R. Clarke, R. Merlin, EM Dufresne, DA Arms, AM Lindenberg, AG MacPhee, et al. Transient strain driven by a dense electron-hole plasma. *Physical review letters*, 91(16):165502, 2003.

7. S.H. Lee. *Time-Resolved X-ray Measurements of Energy Relaxation in Ultrafast Laser Excited Semiconductors*. PhD thesis, The University of Michigan, 2006.

8. M.F. DeCamp. *Seeing sound: Dynamical effects in ultrafast x-ray diffraction*. PhD thesis, The Univesity of Michigan, 2002.

9. DM Fritz, DA Reis, B. Adams, RA Akre, J. Arthur, C. Blome, PH Bucksbaum, AL Cavalieri, S. Engemann, S. Fahy, et al. Ultrafast bond softening in bismuth: Mapping a solid's interatomic potential with X-rays. *Science*, 315(5812):633, 2007.

10. SK Sundaram and E. Mazur. Inducing and probing non-thermal transitions in semiconductors using femtosecond laser pulses. *Nature materials*, 1(4):217–224, 2002.

11. C. Thomsen, HT Grahn, HJ Maris, and J. Tauc. Surface generation and detection of phonons by picosecond light pulses. *Physical Review B*, 34(6):4129–4138, 1986.

12. C. Rose-Petruck, R. Jimenez, T. Guo, A. Cavalleri, C.W. Siders, F. Raksi, J.A. Squier, B.C. Walker, K.R. Wilson, and C.P. Barty. Picosecond-milliangstrom lattice dynamics measured by ultrafast X-ray diffraction. *Nature*, 398(6725):310–312, 1999.

13. AH Chin, RW Schoenlein, TE Glover, P. Balling, WP Leemans, and CV Shank. Ultrafast structural dynamics in InSb probed by time-resolved x-ray diffraction. *Physical review letters*, 83(2):336–339, 1999.

14. MF DeCamp, DA Reis, DM Fritz, PH Bucksbaum, EM Dufresne, and R. Clarke. X-ray synchrotron studies of ultrafast crystalline dynamics. *Journal of synchrotron radiation*, 12(2):177–192, 2005.

15. B.E. Warren. *X-ray Diffraction*. Dover, 1990.

16. W. H Zachariasen. *Theory of X-ray Diffraction in Crystals*. Dover, 1967.

17. DT Cromer and JB Mann. X-ray scattering factors computed from numerical Hartree-Fock wave functions. *Acta Crystallographica Section A: Crystal Physics, Diffraction, Theoretical and General Crystallography*, 24(2):321–324, 1968.

18. CT Chantler, K. Olsen, RA Dragoset, AR Kishore, SA Kotochigova, and DS Zucker. X-ray form factor, attenuation and scattering tables (version 2.0). *National Institute of Standards and Technology, Gaithersburg, MD. Available online: http://physics. nist. gov/ffast*, 2003.

19. BL Henke, EM Gullikson, and JC Davis. X-ray interactions: photoabsorption, scattering, transmission, and reflection at E= 50-30,000 eV, Z= 1-92. *Atomic data and nuclear data tables*, 54(2):181–342, 1993.

20. Krystyn van Vliet. 3.22 mechanical behavior of materials, spring 2008. (massachusetts institute of technology: Mit opencourseware), http://ocw.mit.edu. (Accessed 21 May, 2010). License: Creative Commons BY-NC-SA.

21. M. Schowalter, A. Rosenauer, JT Titantah, and D. Lamoen. Computation and parametrization of the temperature dependence of Debye-Waller factors for group IV, III-V and II-VI semiconductors. *Acta Crystallographica Section A: Foundations of Crystallography*, 65(1):5–17, 2008.

22. B.W. Batterman and H. Cole. Dynamical diffraction of X rays by perfect crystals. *Reviews of modern physics*, 36(3):681–717, 1964.

23. J. Als-Nielsen and Des McMorrow. *Elements of modern X-ray physics*. Wiley Chichester, 2001.

24. S. Takagi. Dynamical theory of diffraction applicable to crystals with any kind of small distortion. *Acta Crystallographica*, 15(12):1311–1312, 1962.

25. D. Taupin. Dynamic theory of x-ray diffraction in crystals. *Bull. Soc. Franc. Miner. Crystallogr*, 87:469, 1964.

26. CR Wie, TA Tombrello, and T. Vreeland Jr. Dynamical x-ray diffraction from nonuniform crystalline films: Application to x-ray rocking curve analysis. *Journal of Applied Physics*, 59:3743, 1986.

27. AM Lindenberg, I. Kang, SL Johnson, RW Falcone, PA Heimann, Z. Chang, RW Lee, and JS Wark. Coherent control of phonons probed by time-resolved x-ray diffraction. *Optics letters*, 27(10):869–871, 2002.

28. CR Wie, TA Tombrello, and T. Vreeland Jr. Erratum: Dynamical x-ray diffraction from nonuniform crystalline films: Application to x-ray rocking curve analysis [J. Appl. Phys. 59, 3743 (1986)]. *Journal of Applied Physics*, 70:2481, 1991.

29. S. A. Stepanov. X0h on the web. http://sergey.gmca.aps.anl.gov/x0h.html.

30. EM. Dufresne, B. Adams, DA. Arms, M. Chollet, EC Landahl, Y. Li, DA Walko, and J. Wang. Time-resolved research at the advanced photon source beamline 7-id. *SRI 2009, 10th International Conference on Radiation Instrumentation*, pages 177–181, 2009.

31. DA Walko, DA Arms, and EC Landahl. Empirical dead-time corrections for synchrotron sources. *Journal of synchrotron radiation*, 15(6):612–617, 2008.

32. A. Rousse, C. Rischel, and J.C. Gauthier. Femtosecond x-ray crystallography. *Reviews of Modern Physics*, 73(1):17–31, 2001.